The *ROSAT* Brightest Cluster Sample – I. The compilation of the sample and the cluster log *N*–log *S* distribution

H. Ebeling,[1,2,3]⋆ A. C. Edge,[2] H. Böhringer,[1] S. W. Allen,[2] C. S. Crawford,[2] A. C. Fabian,[2] W. Voges[1] and J. P. Huchra[4]

[1]*Max-Planck-Institut für extraterrestrische Physik, Giessenbachstrasse, D-85740 Garching, Germany*
[2]*Institute of Astronomy, Madingley Road, Cambridge CB3 0HA*
[3]*Institute for Astronomy, 2680 Woodlawn Drive, Honolulu, HI 96822, USA*
[4]*Harvard-Smithsonian Center for Astrophysics, 60 Garden Street, Cambridge, MA 02138, USA*

ABSTRACT

We present a 90 per cent flux-complete sample of the 201 X-ray-brightest clusters of galaxies in the northern hemisphere ($\delta \geq 0°$), at high Galactic latitudes ($|b| \geq 20°$), with measured redshifts $z \leq 0.3$ and fluxes higher than 4.4×10^{-12} erg cm^{-2} s^{-1} in the 0.1–2.4 keV band. The sample, called the *ROSAT* Brightest Cluster Sample (BCS), is selected from *ROSAT* All-Sky Survey data and is the largest X-ray-selected cluster sample compiled to date. In addition to Abell clusters, which form the bulk of the sample, the BCS also contains the X-ray-brightest Zwicky clusters and other clusters selected from their X-ray properties alone. Effort has been made to ensure the highest possible completeness of the sample and the smallest possible contamination by non-cluster X-ray sources. X-ray fluxes are computed using an algorithm tailored for the detection and characterization of X-ray emission from galaxy clusters. These fluxes are accurate to better than 15 per cent (mean 1σ error).

We find the cumulative log *N*–log *S* distribution of clusters to follow a power law $\kappa \, S^{-\alpha}$ with $\alpha = 1.31^{+0.06}_{-0.03}$ (errors are the 10th and 90th percentiles) down to fluxes of 2×10^{-12} erg cm^{-2} s^{-1}, i.e. considerably below the BCS flux limit. Although our best-fitting slope disagrees formally with the canonical value of -1.5 for a Euclidean distribution, the BCS log *N*–log *S* distribution is consistent with a non-evolving cluster population if cosmological effects are taken into account.

Our sample will allow us to examine large-scale structure in the northern hemisphere, determine the spatial cluster–cluster correlation function, investigate correlations between the X-ray and optical properties of the clusters, establish the X-ray luminosity function for galaxy clusters, and discuss the implications of the results for cluster evolution.

Key words: catalogues – surveys – galaxies: clusters: general – cosmology: observations – large-scale structure of Universe – X-rays: galaxies.

1 INTRODUCTION

Clusters of galaxies are the most massive entities to have collapsed after decoupling from the Hubble expansion of the Universe. As a consequence, they represent excellent tracers of the formation and evolution of structure on the scale of a few to tens of megaparsecs.

As far as the compilation of statistical samples of galaxy clusters is concerned, the emphasis has, historically, been on optical cluster properties such as the projected galaxy surface density in the cluster core or the total number of galaxies in a pre-defined magnitude range and within a fixed radius from the nominal cluster centre. The

largest compilations of this kind are the catalogues of Abell (1958), Abell, Corwin & Olowin (1989, hereafter ACO), and Zwicky and co-workers (1961–68), each containing thousands of entries.

The statistical quality of optically selected cluster samples from these early years is, however, seriously impaired not only by projection effects but also by the subjectivity of an 'eyeball' selection process (Lucey 1983; Sutherland 1988; Struble & Rood 1991). Whereas this 'human factor' has recently been eliminated almost entirely by entrusting the detection and classification of clusters to computer algorithms (e.g. Dalton et al. 1992; Lumsden et al. 1992; Irwin, Maddox & McMahon 1994; Wallin et al. 1994; Postman et al. 1996), the fundamental problem remains that optical images probe the distribution of galaxies only in two dimensions.

⋆E-mail: ebeling@ifa.hawaii.edu

Therefore fluctuations in the surface density of field galaxies as well as superpositions of poor clusters along the line of sight can lead to an overestimation of a system's richness. On the other hand, poor clusters can be missed completely as they often do not contrast strongly with the background field (Frenk et al. 1990; van Haarlem, Frenk & White 1997). Extensive spectroscopic follow-up is required to allow these effects to be quantified (e.g. Collins et al. 1995). Future optical cluster surveys may be able to reduce the impact of projection effects by using multi-colour photometry to improve the contrast of the cluster galaxies over the foreground and background galaxy population – at present such techniques are still under development.

The problem of projection effects can, however, be overcome almost completely by selecting clusters in the X-ray rather than in the optical band. X-ray emission from a diffuse, gaseous intra-cluster medium (ICM) gravitationally confined at temperatures of typically a few $\times 10^7$ K is a sure indication that the system is indeed three-dimensionally bound. Being due to ion–electron interactions and thus proportional to the square of the density in the ICM, the X-ray flux is also much more peaked at the gravitational centre of the cluster than the projected galaxy distribution. This property requires clusters to be almost perfectly aligned along the line of sight in order to be mistaken for a single, more luminous entity, so that projection effects caused by such superpositions can be effectively neglected in the X-ray band.

X-rays thus provide a very efficient and less biased way of compiling cluster samples. Early statistical cluster samples have been compiled from the X-ray data taken by the *Uhuru* (Schwartz 1978), *Ariel V* (McHardy 1978) and *HEAO-1 A-2* satellites (Piccinotti et al. 1982), all of which comprised about 30 clusters. Including clusters detected during the *EXOSAT* mission, Edge et al. (1990) presented an X-ray flux-limited sample of 55 clusters, very similar in size to the statistically complete $z \geq 0.14$ subset of the sample compiled by Gioia et al. (1990) from X-ray sources detected in the *Einstein* Medium Sensitivity Survey (EMSS). The sample of Edge et al. covers the whole extragalactic sky; its depth, however, is limited to redshifts $z < 0.2$ owing to the rather high flux limit at 1.7×10^{-11} erg cm^{-2} s^{-1} in the 2–10 keV band. Hence only the more X-ray-luminous systems are included. The EMSS sample, on the other hand, extends to fluxes of 2×10^{-13} erg cm^{-2} s^{-1} in the 0.3–3.5 keV band and out to redshifts of $z \sim 0.8$ but, even at the brightest fluxes, covers no more than 740 square degrees, i.e. less than 2 per cent of the sky. As a consequence, it samples preferentially an intermediate luminosity range.

In 1991, the completion of the *ROSAT* All-Sky Survey (RASS: Voges 1992) provided a data base of unprecedented quality for the compilation of X-ray-selected cluster samples. Statistical cluster samples compiled from RASS data over sky areas of the order of 1000 square degrees were used by Nichol, Briel & Henry (1994) and Romer et al. (1994) to compute the cluster two-point correlation function. On a larger scale, the first RASS X-ray flux-limited cluster sample with broad sky coverage has recently been presented by Ebeling et al. (1996, hereafter EVB). However, their all-sky sample (named XBACs) comprises only ACO clusters and, albeit X-ray *flux-limited*, it is thus not strictly X-ray-*selected*; this applies also to the much smaller sample of Nichol et al. (1994).

The *ROSAT* Brightest Cluster Sample (BCS) presented in this paper is designed to overcome these limitations. The BCS is an X-ray flux-limited cluster sample covering the whole extragalactic sky ($|b| \geq 20°$) in the northern hemisphere (where the median exposure time in the RASS is 30 per cent longer than in the south). At the same time, the BCS goes beyond optically known clusters to include systems that were selected on the grounds of their X-ray properties alone. We search explicitly for X-ray emission around Abell and Zwicky clusters, but also examine all bright X-ray sources that were found to be significantly extended in the RASS. Optical follow-up observations were performed, first to confirm the cluster nature of the X-ray-selected systems, secondly to obtain redshifts for those BCS clusters for which reliable redshift measurements could not be found in the literature, and thirdly to investigate the spectral properties of the central cluster galaxies (Allen et al. 1992; Crawford et al. 1995, and in preparation).

As the procedure followed in the compilation of the BCS is in many respects very similar, if not identical, to the one employed during the compilation of the XBACs sample, we shall limit the description of certain steps to the minimum required to keep this paper self-contained and, whenever possible, refer to EVB for a more detailed account.

In this, logically if not chronologically, first article of a series we present the BCS and discuss its statistical properties; in other papers in this series we determine the X-ray cluster luminosity function for the BCS and discuss cluster evolution (Ebeling et al. 1997), constrain cosmological parameters using the BCS (Ebeling et al., in preparation), and establish the spatial cluster–cluster correlation function (Edge et al., in preparation).

Throughout this paper, we assume an Einstein–de Sitter universe with $q_0 = 0.5$ and $H_0 = 50$ km s^{-1} Mpc^{-1}.

2 THE X-RAY DATA BASE[1]

From 1990 August to 1991 February, the *ROSAT* X-ray satellite conducted an all-sky survey (RASS) in the soft X-ray energy band ranging from 0.11 to 2.4 keV. Overviews of the *ROSAT* mission in general and the RASS in particular can be found in the literature (Trümper 1990; Voges 1992). A first processing of the data taken by the Position Sensitive Proportional Counter (PSPC) during the RASS was performed as the survey proceeded using the Standard Analysis Software System (SASS, Voges et al. 1992) developed for this purpose at the Max-Planck-Institut für Extraterrestrische Physik (MPE). To this end, the incoming X-ray data were sorted into 2°-wide strips of constant ecliptic longitude following the satellite's scanning motion on the sky. Only three days' worth of data are collected in one strip, though, so that the exposure time in each strip is roughly constant at some 360 s, and the much longer exposure times accumulated around the ecliptic poles are not taken advantage of.

Running on the 90 strips representing the RASS in this framework, the SASS detected 49 441 X-ray sources [multiple detections removed, see Cruddace et al. (1991) for details of the source detection procedure] which constitute the X-ray sample upon which most of the statistical RASS studies performed to date are based. Note that although, in this first processing of the survey data, the SASS provided count rates in various energy bands, the actual source *detection* was performed exclusively in the PSPC broad band, i.e. in the energy range from 0.1 to 2.4 keV. The source count distribution for all SASS sources from this master source list[2] is depicted in Fig. 1 and shows that a minimum of some 10 to 15 photons is required for any source in order to be detected reliably in this first processing of the RASS data. In terms of count rates, this

---

[1] This short section is essentially the same as the identically named one in EVB; we feel that the gain in comprehensiveness of this paper justifies the repetition.

[2] This is exactly the same source list as the one used by EVB in the compilation of the XBACs sample; Fig. 1 is reproduced from their paper.
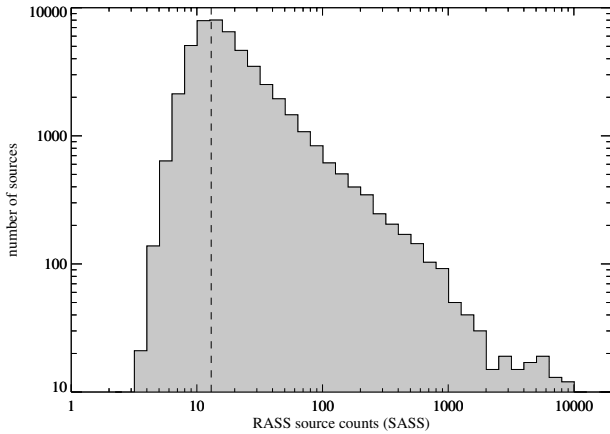
Figure 1. The differential frequency distribution of the X-ray photon counts in RASS sources as detected by the SASS. Accordingly, the SASS master source list starts to become incomplete at source strengths of less than about 15 photons. [Reproduced from EVB.]
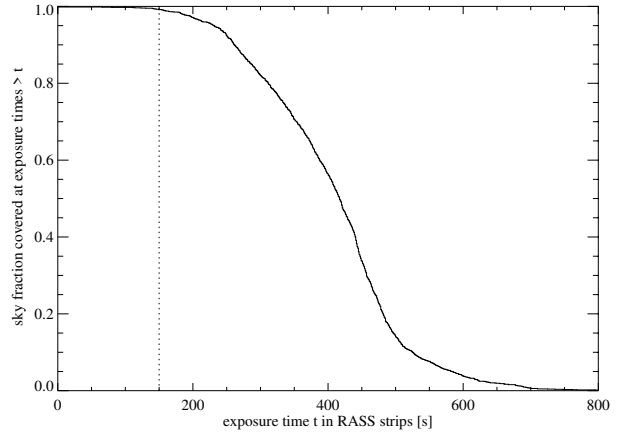

Figure 2. The cumulative frequency distribution of the RASS exposure times in the strips upon which the first SASS processing was performed. Exposure times are computed in squares of 23-arcmin^2 area around 5000 positions randomly distributed on the northern extragalactic sky.
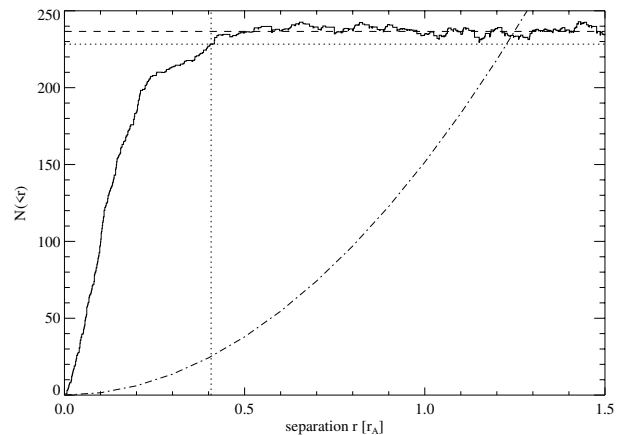

Figure 3. The cumulative number of coincidences in the cross-correlation between the Abell catalogue and the RASS X-ray source list provided by the SASS as a function of the X-ray to optical source separation. Only X-ray sources with SASS count rates higher than 0.1 count s^{-1}, $\delta \geq 0°$ and $|b| \geq 20°$ are considered. A parabolic background component (the dot–dashed line) has been subtracted. The dashed line marks the total number of true coincidences. The dotted lines, finally, mark the selected maximal separation and the corresponding number of true coincidences (see text for details).

translates into an approximate detection limit of 0.04 to 0.05 count s^{-1}; by comparison, the brightest RASS sources feature SASS count rates of the order of 10 count s^{-1} (Voges 1992).

Since 1992, so-called PET files (for 'photon event table') have been produced at MPE; they contain the full photon information in a field of specified size around any given position in the sky, thereby overcoming the limitations of the strip data used in the earlier processing.

Clearly, the optimal approach for the compilation of a highly complete cluster sample from RASS data would be to run an algorithm optimized for the detection of extended emission (e.g. VTP, see Section 3.2) on PET fields for the whole study area. However, running VTP on the whole northern extragalactic sky would have required a total of almost 4000 $2° \times 2°$ PET fields – the production of such a large number of merged photon sets was not feasible when this project was started. We therefore pursued the approach described in detail in the following sections.

3 A TENTATIVE SAMPLE

3.1 The SASS-based sample

Starting from the results of the first SASS processing mentioned above, we select a subset of 10 241 sources with SASS count rates[3] in excess of 0.1 count s^{-1}. This threshold is the result of a compromise between maximal sky coverage and maximal survey depth: for sources consisting of less than ~ 15 photons, the SASS source list starts to become incomplete (see Fig. 1), and at minimal exposure times higher than 150 s the sky coverage of the RASS in the northern hemisphere starts to fall below 99 per cent. The latter figure is derived from the distribution shown in Fig. 2. In the southern hemisphere the completeness with respect to sky coverage is less than 89 per cent at a limiting exposure time of 150 s (EVB) owing to the fact that, in order to avoid damage to the detector electronics, the PSPC was switched off automatically during the All-Sky Survey when passing through regions of enhanced particle background around the so-called South Atlantic Anomaly.

We cross-correlated the reduced SASS X-ray source list with the Abell cluster catalogue (limited to the northern extragalactic sky, i.e. $\delta \geq 0°$, $|b| \geq 20°$) using the redshifts of the clusters to scale angular to metric separations.[4] The latter are measured in units of Abell radii ($1 r_A = 1.5 h_{100}^{-1}$ Mpc). Estimated redshifts based on the magnitude of the tenth-ranked cluster galaxy, m_{10}, and taking into account the cluster richness, are used where measured redshifts are not available; details of the procedure employed to estimate ACO cluster redshifts can be found in EVB. Fig. 3 shows the resulting cumulative distribution of the separations between the SASS X-ray sources and the optical cluster positions. Without any corrections this distribution would be dominated by chance alignments, the number of which increases as the area inside a radius r and thus rises as the square of the separation between the cluster and the respective X-ray source. To counteract this effect, a parabolic

---

[3] For clusters of galaxies observed through a column density n_H of neutral hydrogen, a PSPC broad-band count rate of 0.1 count s^{-1} translates into an unabsorbed energy flux of 1.2×10^{-12} erg cm^{-2} s$^{-1} \times n_H^{0.27}$ in the same 0.1–2.4 keV band if n_H is given in units of 10^{20} cm^{-2}. This formula is accurate to better than 10(5) per cent for all gas temperatures in excess of 1.3(2.2) keV.

[4] Note that both the angular and the metric separations discussed in this section are necessarily measured *in projection* only.
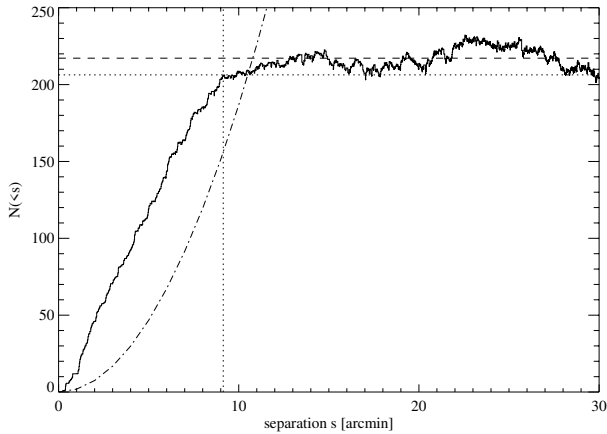
Figure 4. The cumulative number of coincidences in the cross-correlation between the Zwicky catalogue and the RASS X-ray source list provided by the SASS as a function of the X-ray to optical source separation. Only X-ray sources with SASS count rates higher than 0.1 count s^{-1}, $\delta \geq 0°$ and $|b| \geq 20°$ are considered. A parabolic background component (the dot–dashed line) has been subtracted. The dashed line marks the total number of true coincidences. The dotted lines, finally, mark the selected maximal separation and the corresponding number of true coincidences (see text for details).

contribution from random coincidences fitted to the data in the $0.75 \leq r/r_A \leq 1.5$ range has been subtracted (the dash–dotted curve in Fig. 3). The total number of true coincidences (as opposed to chance coincidences) of 236.6 is given by the number at which the cumulative distribution of Fig. 3 levels off, and is indicated by the dashed line in Fig. 3.

Using the same cut-off in the respective separations as Ebeling and co-workers for their XBACs sample ($r_{max} = 0.407\, r_A$, see the dotted lines in Fig. 3), we extract a 96.5 per cent complete sample consisting of 253 correlation pairs involving 252 unique SASS X-ray sources assigned to 235 different Abell clusters. Here, like in the following, the quoted completeness (96.5 per cent) refers to the fraction of the total number of true coincidences (marked by the dashed line in Fig. 3) found within the respective maximal radial separation. As, even at $z = 0.4$, the mentioned radial cut-off of $r_{max} = 0.407\, r_A$ still translates into an angular separation of more than 3 arcmin, it always covers the uncertainty in the optical cluster positions of typically 2 to 3 arcmin (ACO) which therefore do not need to be taken into account separately. Some 25 entries from this list, i.e. 10 per cent, can be expected to be coincidental.

Of the 49 catalogued Abell clusters in our study area with $z \leq 0.05$, only 30 are contained in this list. The lack of SASS detections in excess of 0.1 count s^{-1} for the remaining 19 nearby Abell clusters is, however, not necessarily indicative of their being intrinsically X-ray-faint. Rather, it is possible that the SASS detection algorithms have heavily underestimated the flux from such potentially highly extended sources, or may have missed the source altogether (EVB), as the SASS was designed solely for the detection of point sources. We therefore also include the remaining 19 Abell clusters with $z \leq 0.05$, which brings the total number of Abell clusters in our tentative sample to 254.

As was shown by EVB, problems with the SASS detection efficiency as far as cluster emission is concerned exist also for systems at redshifts greater than 0.05. However, the sheer number of Abell clusters at higher redshifts makes it unfeasible to include them all as potential detections at this point (see Section 3.2 for a description of the reprocessing of the RASS data performed at the positions of all tentative SASS cluster detections). The amount of
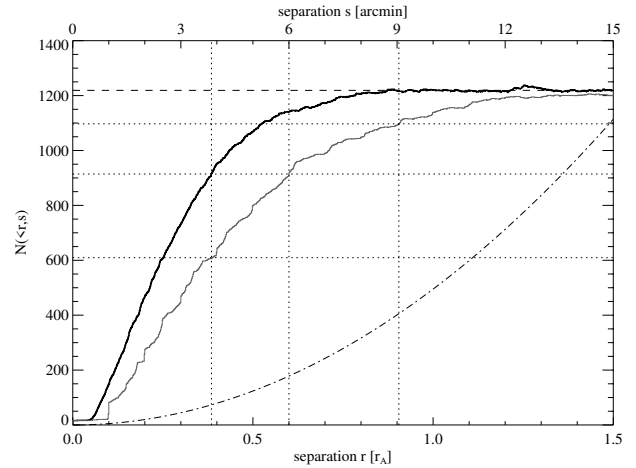

Figure 5. The cumulative number of coincidences in a cross-correlation between the Zwicky and the Abell clusters in our study area as a function of their separation. The bold solid curve represents the number of coincidences within a given metric separation; the fine line corresponds to angular separations as annotated on the upper *x*-axis. A parabolic background component (the dot–dashed line) has been subtracted. The dashed line marks the total number of true coincidences. The dotted lines, finally, mark the 50th, 75th and 90th completeness percentiles for the set of true coincidences found in the angular cross-correlation.

incompleteness of the BCS introduced by missing SASS detections of clusters at all redshifts is discussed in detail in Section 7.1.

For the 8528 Zwicky clusters with $\delta \geq 0°$ and $|b| \geq 20°$ the procedure is essentially the same. Note, however, that we now perform the cross-correlation with the SASS X-ray source list on an angular rather than a metric scale, as redshifts (measured or estimated) are not available for the whole of the Zwicky catalogue. Just as Fig. 3 does for Abell clusters, Fig. 4 summarizes the results of the cross-correlation between the 10 241 RASS X-ray sources with SASS count rates above 0.1 count s^{-1} and the Zwicky cluster list. The total number of true coincidences in this cross-correlation is 217.2; a 95 per cent complete sample extracted at separations of less than 9.1 arcmin consists of 362 coincidences (involving 355 unique SASS sources and 354 different Zwicky clusters), of which some 156 (43 per cent) are expected to be non-physical.

Because of the substantial overlap between the Abell and Zwicky cluster catalogues, many of the X-ray sources associated with Zwicky clusters in our cross-correlation are, at the same time, also contained in the subsample extracted from the cross-correlation with the Abell catalogue. Fig. 5 shows the cumulative number of coincidences in a positional cross-correlation between the Abell and Zwicky clusters in our study area as a function of both their metric (thick solid line) and angular separations (thin solid line).[5] According to Fig. 5, some 1200 clusters have been detected independently by Abell and Zwicky and co-workers. Although, for half of them, the optical cluster centroids determined by Abell and Zwicky agree to within about 4 arcmin, one-quarter of the common clusters are separated by between 4 and 6 arcmin, and for 10 per cent the nominal cluster positions differ by more than 9 arcmin or more than 0.5 Abell radii.

In order to eliminate multiple entries from our tentative sample of RASS-detected Abell and Zwicky clusters, we exclude from our list all Zwicky clusters that lie within 10 arcmin of an Abell cluster, *if both have been assigned the same X-ray source in the*

---

[5] The conversion from angular to metric separations is performed at the redshift of the respective Abell cluster.

cross-correlations. Having thus eliminated 137 of the 354 Zwicky clusters in our list, we are left with a tentative sample of 446 Abell and Zwicky clusters with SASS count rates of at least 0.1 count s^{-1}. Including the 19 nearby Abell clusters that might have been missed by the SASS, we arrive at a total of 465 candidate clusters for the BCS.

So far, all our candidate clusters have been selected from optical cluster catalogues which can be trusted to be reasonably complete for optically rich clusters at redshifts $z \lesssim 0.2$ (Huchra et al. 1990; Scaramella et al. 1991). However, at redshifts higher than about 0.2, even very rich clusters start to become inconspicuous on the optical plates used in the compilation of these catalogues. Incompleteness is a potential problem also at the low-redshift end ($z \lesssim 0.07$), where any X-ray flux-limited sample (such as the BCS) will be dominated by low-luminosity systems that may not be optically rich enough to be included in optical catalogues. This effect of a thinning-out at low redshifts can be clearly seen in the L_X-z distribution of the XBACs (EVB).

To overcome these problems, we use the X-ray source extent to find galaxy clusters not included in the Abell and Zwicky catalogues. The extent parameter supplied by the SASS is the Gaussian width of the radial source profile that is in excess of the instrumental resolution, i.e. the PSPC point spread function (PSF) for the All-Sky Survey. Although a Gaussian is not really an adequate description of the surface brightness distribution of extended X-ray sources such as clusters of galaxies, the SASS extent parameter is none the less very useful for flagging possibly extended emission. As was shown by Ebeling et al. (1993), RASS X-ray sources with a SASS extent value in excess of 35 arcsec are almost exclusively clusters of galaxies (Fig. 6). We emphasize that while, at high Galactic latitude, a significant SASS extent comes close to being a sufficient criterion for a cluster identification (it is not perfect, owing to the possibility of blends of close source pairs), it is not a necessary condition. The latter is demonstrated by a number of Abell clusters classified as point sources by the SASS (see the lower left of Fig. 6), and is discussed in depth in Section A4.

We therefore select from the list of SASS detections with count rates greater than 0.1 count s^{-1} all 406 sources that fall within our study area ($\delta \geq 0°$, $|b| \geq 20°$) and feature an SASS extent of at least
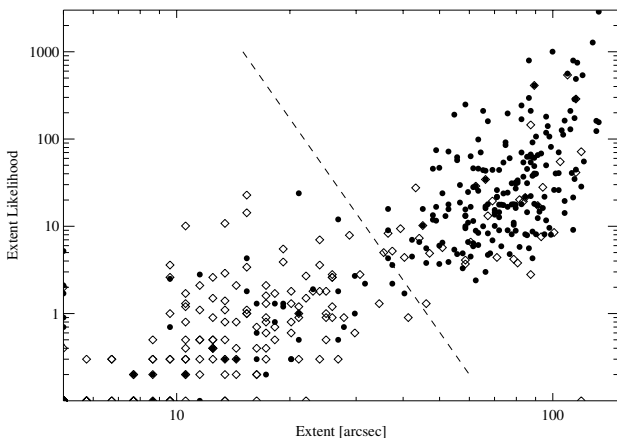

Figure 6. The distribution of the SASS source parameters X-ray extent likelihood and X-ray extent for rich Abell clusters (filled circles) and random field sources (open diamonds). Note that, while both samples comprise the same number of sources, many of the randomly selected sources have X-ray extents of zero and do not feature on this logarithmic plot. [Reproduced, with permission, from Ebeling et al. (1993).]

35 arcsec. 218 of these are already included in our list on the grounds of their being associated with Abell or Zwicky clusters; another 11 can be readily discarded as multiple detections of very bright, nearby sources like M87. We add the remaining 177 to our list to obtain, finally, a sample of 642 BCS candidates.

For all of these we request from the RASS data archive PET data in $2° \times 2°$ fields around the optical cluster position or the position of the extended SASS source. As the PET file for any field contains all photons accumulated during the whole RASS in the respective region, the accumulated exposure times in these fields are sometimes much longer than those available in the SASS strips; up to 8200 s are attained. The median value of 460 s, however, is very similar to the one for the initial strips.

3.2 The VTP-based sample

A fresh search for X-ray emission from clusters of galaxies in these data is now required not only because of the greater depth of the PET maps; we also want to overcome the limitations of the SASS detection algorithms that have been used on the RASS strip data. As mentioned before, the SASS has difficulties characterizing or, for that matter, even reliably detecting extended emission. The cause for this lies in the basic design of the algorithm as a point source detection algorithm which is primarily sensitive to highly localized and quasi-spherical intensity variations. We therefore reprocess the RASS data in the PET fields with VTP (for 'Voronoi tesselation and percolation'), an algorithm developed for the detection and characterization of sources of essentially arbitrary shape (Ebeling & Wiedenmann 1993; Ebeling 1993). VTP works on the individual photons rather than on spatially binned representations of the data; also, it does not require any model profiles to be fitted to the detected emission in order to determine fluxes, all of which makes the algorithm extremely versatile and flexible. The reprocessing of the data with VTP is crucial in order to obtain reliable fluxes for the clusters in our sample: for clusters of galaxies, raw SASS fluxes are found to be typically too low by about a factor of 0.5; for nearby clusters the misassessment can even exceed one order of magnitude (EVB).

At the time of writing, more than 98 per cent of our 642 BCS candidate clusters have had their PET fields processed by VTP. For 11 sources, either PET files are not available or their VTP processing has been delayed owing to very high photon counts in a few fields at high ecliptic latitude which cannot be processed in one go by VTP. In order to assess the impact of missing fields on the completeness of the BCS, we have tried to identify the corresponding SASS sources. We find the following.

(i) The only source of these 11 that is associated with an Abell cluster (A2506) is $0.37r_A$ away from the optical cluster centre and coincides within 7 arcsec with a close pair of bright stars of $m_V \sim 7$.

(ii) Of the eight sources tentatively assigned to Zwicky clusters, six feature X-ray/optical separations of 9 arcmin or more and are thus very likely to be chance coincidences with non-cluster sources. Indeed, three of them have firm stellar identifications, another two coincide with catalogued active galactic nuclei (AGN), and only for one is the identification (although clearly non-cluster) ambiguous in as much as the source is probably a blend of emission from an *IRAS* galaxy and NGC 6521.

(iii) The two sources without VTP results from our list of 177 sources classified as extended by the SASS are identified with a star and a QSO, respectively. With SASS count rates in excess of 0.3 count s^{-1}, both of these point sources are sufficiently bright for the

instrumental PSF to be sampled with good statistical accuracy. The simple approximation to the PSF used by the SASS (a single Gaussian) is known to lead to spurious extents for bright point sources. Also, both sources lie within 2° of the north ecliptic pole (NEP), so that small inaccuracies in the attitude solution of the *ROSAT* satellite in the immediate vicinity of the NEP may contribute to the erroneous extent classification.

Thus nine of the 11 sources for which VTP results are not available are associated with non-cluster counterparts. The two candidates left that might be true cluster detections missing from our tentative list are both Zwicky clusters, namely Z3803 and Z8417. The former is a previously detected EMSS cluster, and the latter, although previously undetected, has a galaxy distribution consistent with a cluster at a redshift $z \gtrsim 0.2$. Thus both are accepted as cluster identifications. Summarizing, we can say that the incompleteness of 2 per cent in our BCS/VTP data base has no significant implications for the completeness of the BCS as a whole.

The sources detected in the 631 PET fields processed by VTP are then screened for possible blends of close source pairs. Such blends occur because VTP makes no assumptions about the intrinsic surface brightness distribution of any source that it considers to be a significant enhancement over the background. As a consequence, the VTP percolation algorithm needs to be forced to stop at the interface of two sources with detected surface brightness profiles that overlap, in order to keep the two sources separated. Deblending was required for 55 VTP sources. Note that direct deblending is only feasible for bright blends with components that are clearly discernible as separate sources on the RASS images (see fig. 8 of EVB for an illustration of the deblending procedure). The majority of blends, however, occur near the detection limit and typically involve sources that are too faint to be resolved in the RASS. Falling well below the flux limit, these faint blends are of no immediate concern for the BCS proper; however, if not recognized, they would contribute significantly to the number of X-ray-extended sources at the faint end of the cluster $\log N - \log S$ distribution presented in Section 7.2.1. Our procedure of identifying and eliminating unresolved blends is discussed in Section 5.

Just as before with the SASS sample, we then introduce a count rate cut for the VTP detections, thereby eliminating sources at flux levels at which any sample would be intrinsically incomplete owing to the limited depth of the RASS alone. A threshold value of 0.07 count s^{-1} is chosen for this purpose. As will be shown in Section 7.2.1, VTP sources below this count rate threshold can be safely ignored for our purposes as, statistically, fewer than one of these faint sources would reach final energy fluxes in excess of 2×10^{-12} erg cm^2 s^{-1} (0.1–2.4 keV), which is the flux level at which the RASS starts to become incomplete in the northern hemisphere owing to exposure time limitations. Application of this count rate limit leaves a sample of 1650 VTP sources.

Subsequently, the merged VTP X-ray source list for all PET fields is correlated against the Abell catalogue, and, just as before, a 95 per cent complete sample of coincidences is compiled (see Fig. 7). The maximal separation between the included matches is 0.470 Abell radii. This sample now comprises 334 unique X-ray sources corresponding to 298 different Abell clusters, with some 11 per cent of the entries being caused by positional chance coincidences (as indicated by the dot–dashed line in Fig. 7).

For the Zwicky clusters the cross-correlation with the VTP source list results in 365 true coincidences. Fig. 8 shows the cumulative number of coincidences as a function of angular separation. A 95 per cent complete sample consists of 461 unique
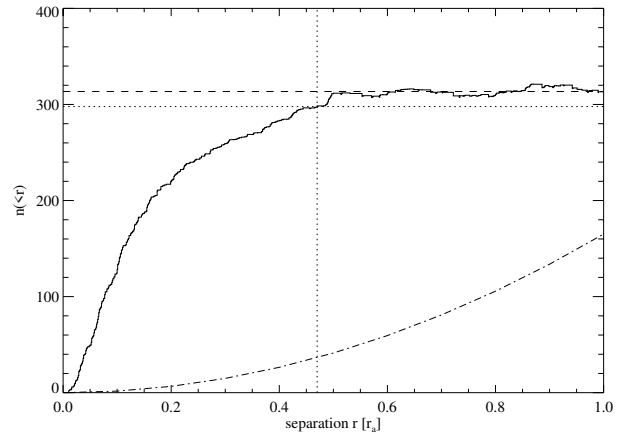

Figure 7. The cumulative number of coincidences in the cross-correlation between the ACO catalogue and the RASS X-ray source list provided by VTP as a function of the X-ray to optical source separation. Only X-ray sources with VTP count rates higher than 0.07 count s^{-1} are considered. A parabolic background component (the dot–dashed line) has been subtracted. The dashed line marks the total number of true coincidences. The dotted lines, finally, mark the selected maximal separation and the corresponding number of true coincidences.

Figure 8. The cumulative number of coincidences in the cross-correlation between the Zwicky cluster catalogue and the RASS X-ray source list provided by VTP as a function of the angular distance between the X-ray source and the optical cluster position. Only X-ray sources with VTP count rates higher than 0.07 count s^{-1} are considered. A parabolic background component (the dot–dashed line) has been subtracted. The dashed line marks the total number of true coincidences. The dotted lines, finally, mark the selected maximal separation and the corresponding number of true coincidences.
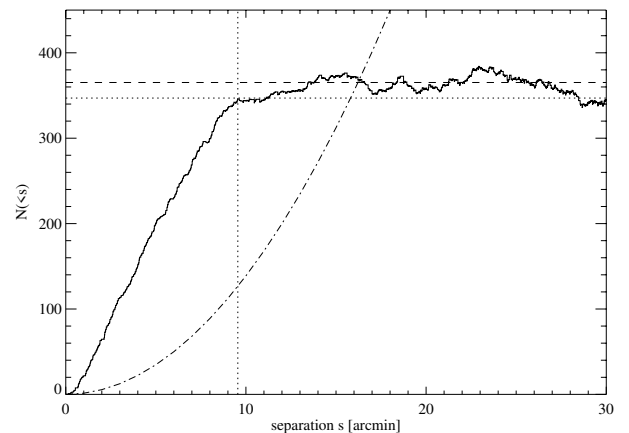
X-ray sources associated with 461 Zwicky clusters at separations of up to 9.55 arcmin. Just as before for the tentative sample from the cross-correlation with the SASS source list, the contamination of this sample by chance coincidences is high: almost 27 per cent of the correlation pairs within a maximal separation of 9.55 arcmin are expected to be coincidental.

Note that the number of true coincidences found in the cross-correlations (the number at which the cumulative distributions of Figs 3, 4, 7 and 8 level off) is considerably higher when the VTP source list is used. More than 60 per cent more Zwicky clusters are found in the cross-correlation with the VTP source list than in the previous one with the original SASS list; for Abell clusters the increase in detections is less dramatic but amounts still to more than 30 per cent. The reasons for this rise are twofold. First, and most importantly, the VTP source list has a lower count rate limit than the

SASS list. Consequently, a number of (mostly faint) X-ray sources get included in the VTP-based sample as serendipitous detections of Abell and Zwicky clusters in our PET fields. This effect is amplified by the presence of a few PET fields with exposure times much longer than those of the strip data used in the first SASS analysis. A second cause for the increase in cluster detections lies in the source detection procedures themselves, as nearby low-surface-brightness sources missed or misassessed by the SASS are now detected by VTP.

Again, there is considerable overlap between the X-ray source lists obtained from the correlations between the VTP source list and the Abell and Zwicky cluster catalogues, respectively. Merging the two samples yields a list of 612 unique VTP sources with count rates of at least 0.07 count s^{-1} that have been associated with Abell or Zwicky clusters in the extragalactic part of the northern hemisphere.

We still have to incorporate the list of sources flagged as extended by the SASS. As the PET fields around them have also been reprocessed by VTP, we now have to find the VTP counterparts of the SASS sources upon which the PET fields are centred. This leads to the inclusion of another 132 VTP sources with count rates in excess of 0.07 count s^{-1} that lie within 4 arcmin of the original SASS position and have not yet been included as possible detections of Abell or Zwicky clusters. Note that the number of VTP detections of SASS-extended sources thus included (132) is considerably lower than the number of extended (non-Abell and non-Zwicky) SASS sources from which we started (177, for 175 of which we have PET fields). This discrepancy is mainly due to some two dozen 'SASS crashes', i.e. detections of, in general, very bright point sources that the SASS erroneously flagged as extended. Since these sources also have large positional errors of typically 10 arcmin, they are excluded from entering our sample by the cut-off at a respective SASS–VTP source separation of 4 arcmin. Fig. 9 illustrates the clear separation between regular SASS detections and 'SASS crashes'. Note the significant rise in the number of true coincidences at some 10 arcmin caused by bright point sources with large errors in the SASS source position.
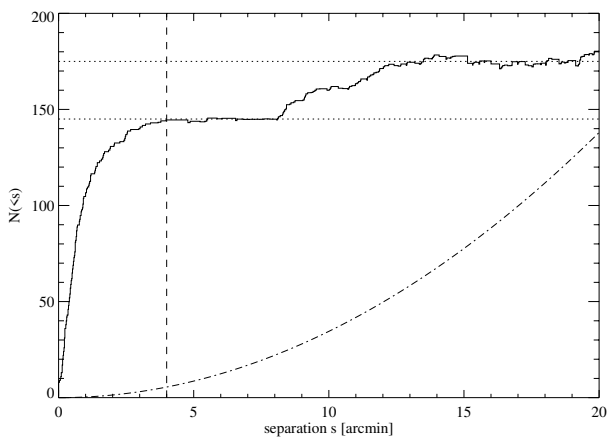

Figure 9. The cumulative number of coincidences in the cross-correlation between the SASS extended sources that do not coincide with either Abell or Zwicky clusters and the RASS X-ray source list provided by VTP, as a function of the angular distance between the SASS and VTP X-ray source positions. A parabolic background component (the dot–dashed line) has been subtracted. Note the jump in the total number of true coincidences highlighted by the dotted lines. The dashed vertical line marks the maximal allowed separation for sources accepted as real detections of potentially extended X-ray sources.

Having included the VTP counterparts of bright X-ray sources classified as extended by the SASS, we are left with one more class of potential cluster detections, namely the sources classified as extended by VTP that are not yet included. Since, contrary to the SASS, VTP does not assume any model for the radial source profile in the source detection procedure, it necessarily cannot provide an immediate measure of the source extent. However, VTP does determine source extents at a later stage when correcting the detected source count rates for low-surface-brightness emission that has escaped direct detection. In order to ensure the greatest possible completeness for our tentative sample, we use a deliberately low threshold for the VTP source extent of $r_c = 15$ arcsec (see Section 4 below) and add another 439 X-ray sources to our list, bringing the total up to 1183 VTP sources. Including in our list of cluster candidates all sources classified as extended by either the SASS or VTP also allows us quantitatively to assess the efficiency of selecting a cluster sample purely by the X-ray characteristics of the sources (see Appendix A).

4 COUNT RATE CORRECTIONS AND THE DETERMINATION OF VTP SOURCE EXTENTS

In the presence of background radiation, the emission directly detectable by any source detection algorithm is always limited to some fraction of the total flux. Hence the raw VTP count rates have to be corrected for the low-surface-brightness emission in the far wings of the source that has not been detected directly. While usually small for point-like sources, the 'missing' fraction of the total projected source emission can be substantial for extended sources such as clusters of galaxies. A correction to the directly detected emission such as the one outlined in the following thus plays a crucial role in the compilation of any X-ray cluster sample.

Since the procedure employed to this end is described in detail by EVB, we give only a brief summary here. The algorithm uses two different kinds of source profile. The first one applies to extended cluster emission that is resolved in the RASS and assumes a King model, i.e. a radial surface brightness profile of the form

$$\sigma(r) = \sigma_K(r) = \sigma_0 \left[1 + (r/r_c)^2 \right]^{-3\beta + 1/2}$$

(Cavaliere & Fusco-Femiano 1976), where $\sigma(r)$ is the projected surface brightness as a function of radius. Fixing the beta parameter at a value of 2/3 (Jones & Forman 1984), we can derive both the normalization σ_0 and the core radius r_c from the VTP source characteristics. Note that it is only in *correcting* the detected count rates that a specific model for the source profile and, in particular, spherical symmetry is assumed for VTP detections.

The second source profile assumed in the count rate correction procedure is that of a point source, i.e.

$$\sigma(r) = \sigma_{ps}(r) = \frac{s_{ps}}{2\pi r} \delta(r),$$

where s_{ps} is the total source count rate and $\delta(r)$ is Dirac's delta function. This model is applied to cluster emission that is not resolved as extended in the RASS (see below and Section A1 for a discussion of the VTP extent parameter).

The expected observed surface brightness distribution $\tilde{\sigma}(r)$ is the convolution of the intrinsic surface brightness distribution of the source $\sigma(r)$ with the instrument response:

$$\tilde{\sigma}(r) = \int_0^{2\pi} \int_0^\infty \sigma(|\boldsymbol{r} - \boldsymbol{r}'|) \, \mathrm{PSF}(r') \, r' \, \mathrm{d}r' \, \mathrm{d}\phi. \quad (1)$$

For the RASS, the telescope point spread function, PSF(r), is the weighted average of the PSFs at all off-axis angles. PSF(r) has been

computed for several photon energies by Hasinger et al. (1994); we employ a numerical representation of PSF(r) for $E = 1$ keV (De Grandi, private communication) that was shown to be in excellent agreement with the source profiles found for RASS-detected AGN (Molendi, private communication).

As described in more detail in EVB, the free parameters of the model profile $\tilde{\sigma}(r)$ can be derived from observed source characteristics without any radial fitting. The quantities used are the total detected count rate, which must equal the integral over the model profile out to the effective detection radius, and the surface brightness level relative to the background, used as the equivalent of a percolation radius in VTP's percolation step.

The true total source count rate can then be determined from

$$s_{\text{true}} = 2\pi \int_0^\infty \sigma_K(r) \, r \, \mathrm{d}r = \frac{\pi \, \sigma_0 \, r_c^2}{3 \, (\beta - 1/2)} \tag{2}$$

(for clusters of galaxies), or

$$\frac{s(r_{\text{VTP}})}{s_{\text{true}}} = 2\pi \int_0^{r_{\text{VTP}}} \text{PSF}(r) \, r \, \mathrm{d}r \tag{3}$$

(for point-like sources).

Clearly, our assumption that the observed emission from any cluster can be described by either of these model profiles represents an oversimplification, in particular in the presence of cooling flows. However, at no stage of the flux correction procedure is the model profile from equation (1) fitted to the actually observed surface brightness distribution. Although we do assume a specific model, it is only its integral properties that enter, which is why deviations of the true distribution from the assumed model (such as the extremely peaked surface brightness profile observed in the very core of cooling flow clusters) have much less effect on the result than they do for the fitting procedures employed by conventional source detection algorithms. As, in all but the largest cooling flow clusters, it is the emission from outside the cooling core rather than from the cooling flow itself that dominates the overall X-ray luminosity of the cluster (White, Jones & Forman 1997), we are confident that our integral correction to the total emission will not be largely affected by the presence of cooling flows (this is confirmed by Fig. 12 which is discussed later in this section).

However, as far as the initial SASS detections are concerned, the presence of cooling flows may cause some bias. As mentioned before, the SASS was designed as a point source detection algorithm. Thus cooling flow clusters are likely to be preferentially detected and therefore over-represented in the sample of SASS clusters from which our analysis started. We have no means to correct for this bias, other than to rely on VTP serendipitously to detect low-surface-brightness emission from non-cooling flow clusters that the SASS has missed. Section 7.1 discusses the importance of these serendipitous detections in detail. Once a cluster is detected (or redetected) by VTP, the presence of a cooling flow will not greatly affect the flux correction procedure.

The lack of any radial fitting in the count rate correction procedure entails that, for any particular cluster, the value for the cluster core radius r_c determined in the flux correction process cannot be expected to be as accurate as the results of a detailed imaging analysis of pointed data. Rather, it should be seen as a statistical parameter that allows the extent of the source and the fraction of the cluster emission that has escaped direct detection to be assessed. In the following, we will use the term 'VTP extent' as a synonym for r_c.

The distribution of VTP extents (r_c) for the 1650 sources detected by VTP at count rates in excess of 0.07 count s^{-1} in the 631
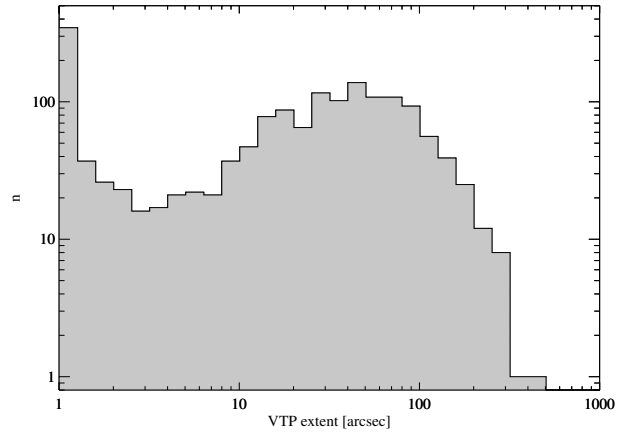

Figure 10. The distribution of VTP source extents for the 1650 sources in our PET fields with VTP detected count rates in excess of 0.07 count s^{-1}. Sources with extent values below the plotted range have been assigned an extent of 1 arcsec. Note the gap in the distribution, indicating that source extents of less than about 10 arcsec are not resolved in the RASS.
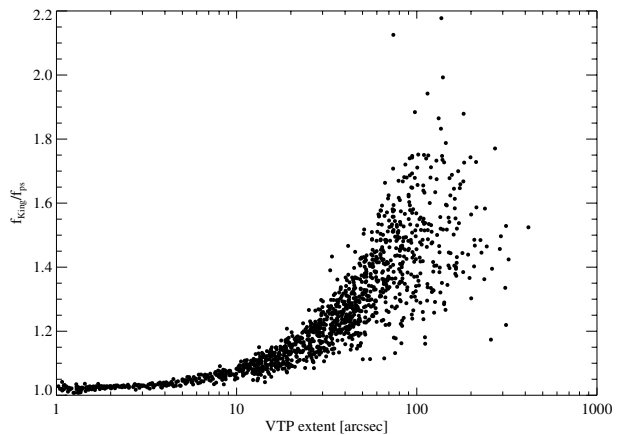

Figure 11. The ratio of the count rate correction factors (King model/point source) for the sources of Fig. 10 as a function of VTP extent, i.e. core radius. Note how the correction factors for the two models converge for vanishing extent values.

processed PET fields is shown in Fig. 10. Note that the distribution peaks at about 40 arcsec, indicating that sources with an extent parameter considerably below this value are not reliably resolved as extended in the RASS. When applying the flux correction factors, we take the conservative approach to consider only sources with an extent of less than 15 arcsec to be point-like and apply equation (3), whereas sources featuring VTP extents greater than this threshold value are considered to be potential clusters the count rates of which are corrected according to equation (2). As the results from equations (2) and (3) converge as the source extent obtained from the King model decreases (see Fig. 11), and differ typically by only 10 per cent or less for extent values smaller than 15 arcsec, is does not really matter where exactly the line between point sources and extended sources is drawn. Note, however, that, even for the most extreme case of a very compact cluster at a redshift of $z = 0.5$ (which is higher than that of any cluster detected so far in the RASS), a metric core radius of only 150 kpc would still correspond to more than 20 arcsec on an angular scale. Thus we do not believe that the use of the correction factor from the convolution of the King

model with the RASS PSF is scientifically justifiable at extent values significantly below $r_c \sim 15$ arcsec.

It ought to be noted here that we do not expect all sources with VTP extents in excess of 15 arcsec to be really physically extended. Undoubtedly, a considerable fraction of the sources with extents between about 10 and 40 arcsec will be blends near the VTP detection limit. These will be eliminated from our sample at a later stage when we assess the physical identifications of all sources in our tentative sample from their combined X-ray/optical appearance. At this point we are not yet concerned with source identification – rather, we want to mark *potentially* extended sources for inclusion in our cluster candidate list. At the same time, the above procedure provides us with total count rates (fluxes) for all sources that will finally remain in our sample.

While the count rate correction procedure outlined above recovers emission that has escaped direct detection for point-like and extended sources alike, it assumes a single surface brightness profile and does thus not account for emission from more than one contributor. For clusters of galaxies this means that any contribution from point sources (usually AGN) or cooling flows to the overall emission will result in an overestimation of the *detected* count rate if interpreted wholly as emission from an isothermal ICM. Subsequently, the overestimation of the *corrected* count rate will be even greater as both the diffuse and the point-like emission get corrected assuming the same King model. Hence, the raw (detected) VTP count rates for clusters will be too low and the corrected ones will be too high.[6] Since, at the angular resolution and sensitivity of the RASS, it is impossible to quantify the point source or cooling flow contribution to the X-ray emission from all but the brightest and most nearby clusters of galaxies, we resort to a final heuristic correction to account for this problem by adopting the geometric mean of the detected and the corrected count rates as the best VTP estimate of the true count rate from diffuse ICM emission.

The accuracy of these final RASS–VTP count rates of galaxy clusters can be assessed by comparing them with the PSPC broad-band count rates obtained in pointed observations (POs) of the same clusters. Such a comparison has been made by EVB for their XBACs, the fluxes of which were derived in exactly the same way as those for the BCS. Fig. 12 shows RASS–VTP and PO count rates for 100 ACO clusters for which both RASS and pointed data are available. Note the excellent agreement between the VTP count rates based on RASS exposure times of typically 400 s and the values obtained from pointed PSPC observations that are typically 25 times deeper (median PO exposure: 10.2 ks). Since the sample of 100 clusters used in this comparison contains both clusters with and without cooling flows, the good agreement between the RASS–VTP count rates and the total (aperture) count rates obtained from pointed data confirms our earlier statement that the presence of cooling flows does not greatly affect our flux correction procedure. Using the data shown in Fig. 12 to calibrate the 1σ uncertainty Δs in the RASS–VTP count rates, EVB find

$$\frac{\Delta s}{s} = 2.29 \, (s \, t_{\mathrm{exp}})^{-0.48}, \tag{4}$$

where s is the final VTP count rate and t_{exp} is the RASS exposure time.

---

[6] Using VTP results obtained for data from simulated PSPC cluster observations, Scharf et al. (1997) recently pointed out that the tendency for the corrected VTP count rates to be too high may in part also be attributed to 'positive background noise', i.e. upward fluctuations in the observed background photon density, around the cluster that gets included in the VTP detection.
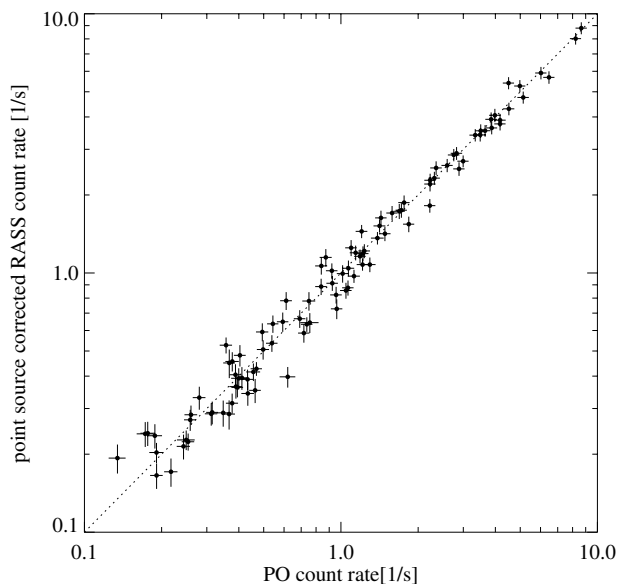
Figure 12. PSPC broad-band count rates for 100 ACO galaxy clusters as derived from RASS data using VTP, compared with the corresponding values obtained from PO. Note that the contribution from point sources is *excluded* in the PO data. The error bars allow for a 5 per cent systematic uncertainty in addition to the Poissonian errors. [Reproduced from EVB.]

The overall agreement between VTP and PO fluxes is thus very good. However, one might suspect that the $2° \times 2°$ fields in which the VTP analysis was performed could be too small to cover fully the very extended ICM emission from the most nearby clusters of galaxies, resulting in VTP fluxes that are too low. Inspecting the RASS X-ray images of bright and nearby clusters, we find that our limited field size could be a potential problem only for three systems, namely the Perseus, Coma and Virgo clusters.

Owing to its low Galactic latitude, the Perseus cluster is not a member of the BCS. For Coma, VTP obtains a final flux of 3.19×10^{-10} erg cm^{-2} s^{-1}, in perfect agreement with the value of 3.2×10^{-10} erg cm^{-2} s^{-1} found by Briel, Henry & Böhringer (1992) who analyse the RASS data for Coma out to almost twice the radius of our PET fields, namely $1°75$. The X-ray emission from the Virgo cluster, however, is extended over more than $10°$ on the sky; thus there can be no hope to recover its X-ray flux completely from the data in our $2° \times 2°$ field centred on M87. VTP finds a total flux of 6.7×10^{-10} erg cm^{-2} s^{-1}, some 37 per cent of the total flux measured by Böhringer et al. (1994) in an analysis of the RASS data in a $12° \times 12°$ field. We correct for the flux outside our PET field by scaling the VTP count rate, flux and luminosity of Virgo accordingly, i.e. by a factor of 2.74.

5 REMOVAL OF NON-CLUSTER SOURCES

The tentative sample of 1183 RASS–VTP sources described in Section 3 was compiled with the goal of maximal completeness. We included X-ray sources out to considerable distances from the optical centroids of Abell and Zwicky clusters as potential cluster detections, and, for the X-ray-selected systems, accepted VTP sources with extent values as low as 15 arcsec. The price to be paid for the high degree of completeness thus achieved is severe contamination by non-cluster sources. A large part of the contamination is caused by random coincidences between the optical Abell/Zwicky cluster positions and non-cluster X-ray sources, but

also by true coincidences with point sources like QSOs or AGN which are members of otherwise X-ray-faint clusters of galaxies. Besides that, our tentative sample will also contain a substantial number of apparently extended VTP sources that are in fact blends of fainter sources that cannot be identified as such from the X-ray images alone.

In order to identify chance coincidences as well as cluster-related point sources, we cross-correlated our source list with the objects in the NASA/IPAC Extragalactic Database (NED). We also obtained 12×12 arcmin^2 optical images from the digitized Palomar Observatory Sky Surveys (POSS, first- and second-generation where available) using the SkyView and STScI WWW interfaces,[7] and looked for possible optical identifications. Wherever possible, we obtained E magnitudes and $O-E$ colours from the APM object catalogue (Automated Plate Measuring machine, Irwin et al. 1994) for galaxies or stellar objects thought to be the true source of the observed X-ray emission.

Also, we searched the *ROSAT* public archive of pointed PSPC and High Resolution Imager (HRI) observations for further X-ray data on our cluster candidates. The deeper X-ray images thus obtained plus a few more from non-public POs awarded to the authors were then examined in order to ensure that the emission detected by VTP in the RASS data is genuinely extended, indicating that it originates indeed from a diffuse ICM.

We emphasize that, although we will loosely refer to the process described in the following as the identification procedure, it is not our goal to identify completely all X-ray sources in our tentative sample. The only distinction that we attempt to make for all sources is the one between X-ray detections of diffuse emission from clusters of galaxies and X-ray sources for which the emission is of a different origin. Although this step often entails identifications if the optical non-cluster counterpart is either obvious or well-known, there are cases where we discard sources as not cluster-related without having a secure alternative identification. The majority of these are apparently extended, faint X-ray sources with positions on the sky that do not coincide with any discernible galaxy concentration but that have at least one plausible stellar optical counterpart that could account for part of the X-ray emission. Such sources are consequently classified as likely blends of faint point sources.

Prior to assessing the available data on all our cluster candidates, we need to establish a value for the radius of the error circle around the nominal VTP X-ray source position within which to search for optical counterparts. A good estimate of the intrinsic accuracy of the VTP source positions can be obtained by cross-correlating them with the sources of the RASS 1RXS catalogue (also known as the Bright Source Catalogue: Voges et al. 1996) which is a compilation of RASS sources found by the standard SASS point source detection algorithms in the merged RASS photon data (see also Section 10). For bright point sources, the 1RXS positions are expected to be accurate to about 10 arcsec, of which 6 arcsec are assumed to be due to systematics. From the cumulative distribution of the separations between VTP sources and their 1RXS counterparts, we derive a 90 per cent error radius of 1 arcmin around the positions of VTP point sources. For VTP point sources with actual counterparts in the 1RXS sample, we use the more accurate source positions from the latter sample and adopt an error circle of 30-arcsec radius in the identification process. For extended VTP sources, we find significantly larger separations between the VTP

and the 1RXS positions. However, in general it is not clear which of the two data sets can be considered to be the more accurate: SASS uses a source profile that is inappropriate for extended emission and likely to bias the source position toward the most point-like feature within the emission region; VTP, on the other hand, tends to blend sources if both the detection and count rate thresholds are low. For our present purpose of discarding non-cluster sources we take a conservative approach and adopt a value of 2 arcmin for the search radius around the positions of extended VTP sources. VTP-extended sources that have point-like counterparts in the 1RXS sample within 2 arcmin are treated as potential blends (not all components of which have necessarily been detected by SASS) if likely optical counterparts are found within 30 arcsec of these point-like 1RXS sources.

In the following we derive criteria designed to discriminate between clusters and non-cluster sources using the X-ray properties of the VTP detections and the optical properties of the most likely APM counterparts within the X-ray error circle. We stress that, although a preliminary decision is made based on these criteria, no source is discarded from our list of cluster candidates without careful visual inspection of all the data at hand.

A brief summary of this procedure covering all steps detailed in Sections 5 and 6 is given in Table 1.

Table 1. Overview of the 'identification' procedure used to discriminate between clusters and non-cluster X-ray sources, starting from our initial list of 1183 VTP sources selected as cluster candidates and ending at our final sample of 442 likely clusters. See Sections 5 and 6 for details.

number of VTP sources	action taken
1183	START: initial list of candidate clusters
− 111	excluded as non-clusters based on pointed data
− 71	excluded as catalogued AGN or QSOs without pointed data
− 83	excluded as catalogued bright stars without pointed data
− 62	excluded as likely stars (stellar object with $E \leq 12$ within error circle)
− 306	excluded as likely AGN or QSOs (object with $E \geq 12$, $O - E < 2$ within error circle)
− 88	excluded as too soft (X-ray hardness ratio below 95 per cent confidence limit for clusters)
+ 30	brought back as likely clusters after visual inspection of all data at hand (overrides previous, automatic assessment)
− 24	excluded as unlikely clusters after visual inspection of all data at hand (overrides previous, automatic assessment)
− 1	excluded (Z569 – cluster but just south of $\delta = 0°$)
− 1	excluded (unrelated source erroneously associated with Z5948)
− 1	excluded as a blend of fainter sources after visual inspection of all data at hand (overrides previous, automatic assessment)
+ 14	included as faint (count rates of less than 0.07 count s^{-1}) fragments of clearly extended main cluster emission
− 22	fragments merged with main body of emission from 15 different clusters
− 2	excluded as below the 0.07 count s^{-1} count rate threshold even after merging of fragments
+ 1	A625b included to join A625a although count rate is below 0.07 count s^{-1}
− 14	excluded as underluminous [$L_X(0.1-2.4$ keV$) < 5 \times 10^{42}$ erg s^{-1}]
442	END: final list of likely clusters

5.1 Sources with pointed *ROSAT* data and the significance of local galaxy overdensities

We begin the identification process by examining the 246 sources for which pointed *ROSAT* data are available. Of these 246, we confirm 135 as clusters on the grounds that their X-ray emission is genuinely extended in the pointings. More than 83(93) per cent of these 135 sources feature RASS–VTP extents in excess of 30(15) arcsec, and all of them are coincident with obvious galaxy over-densities on the optical plates. We attempt to make the latter statement more quantitative with the help of the APM galaxy counts in the vicinity of the X-ray source (we use the magnitudes and number counts from the E plates in all of the following). We compute the surface densities of APM galaxies and blends in circles of 2.5-, 5- and 7.5-arcmin radius around the VTP source positions down to 18th and 19th magnitudes respectively, and compare them with the mean surface density of galaxies on the respective optical plate. The statistical significance of any overdensity is then deter-mined using Poisson statistics, and the highest of the six significances (for two limiting magnitudes in each of three apertures) measured for each source is adopted as the final value. We find more than 81 per cent (110 out of 135) of the clusters confirmed in pointed observa-tions to feature galaxy overdensities that are significant at greater than the 2σ level. The 25 clusters for which the APM data yield a less significant galaxy overdensity (or none at all) meet one or more of the following criteria: they (i) are very nearby ($z \lesssim 0.05$) groups or poor clusters which often extend over an area greater than our largest aperture, or (ii) are richer systems at redshifts greater than 0.2 with a considerable fraction of the cluster galaxies fainter than 19th magni-tude where the APM galaxy counts begin to become unreliable for the shallowest plates, or (iii) fall on plates for which the mean galaxy surface density was not available and had to be estimated. Although the measurement of galaxy overdensities based on the APM object catalogue can thus support optical cluster identifications, it cannot replace visual inspection of the POSS plates.

This becomes even more evident when the false-alarm rate is considered: more than one-third of the 111 VTP sources identified as non-clusters based on the pointed data feature APM galaxy overdensities that are significant at greater than the 2σ level. This had to be expected though: not only do star–galaxy misclassifica-tions and the presence of spurious APM sources in the vicinity of, for instance, bright stars boost the apparent galaxy overdensities around non-cluster sources; more importantly, most of our PET fields are, by design, centred on known clusters of galaxies, making chance superpositions between non-cluster X-ray sources and regions of increased galaxy surface density more likely than in randomly selected fields. A high APM value of the local galaxy overdensity is thus neither a sufficient nor a necessary condition for a cluster identification.

We therefore use the APM galaxy overdensity measurements only as one of several statistical indicators to eliminate non-cluster sources: VTP sources with a galaxy overdensity that is significant at less than the 2σ level have a probability of only $\sim$20 per cent of being clusters of galaxies.

5.2 APM colours and magnitudes of confirmed clusters and catalogued AGN, QSOs and stars

In this next step we investigate the distribution of the $O-E$ ($\approx B-R$) colours and $E(\approx R)$ magnitudes of the brightest plausible optical counterpart in the error circles around VTP sources with cluster and non-cluster identifications.

Using all the information at hand, we identify 111 VTP sources with catalogued AGN and QSOs. Since 40 of these 111 have already been flagged as non-cluster sources on the basis of their appearance in pointed *ROSAT* observations (see Section 5.1), the total number of sources identified as non-clusters up to this point is 182. For 83 per cent of the sources identified as AGN and QSOs the tentative optical counterpart is bluer than $O-E = 2$ and fainter than $E = 12$, while the same is true for only less than 4 per cent of the confirmed clusters.

Finally, we search for catalogued bright stars as possible optical counterparts for our VTP detections and accept 92, 85 (92 per cent) of which are brighter than $E = 12$. With nine of these 92 having previously been flagged as non-cluster sources based on pointed data, the total number of identified non-cluster sources rises to 265. We note that the probability of a chance alignment within 30(60) arcsec between a VTP source and a star of APM magnitude $E = 12$ or brighter is less than 1(3.4) per cent, so that the risk of an erroneous identification of a VTP source with a bright star is very small.

5.3 The hardness ratio distribution of VTP sources

Using again as a training set the sample of 135 clusters confirmed by *ROSAT* POs, we establish a 95 per cent lower limit to the spectral hardness ratio (see EVB for details) as a function of the equivalent Galactic column density of neutral hydrogen (Stark et al. 1992). While more than half of the 265 sources discarded so far as non-clusters fall below this hardness ratio threshold,[8] the same is, by design, true for only 5 per cent of the confirmed clusters.

5.4 Removal of unidentified non-cluster sources on the grounds of their X-ray/optical properties

We now apply the criteria defined above to remove from our list of cluster candidates all sources that are likely to be of non-cluster origin. In addition to the 265 sources eliminated as point sources or catalogued AGN, QSOs and stars as described in Sections 5.1 and 5.2, we

(i) flag 62 sources as stars using the criterion defined in Section 5.2 (stellar counterpart brighter than $E = 12$ within the error circle),

(ii) mark another 306 sources as likely AGN or QSOs using the criterion defined in Section 5.2 ($E \geq 12$, $O-E < 2$),

(iii) and finally flag another 88 sources with X-ray hardness ratios that fall below the 95 per cent lower limit for clusters (see Section 5.3).

Altogether we thus mark 456 X-ray sources as unlikely to be of cluster origin on statistical grounds. However, since none of the applied exclusion criteria is strictly *sufficient*, we expect some 5 per cent, or 23, of these 456 sources to be clusters, despite the fact that they lie close to a bright star, contain a very blue central galaxy, or feature an unusually low X-ray hardness ratio. After careful visual inspection of all tentatively discarded sources, we override our previous non-cluster assessment for 30 sources that appear to be bona fide clusters from their combined X-ray/optical appearance, bringing the number of sources in our sample of likely clusters back up to 492 ($= 1183 - 265 - 456 + 30$).

As our elimination criteria do not constitute a *necessary* set of conditions for a source to be of non-cluster origin, there will also be

---

[8] Given by $-0.39 + 0.83 \log n_H$ with n_H in units of 10^{20} cm^{-2}.

a number of sources in this list of 492 that are in fact not clusters but e.g. X-ray-bright stars with $E > 12$ or AGN with colours redder than $O-E = 2$. Statistically, we expect some 11 per cent, or 39, of the 357 sources presently marked as likely clusters without confirmation by pointed data to be of non-cluster origin. Again, we scrutinize all available information and discard a further 24 sources as non-clusters on the grounds that the optical/X-ray appearance of the source rules out a cluster identification. Six of these 24 sources are in fact spurious in the sense that they do not correspond to any well-defined photon overdensity; rather, they are VTP detections of large-scale background variations that extend over a significant fraction of the $2° \times 2°$ PET field. Other sources either have obvious non-cluster counterparts on the optical plates which, however, fail to meet our exclusion criteria (e.g. very bright isolated spiral galaxies), or feature conflicting X-ray and optical properties in the sense that they are clearly point-like at the resolution of the RASS but have been associated with very nearby clusters with galaxy distributions that extend over tens of arcminutes. Three sources are eliminated based on deep CCD images taken with the University of Hawaii's 2.2-m telescope which fail to show a galaxy overdensity down to an R magnitude of 23. We also discard Z569 at this stage since it falls just outside our study area.

In the course of the visual inspection of both the X-ray and the optical images of all our candidate sources, we came repeatedly across very extended VTP detections that do not have any obvious counterparts at all in the optical. The emission from these very diffuse sources is extended over typically several tens of arcminutes and spectrally soft, which is why we excluded the corresponding sources from our list. Note that, although these RASS–VTP detections are not always obvious even to the eye, they are not spurious. RX J0905.4+1731 is a typical example of this type of source and is also detected as an extremely diffuse source at the edge of the field of the PSPC pointing on the quasar 0903+169. This is the same type of source as the one detected first in the RASS by Ebeling et al. (1994), who tentatively classified them as fragments of Galactic supernova remnants.

The visual inspection of all our candidates also causes one further detection of an Abell cluster to be included in our sample. A1758b is more than 0.470 Abell radii away from Abell's optical cluster position and was thu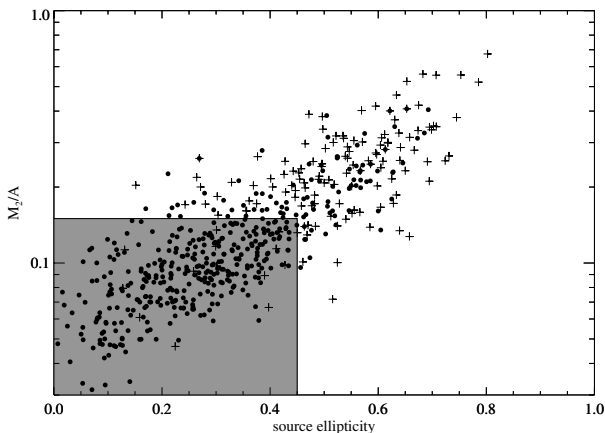s not included in the sample selected from the cross-correlation between the Abell catalogue and all X-ray sources detected by VTP. However, it is picked up later as a possibly extended VTP source (with an extent parameter of 17 arcsec) and joins A1758a. Another source, initially included because it falls within 9.1 arcmin of Z5948, is eliminated at this stage on the grounds that it is point-like in the VTP analysis and clearly unrelated to Z5948 (=A1738) which is detected as a different VTP source at the nominal Abell position.

As mentioned earlier, blended sources become increasingly common as the flux of the sources in question approaches the detection limit. In an attempt to find blended sources that might have been missed by the above screening procedure, we investigate the efficiency of two more source parameters as an additional criterion to discriminate against blends. Fig. 13 shows the ratio of the second moment of the sources' spatial photon distribution, M_2, over the area covered by the source photons, A, as a function of source ellipticity e. Whereas the sources classified as clusters extend over a considerable range of values in both parameters, the sources eliminated so far as likely blends are preferentially found outside the shaded region defined by $e \leq 0.45$ and $M_2/A \leq 0.15$ in Fig. 13. We therefore investigate once more the 94 sources classified as clusters that fall into the realm of blends above the quoted thresholds.[9]

Reassuringly, the re-investigation of these sources does not lead to a substantial change in our initial assessment: only one source previously classified as a cluster is now discarded as a likely blend with a dominant non-cluster component. Essentially, the clusters in the high-ellipticity/high-M_2/A regime can be divided into three categories: clusters with good X-ray photon statistics that are indeed distinctly non-spherical (like A76, A1314 or A2111); sources with poor photon statistics with ellipticity and M_2/A values that are ill determined or with VTP detections that contain shot noise from the vicinity of the source causing the emission to appear more elliptical than it is; and, finally, clusters with emission that is blended with X-rays from other sources that may or may not be part of the cluster but appear more peaked than the diffuse cluster emission. Most of the clusters in the third category have in fact already been classified as possibly contaminated in our initial inspection; the remainder receive their 'contaminated?' flag now.

Altogether we have thus removed 718 X-ray sources from our initial candidate list of 1183 VTP detections, which leads to a cleaned sample of 465 X-ray sources. Although below the count rate limit of 0.07 count s^{-1}, a further 14 VTP detections are added to the source list as fragments of extended cluster emission that has been detected in several pieces by VTP. Like 23 brighter VTP sources already included in our list under the same classification, these detections do not appear to define any obvious substructure in the X-ray emission from the 15 different clusters affected. Following EVB, we therefore merge the multiple detections into one for each of these 15, thereby reducing our VTP source list by 22 entries. Two of the multiply detected clusters fall short of our count rate limit even after the individual components have been merged, and are thus rejected, which leaves us with 455 VTP detections of 455 clusters. Seven of these are subclusters (A625a, A1758a/b, A2197a/b and A2572a/b) detected as separate entities by VTP. The one subcluster missing to complete the above list (A625b) was initially excluded because its VTP count rate lies below

Figure 13. Second moment (M_2) over source area (A) versus source ellipticity e for the VTP detections classified as blends (crosses) and clusters (filled circles). Source ellipticity is defined as $e = 1 - b/a$, where b and a are the minor and major axes of the source, respectively. Note that more than 90 per cent of all blends lie outside the shaded region.

[9] Note that these empirical threshold values have no theoretical foundation but are solely based on the distribution of blends and clusters shown in Fig. 13.

0.07 count s^{-1}. We include it now, which brings the number of clusters in our sample to 456, four of them double.

6 CONVERTING PSPC COUNT RATES INTO FLUXES

The conversion of our final corrected VTP count rates into energy fluxes again follows EVB.

We convert the corrected count rates to proper, unabsorbed energy fluxes using the XSPEC spectral analysis package and assuming a Raymond–Smith-type spectrum with a global metal abundance of 30 per cent of the solar value.[10] Values for the Galactic column density of neutral hydrogen, n_{H}, are taken from the compilation of Stark et al. (1992). Where available, measured X-ray temperatures taken from the compilation of David et al. (1993) are used in the conversion; for the remainder the ICM gas temperature is estimated from the bolometric X-ray luminosity of the clusters. We adopt

$$kT = 2.76 \text{ keV } L_{\mathrm{X,bol,44}}^{0.33}$$

for the $kT-L_{\mathrm{X}}$ relation (White et al. 1997), where $L_{\mathrm{X,bol,44}}$ is the bolometric X-ray luminosity in units of 10^{44} erg s^{-1}. Starting from a default value of 5 keV, kT is then determined from the above relation in an iteration loop. K-corrections are applied using measured cluster redshifts wherever available (357 clusters), and estimates for the remainder of the sample (99 clusters).

In addition to computing fluxes and cluster-rest-frame luminosities in the *ROSAT* broad band (0.1−2.4 keV) and the pseudo-bolometric 0.01−100 keV band, we also determine the respective values for all of our clusters in the energy ranges of previous missions, namely 0.5−2.0 keV (*ROSAT* hard band), 0.3−3.5 keV (*EMSS*) and 2−10 keV (*HEAO-1*), in order to facilitate the comparison of our results with those of previous and future studies.

Using the derived X-ray luminosities in the *ROSAT* broad band, we apply one more cut to our sample and exclude all 'clusters' featuring X-ray luminosities below 5×10^{42} erg s^{-1} (0.1−2.4 keV). Most of these nearby, low-luminosity systems have entered our sample as purely X-ray-selected sources classified as extended by either the SASS or VTP. A total of 14 systems are thus eliminated from our list (among them M31 and M82); one source, A2197b, is kept despite its low luminosity in order to allow us to keep track of all components of multiple systems. This last elimination step leaves us with our final sample of 442 clusters.[11]

7 THE CLUSTER LOG N–LOG S DISTRIBUTION AND THE BCS FLUX LIMIT

Given the rather complicated compilation procedure (different source detection algorithms with different sky coverage, a combination of optical and X-ray criteria in the selection of our initial PET field targets, etc.), one might think that the completeness of the BCS would be difficult to quantify.

Fortunately, this is not the case.

7.1 Inclusion of serendipitous cluster detections

Thanks to having VTP run on all of our 631 2° × 2° PET fields, we have a complete set of *serendipitous* VTP detections that is almost totally independent of the initial selection criteria applied to the

---

[10] We use the solar abundance table of Anders & Grevesse (1989).
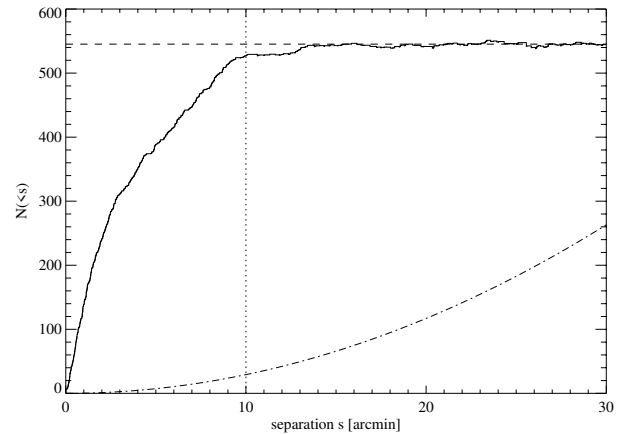[11] Eight of these systems are in fact the components of four double clusters.

Figure 14. The cumulative number of VTP sources with detected count rates higher than 0.07 count s^{-1} from all 631 PET fields as a function of their angular distance from the respective field centres. A parabolic component (the dot–dashed line) describing the background source density of 0.53 deg^{-2} has been subtracted. The fact that the data reach the constant background level (marked by the dashed line) only at separations of about 13 arcmin is due to peculiarities introduced by the 'SASS crashes' discussed in Section 3.2.

SASS source list. The total sky area covered by all PET fields is 2190 deg^2, not much less than $631 \times (1°.8)^2 = 2278$ deg^2 owing to a small amount of overlap between some of our fields. (We remind the reader that the outer 5 per cent of each PET field is actually not processed by VTP but serves as a tessellation margin.) Plotting the cumulative number of all VTP detections with raw count rates in excess of 0.07 count s^{-1} in these 631 fields as a function of their radial separation from the field centre, we find the number of sources per unit area (and above the quoted count rate limit) to converge to 0.53 deg^{-2} at a radius of about 10 arcmin (see Fig. 14). We thus subtract another $631 \times \pi \times (10 \text{ arcmin})^2 = 55$ deg^2 from the above 2190 deg^2 to allow for the central target regions of each field within which detections cannot be considered to be serendipitous, and obtain a total solid angle of 2134.6 deg^2 (or 15.7 per cent of the northern extragalactic sky) that is available for serendipitous VTP detections. We note that no additional corrections for obscuration by extended emission are required: the total area covered by cluster emission detected by VTP outside the mentioned inner circle of 10-arcmin radius in each field is 1.7 deg^2, i.e. a negligible fraction of the total solid angle available for serendipitous detections.

However, not all of the 100 cluster detections in these 2134.6 deg^2 are necessarily serendipitous. 'Clusters cluster' to the extent that the odds of finding a second cluster within some 20 Mpc of any given cluster are significantly increased over the probability derived from their average volume density. As, by design, our serendipitous detections are all within 1°.3 of some target cluster (i.e. within 20 Mpc for $z < 0.2$), we need to account for the increase in the projected surface density of clusters caused by the non-vanishing amplitude of the cluster–cluster correlation function on these scales.

To this end we compare the relative separation in redshift space between the serendipitous clusters and the respective closest target clusters with the relative separation in z between random pairs of target clusters and serendipitously detected clusters that are separated by more than 20° on the sky. The latter set of pairs serves as a control sample which, owing to the large angular separation within each pair, can be assumed to be unaffected by clustering. As can be seen in Fig. 15, the fraction of serendipitous clusters that lie within
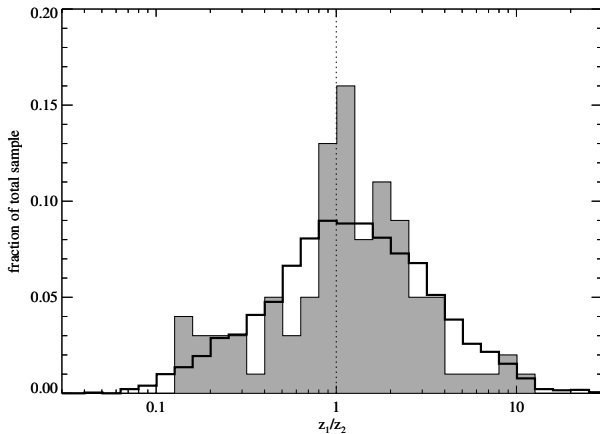
Figure 15. The distribution of the redshift ratios of the 100 serendipitous/target cluster pairs (shown shaded). The same distribution for a control sample of 5000 random pairs of target clusters separated by more than 20° on the sky is shown as the solid, bold line.

Figure 16. The cumulative flux distribution of the 442 clusters in our sample of VTP detections with raw count rates greater than 0.07 count s^{-1}. VTP re-detections of the initial target clusters selected from the SASS source list and additional, serendipitous VTP detections are plotted separately. The sample of SASS-based clusters also contains five physically associated systems. Note how, at a flux of about 5×10^{-12} erg cm^{-2} s^{-1}, the number count distribution of SASS-based clusters begins to flatten compared with a power law (shown as a dotted line).

some 20 per cent of the redshift of the nearest target cluster is somewhat higher than what would be expected from the same distribution for physically unrelated cluster pairs, indicating that clustering has indeed some effect.[12] Note that the fact that more than half of the serendipitously detected clusters have only estimated redshifts does not greatly affect this result: although random errors in the estimated redshifts (which are of the order of 20 per cent: see EVB) introduce a blurring of the distribution shown in Fig. 15, the effect is limited to a scale comparable to the bin width in Fig. 15. We can, in a statistical sense, quantify how many of our serendipitously detected clusters can be attributed to large-scale clustering by gradually removing from our sample quasi-serendipitous clusters that lie close to the peak of the distribution shown in Fig. 15 until the redshift ratio distribution of the remaining cluster pairs becomes consistent with that of our control sample. In any case we are dealing with a small correction as, according to the Kolmogorov–Smirnov statistic, the distribution of the original sample is inconsistent with that of the control sample at only the 56 per cent level. If only five serendipitous clusters that lie within 20 per cent of the redshift of the nearest target cluster are removed, the probability that the remaining distribution is not drawn from the same parent distribution as that of our control sample falls to below 50 per cent, and, if 10 of the serendipitous detections are attributed to clustering, the respective figure drops to less than 23 per cent.

In an attempt to find at least some of the few physical pairs, we compute the projected metric separations of those serendipitous/target cluster pairs with redshifts that agree to within 20 per cent. Five pairs feature separations of less than 2 Mpc if the mean of the respective cluster redshifts is assumed in the conversion from angular to metric separations. We assume that the affected serendipitously detected clusters are physically related to the respective target clusters, and thus move A2122, A2151b, A2197b, A2678 and IV Zw 038 from our list of serendipitous detections to that of our target clusters. Note that all of these five clusters have measured redshifts.

[12] The distribution shown in Fig. 15 is slightly skewed toward z_1/z_2-values greater than unity. This is due to a small, systematic difference in the redshift distributions of the two samples: since we processed the PET data around *all* Abell clusters within a redshift of 0.05, the odds of serendipitously detecting a background cluster are, on average, slightly higher than those of finding a cluster in the foreground.
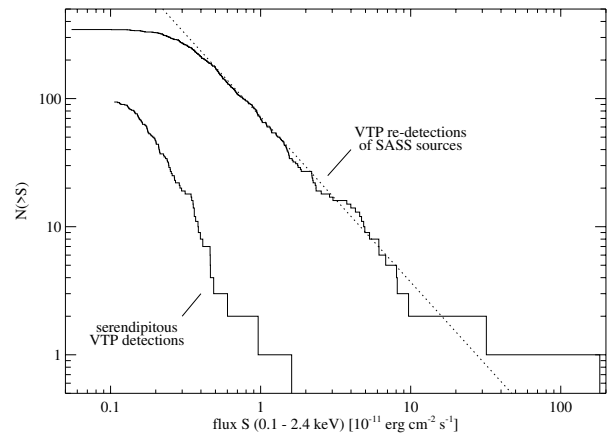
The set of the remaining 95 serendipitous VTP detections (of which no more than a handful may still be due to clustering) is of crucial importance for the assessment of the completeness of the BCS as a statistical sample. As mentioned before, VTP was run on only 15.7 per cent of our actual study area. Hence the BCS cluster list is incomplete, to some extent, at almost any X-ray flux level, and particularly so for low flux and low-surface-brightness emission from nearby poor clusters and groups of galaxies to which the SASS detection algorithms are particularly insensitive. This is illustrated in Fig. 16 which shows the cumulative number of clusters in our (so far) VTP count rate limited sample as a function of energy flux with the total sample split into two subsets. On the one hand, there are the 342 clusters detected by VTP within the inner 10 arcmin of the PET fields (which are, with few exceptions, re-detections of sources from our initial SASS source list which covered the whole northern extragalactic sky) plus five clusters detected at larger angular offsets from the respective target clusters but physically associated with them. On the other hand, we have the 95 clusters detected serendipitously by VTP in our 631 PET fields (i.e. outside the inner 10 arcmin – again with a few exceptions). Note how the sample based on SASS detections alone starts to become seriously incomplete at fluxes as high as $\sim 5 \times 10^{-12}$ erg cm^{-2} s^{-1}.

The level of incompleteness at any flux level can be quantified very accurately with the help of the serendipitous detections. The total solid angle of our study area defined by $\delta \geq 0°$, $|b| \geq 20°$ is 13 578 deg^2, or 4.14 sr. By weighting the serendipitous clusters by a factor given by the ratio of respective sky areas (i.e. 13 578/2134.6 = 6.36), we can thus correct for the incompleteness introduced by the fact that VTP was not run on the whole of our study area. This would be the correct weight only if our cleaned list of serendipitous detections were really entirely unaffected by clustering. If we assume that five more of our 95 non-target clusters are in fact not really serendipitous (without knowing which ones they are), the weight assigned to all our non-target clusters drops from

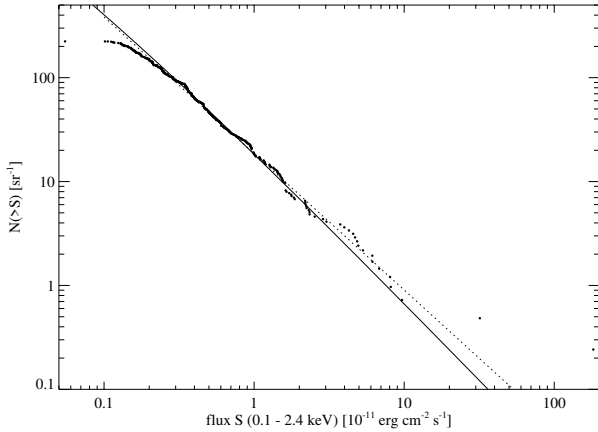$$w_0 = \frac{13\,578}{2134.6} = 6.36 \quad \text{to} \quad w = w_0 - \frac{5}{95}(w_0 - 1) = 6.08.$$

Figure 17. The cumulative $\log N - \log S$ distribution of the 442 clusters in our sample of VTP detections with raw count rates greater than 0.07 count s^{-1}. Serendipitous VTP detections are included with a relative weight of 6.08 which takes into account the smaller solid angle available for serendipitous detections. The solid curve shows the run of $N(> S)$ for a cluster population described by the BCS X-ray luminosity function (Ebeling et al. 1997) in a flat Einstein–de Sitter universe. The dotted line represents the best overall power-law description of the data and has a slope of -1.31.

Figure 18. The final cluster fluxes as a function of the detected VTP count rate for our sample of 442. Note how our count rate limit of 0.07 count s^{-1} ensures completeness to a flux limit of about 2×10^{-12} erg cm^{-2} s^{-1}.

For many statistical purposes (such as studies of the cluster $\log N - \log S$ distribution or the cluster X-ray luminosity function) the intrinsic incompleteness of the BCS can thus be entirely overcome by applying the above modified sky coverage correction. This is demonstrated in the following section.

7.2 The $\log N - \log S$ distribution of clusters of galaxies

As was shown in the previous section, the BCS cluster list starts to become seriously incomplete at fluxes around 5×10^{-12} erg cm^{-2} s^{-1}. However, when the serendipitous VTP detections are normalized properly, it becomes apparent that this incompleteness is not due to any intrinsic limitation of the RASS like, for instance, the relatively short exposure times, but is entirely due to the inadequacy of the SASS algorithms for the detection and characterization of extended emission.

7.2.1 The BCS $\log N - \log S$ distribution

Fig. 17 shows the BCS $\log N - \log S$ distribution when serendipitous VTP detections are included with a relative weight of 6.08 which allows for the smaller solid angle that is actually available for serendipitous detections (see Section 7.1 for details). We determine the best power-law description of the BCS $\log N - \log S$ in a maximum likelihood fit to the bright end of the differential, unbinned distribution. As the uncertainty of the best-fitting slope is dominated by systematics (namely the precise choice of the flux range over which the fit is performed) rather than by statistics, we investigate these systematics by performing a series of fits to the data in the range $S > S_{min}$, where S_{min} is varied from 2×10^{-12} to 2×10^{-11} erg cm^{-2} s^{-1}. Note that, in these fits, the amplitude κ of the fitted power law $N(> S) = \kappa S^{-\alpha}$ is completely determined by the best-fitting slope α and the requirement that the integral number of clusters be conserved. Thus α is the only independent fit parameter. For $S_{min} \approx 9 \times 10^{-12}$ erg cm^{-2} s^{-1} we find the BCS $\log N - \log S$ distribution to be well described by a Euclidean power law, i.e. $\alpha = 1.5$, indicative of a non-evolving source population in
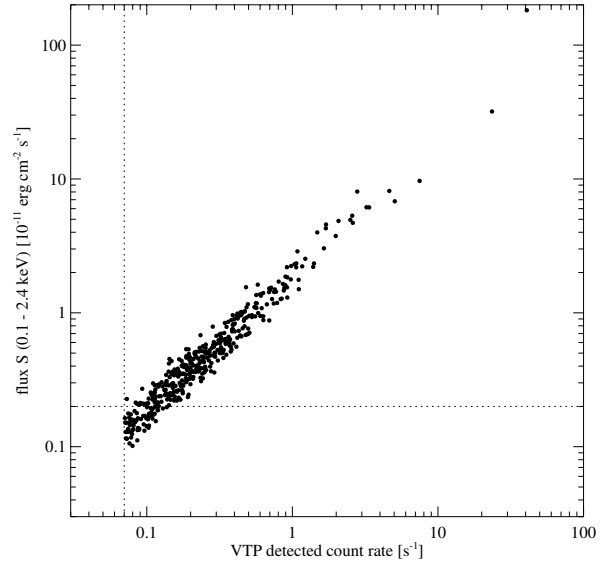
a static universe. For lower values of S_{min} the best-fitting α-value decreases slightly to reach $\alpha \approx 1.3$ at $S_{min} = 2.5 \times 10^{-12}$ erg cm^{-2} s^{-1}. This intrinsic flattening of the cluster $\log N - \log S$ distribution is, however, not necessarily a sign of cluster evolution but mainly an effect of the expansion of the universe. At redshifts below about 0.1, spatial volumes in the observer's reference frame can be considered identical to the intrinsic, comoving ones. However, at the redshifts probed by the BCS ($z \lesssim 0.4$), the difference becomes significant. If cosmological effects are taken into account, we find not just the bright end, but in fact the whole of the BCS $\log N - \log S$ distribution to be fully consistent with a non-evolving cluster space density. Fig. 17 illustrates this by showing the run of $N(> S)$ for a cluster population following the local cluster X-ray luminosity function (XLF) as described by Ebeling et al. (1997) and assuming an Einstein–de Sitter universe where $q_0 = 0.5$ and $H_0 = 50$ km s^{-1} Mpc^{-1} (solid line). Although the good agreement is not entirely surprising in view of the fact that both the $\log N - \log S$ distribution and the cluster XLF were determined from the same sample (the BCS), the comparison still represents a useful consistency check. Note also that the excellent agreement holds down to fluxes of about 2.5×10^{-12} erg cm^{-2} s^{-1}, i.e. almost a factor of 2 below the flux limit of the BCS subsample used by Ebeling et al. (1997) in the construction of the cluster XLF.

In order to facilitate comparison with previous work and also to provide a simple analytic parametrization of the BCS $\log N - \log S$ distribution over a large range of fluxes, we determine a global power-law description from the values obtained for κ and α when S_{min} is varied from 4×10^{-12} to 8×10^{-12} erg cm^{-2} s^{-1}. The median values κ, α of the best-fitting power laws found in this range are

$$\kappa = 18.63^{-0.08}_{+0.09} \text{ sr}^{-1} (10^{-11} \text{ erg cm}^{-2} \text{ s}^{-1})^{\alpha}, \quad \alpha = 1.31^{+0.06}_{-0.03}, \quad (5)$$

where the quoted errors represent not 1σ uncertainties but rather the 10th and 90th percentiles of the distribution of best-fitting parameters.

We emphasize once more that the fact that the Euclidean α-value of 1.5 is excluded at more than 90 per cent confidence by the quoted uncertainties does *not* imply an evolving cluster population.

It is also noteworthy that, at a flux of 2×10^{-12} erg cm^{-2} s^{-1}, the data still fall within 4 per cent of the power-law value of equation (5) and within 9 per cent of the prediction of our Einstein–de Sitter model, indicating that, in principle, the RASS data in the northern hemisphere would allow the compilation of complete, flux-limited cluster samples down to, and possibly even below, this value. At even lower fluxes the BCS $\log N - \log S$ distribution begins to flatten beyond the theoretical expectation. This is, however, probably mainly due to our count rate limit at 0.07 count s^{-1}, as can be seen from Fig. 18 which shows the final cluster fluxes as a function of the initially detected (i.e. uncorrected) VTP count rate. At higher count rates (fluxes) VTP detects more than 50 per cent of the cluster emission directly regardless of the extent of the emission (cf. Fig. 11), i.e. the detection efficiency is indeed essentially 100 per cent.

Thanks to the, by X-ray standards, huge size of our sample (442 clusters) and the homogeneous selection criteria used in its compilation, the power law with κ and α as quoted in equation (5) represents the best parametrization of the cluster $\log N - \log S$ distribution at fluxes above 2×10^{-12} erg cm^{-2} s^{-1} to date.

7.2.2 Comparison with previous determinations of the cluster log N–log S distribution

To allow a comparison of our results with previous and future work in other energy bands, we also compute the BCS $\log N - \log S$ distribution in the following energy ranges: 0.5–2.0 keV (*ROSAT* hard band), 0.3–3.5 keV (*EMSS*), 2–10 keV (*HEAO-1*), and 0.01–100 keV (pseudo-bolometric).

Fig. 19 shows the respective distributions in three of these bands and illustrates the excellent agreement between our results and earlier measurements. In the 2–10 keV band (Fig. 19, top panel), at very high fluxes ($S > 3.6 \times 10^{-11}$ erg cm^{-2} s^{-1}), our data confirm the early measurement of Piccinotti et al. (1982) which was based on 25 clusters detected by the *HEAO-1 A-2* experiment. At somewhat lower fluxes, the BCS $\log N - \log S$ distribution is also (just) in agreement with the result of Edge et al. (1990) obtained for a sample of 46 clusters compiled from *HEAO-1*, *Ariel V*, *Einstein* and *EXOSAT* data.

In the 0.5–2.0 keV range (Fig. 19, middle panel), at fluxes down to 3×10^{-12} erg cm^{-2} s^{-1}, the BCS $\log N - \log S$ distribution is, within the errors, in agreement with early results from the ESO Key Programme[13] (Guzzo et al. 1995) for a sample of 111 clusters in the southern hemisphere (De Grandi 1996). That the best-fitting power law found by De Grandi is somewhat shallower than that of the BCS in the same flux range ($\alpha = 1.21$ as opposed to 1.28 for the BCS) is mainly due to the fact that De Grandi's fit does not explore a range of minimal fluxes, which causes her best power-law representation to be dominated by the apparent flattening of the $\log N - \log S$ distribution at the low-flux end of her sample. However, her 1σ lower limit ($\alpha = 1.36$, $\kappa = 9.21$) is in very good agreement with both the BCS and the Piccinotti et al. result.

The bottom panel of Fig. 19, finally, shows the BCS $\log N - \log S$ distribution in the 0.3–3.5 keV band of the *Einstein* observatory. To establish the EMSS cluster $\log N - \log S$ distribution, we consider the updated EMSS cluster sample of Gioia & Luppino (1994) with the restrictions described by Henry et al. (1992), i.e. $\delta \geq -40°$ and $f_{det} \geq 1.33 \times 10^{-13}$ erg cm^{-2} s^{-1} (0.3–3.5 keV). The latest EMSS source identifications as listed by Maccacaro et al. (1994) are taken into account, as well as new redshifts from Luppino & Gioia (1995)

---

[13] Recently renamed the REFLEX Cluster Survey.
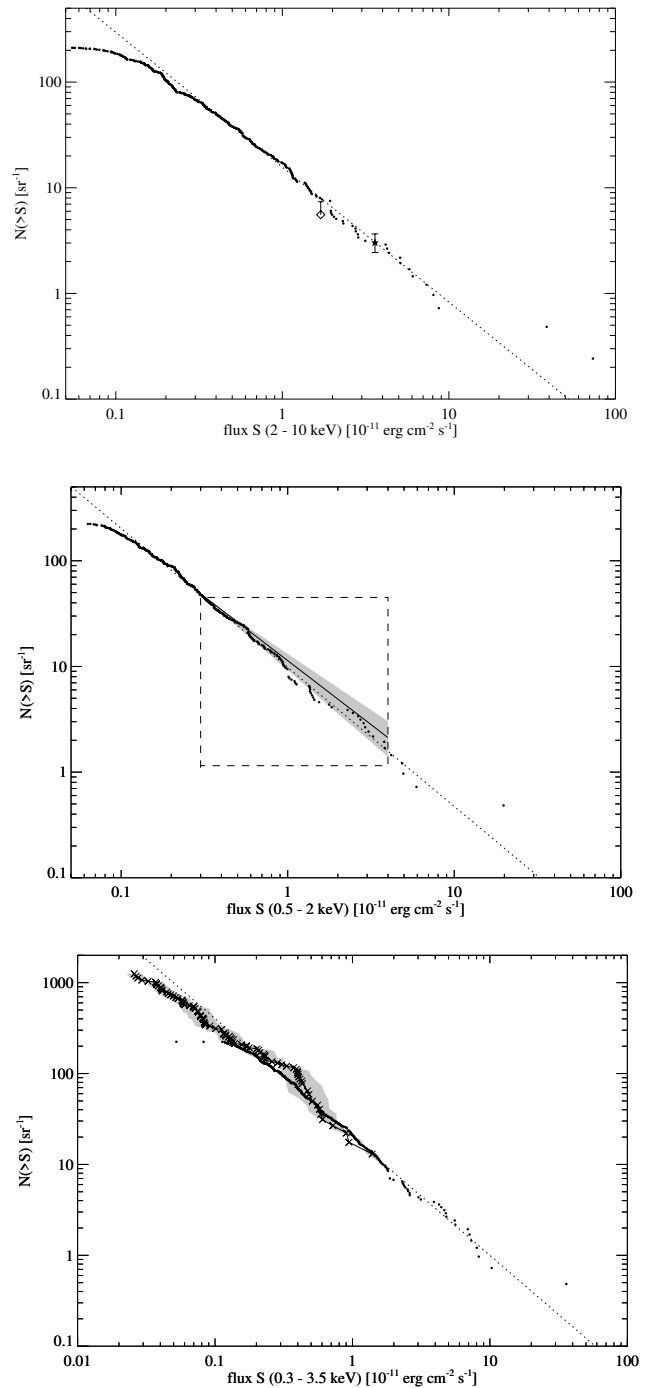
Figure 19. The cumulative $\log N - \log S$ distribution of the 442 clusters in our sample in the 2–10 keV (top), the 0.5–2.0 keV (centre) and the 0.3–3.5 keV bands (bottom). The single data point shown as a filled star in the top panel denotes the space density of *HEAO-1* clusters as determined by Piccinotti et al. (1982); the open diamond represents the result of Edge et al. (1990) with its 90 per cent upper limit. In the central panel, the solid line inside the shaded triangle represents the best power-law fit with its 1σ error range for the $\log N - \log S$ distribution of De Grandi (1996) for an early cluster subsample from the ESO Key Programme (now known as the REFLEX Cluster Survey). The actual flux range covered by the REFLEX subsample is indicated by the dashed box. In the bottom panel, the crosses connected by a solid line represent the $\log N - \log S$ distribution of the EMSS cluster sample of Henry et al. (1992). The shaded region illustrates the effect of varying the assumed cluster core radius from 200 to 300 kpc. At its bright end, the EMSS $\log N - \log S$ distribution was forced to agree with the BCS power law.

and Romer (private communication). Also, we discard MS 0011.7 + 0837, 1050.7 + 4946, 1154.1 + 4255, 1209.0 + 3917 and 1610.4 + 6616, all of which have revised non-cluster identifications based on additional optical and X-ray observations (Gioia, Stocke & Henry, private communication). The $\log N - \log S$ distribution for the resulting sample of 87 EMSS clusters is then computed from the total cluster fluxes and the sky coverage values corresponding to the detected fluxes as published by Henry et al. (1992). Consisting exclusively of serendipitous detections, the EMSS sample is potentially intrinsically incomplete at its high-flux end, as the corresponding X-ray-bright clusters were preferentially selected as targets of *Einstein* observations, thereby making them unavailable for serendipitous detection. We compensate for this effect by forcing the EMSS $\log N - \log S$ distribution to match the BCS power-law value at the flux of the brightest EMSS cluster. We stress that this is only a minor adjustment, as no more than one additional cluster is required at $S \gtrsim 1.4 \times 10^{-11}$ erg cm^{-2} s^{-1} to make the bright end of the EMSS $\log N - \log S$ distribution match the BCS power-law value.

In addition to the usual statistical error, the EMSS $\log N - \log S$ function is affected by systematic errors introduced by the fact that Henry and co-workers used a fixed value of 250 kpc for the cluster core radius in their conversion from detected to total fluxes. The impact of this effect can be assessed by recomputing the total EMSS cluster fluxes for slightly different core radii (we assume 200 and 300 kpc, respectively). The shaded region in the bottom plot of Fig. 19 illustrates the resulting uncertainty in the EMSS $\log N - \log S$ distribution. Within these errors, the EMSS data are fully consistent with the BCS $\log N - \log S$ distribution where the flux ranges of the two samples overlap and the BCS is not affected by the applied count rate cut (i.e. $S \gtrsim 2 \times 10^{-12}$ erg cm^{-2} s^{-1}). At fluxes around 1×10^{-12} erg cm^{-2} s^{-1}, however, the EMSS $\log N - \log S$ distribution begins to deviate significantly from the extrapolated BCS power law, possibly indicating that cluster evolution becomes increasingly important at the higher redshifts probed by the EMSS ($z_{max} = 0.82$). The evidence for cluster evolution in the BCS is discussed in the context of the BCS X-ray luminosity function (Ebeling et al., 1997); a reassessment of the significance of the evolution in the EMSS sample is discussed by Nichol et al. (1997).

Since the only parametrization of the EMSS cluster $\log N - \log S$ distribution in the literature (Gioia et al. 1984) is based on an erroneous sky coverage calculation which did not treat extended emission properly, we quote the best-fitting power-law parameters for the EMSS cluster sample for reference:

$$\kappa = 23.9^{-4.3}_{+2.7} \text{ sr}^{-1}(10^{-11} \text{ erg cm}^{-2} \text{ s}^{-1})^{\alpha}, \quad \alpha = 1.13^{+0.11}_{-0.05}. \quad (6)$$

The quoted errors correspond to the 10th and 90th percentiles of the

best-fitting values found when the fit range is varied from $S_{min} = 4 \times 10^{-13}$ to 8×10^{-13} erg cm^{-2} s^{-1}. A core radius of 250 kpc was assumed in the conversion from detected to total fluxes. Varying this parameter in the range from 200 to 300 kpc affects mainly the amplitude of the resulting best-fitting power law, but hardly changes the slope. The best-fitting parameters of equation (6) change only marginally if we fit to the EMSS data without enforcing a match with the BCS power law at the bright end. We obtain

$$\kappa = 20.7^{-4.2}_{+2.9} \text{ sr}^{-1}(10^{-11} \text{ erg cm}^{-2} \text{ s}^{-1})^{\alpha}, \quad \alpha = 1.18^{+0.12}_{-0.06},$$

consistent with our previous result.

A power-law representation of the EMSS cluster $\log N - \log S$ distribution has also been computed by Rosati et al. (1995) by integrating the X-ray luminosity functions of Henry et al. (1992). However, Rosati and co-workers do not quote the result of this exercise in their paper, and their fig. 5 shows the EMSS power law not in the *Einstein* passband but rather in the *ROSAT* 0.5–2.0 keV range. Thus we can only state that the above parametrization is in qualitative agreement with their figure.

We emphasize once more that the discrepancy between the BCS and EMSS power-law slopes does not imply a conflict between the two samples, in particular since the actual *data* agree at fluxes greater than 2×10^{-12} erg cm^{-2} s^{-1} (0.3–3.5 keV). Given the impressive redshift range spanned by the EMSS cluster sample ($0.046 \leq z \leq 0.826$), its $\log N - \log S$ distribution cannot be expected to follow a single power law. Indeed, a trend for the EMSS $\log N - \log S$ distribution to flatten with decreasing flux is evident in Fig. 19.

Table 2 summarizes the fit results for the BCS $\log N - \log S$ distributions in all five energy bands.

7.3 The flux-limited *ROSAT* Brightest Cluster Sample

As discussed in detail in Section 7.1, the BCS cluster list starts to become increasingly incomplete at fluxes of about 5×10^{-12} erg cm^{-2} s^{-1}, because serendipitous VTP detections that could compensate for the incompleteness of the sample based on SASS detections alone are available for only about one-sixth of the total BCS sky area. Although this incompleteness can be corrected for and is thus of no major concern for the study of certain cluster statistics such as the $\log N - \log S$ distribution (see Section 7.2.1) or the X-ray luminosity function, it represents a severe handicap for other investigations, most notably the spatial cluster–cluster correlation function, where such corrections cannot be applied and a reasonably complete statistical sample is required.

Fig. 20 shows again the cumulative number counts of all 442 BCS clusters as a function of flux. However, this time all clusters are given the same weight of unity, i.e. no corrections are made for

Table 2. The results of maximum likelihood fits of a power law $N(> S) = \kappa S^{-\alpha}$ to the BCS $\log N -$ $\log S$ distributions in five different energy bands. The quoted best-fitting parameters are the median values of the results obtained in fits to the data at $S > S_{min}$, where S_{min} is varied as indicated. The quoted errors are the 10th and 90th percentiles, respectively.

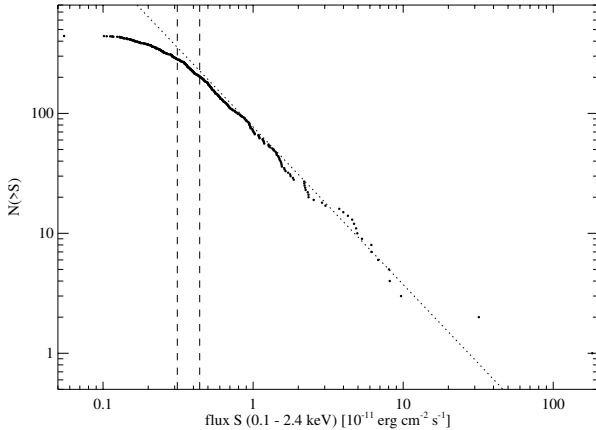| energy range (keV)	S_{min} range $(10^{-11} \text{ erg cm}^{-2} \text{ s}^{-1})$	κ [sr^{-1} $(10^{-11} \text{ erg cm}^{-2} \text{ s}^{-1})^{\alpha}$]	α
0.1–2.4	0.40–0.80	$18.63^{-0.08}_{+0.09}$	$1.31^{+0.06}_{-0.03}$
2.0–10.0	0.35–0.70	$15.67^{-0.10}_{+0.11}$	$1.28^{+0.05}_{-0.03}$
0.5–2.0	0.25–0.50	$9.80^{-0.25}_{+0.09}$	$1.32^{+0.05}_{-0.04}$
0.3–3.5	0.42–0.84	$20.05^{-0.24}_{+0.27}$	$1.30^{+0.05}_{-0.04}$
bolometric	0.80–1.60	$47.0^{-1.6}_{+3.5}$	$1.27^{+0.08}_{-0.05}$

Figure 20. The cumulative flux distribution of all 442 clusters in our sample of VTP detections with raw count rates greater than 0.07 count s^{-1}. The dotted line represents the power-law description of the BCS $\log N$–$\log S$ distribution as determined in Section 7.2.1. The dashed lines mark the flux limits of 80 and 90 per cent completeness, respectively.
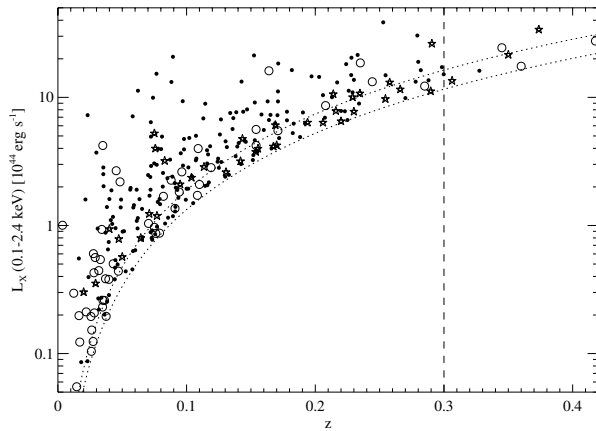

Figure 21. The X-ray luminosity of the 283 clusters of the 80 per cent complete flux-limited BCS as a function of redshift. The dotted lines show the cut-off introduced by the X-ray flux limits at 3.1×10^{-12} erg cm^{-2} s^{-1} (80 per cent completeness) and 4.4×10^{-12} erg cm^{-2} s^{-1} (90 per cent completeness). Abell (Zwicky) clusters are plotted as solid dots (stars); the remaining 52 clusters not contained in these largest optical cluster catalogues are shown as open circles.

variations in the effective sky coverage within our sample. The overlaid power law represents the best fit to the BCS $\log N$–$\log S$ distribution as determined in Section 7.2.1. The requirement that the flux completeness be at least 80 per cent leads to a limiting flux of 3.1×10^{-12} erg cm^{-2} s^{-1} and yields a subsample of 283 clusters. Included in this flux-limited, 80 per cent complete BCS is a smaller, 90 per cent flux complete sample of 203 clusters with fluxes higher than 4.4×10^{-12} erg cm^{-2} s^{-1}. Limiting the BCS to this more complete subsample will allow us to quantify how incompleteness affects the BCS cluster–cluster correlation function (Edge et al., in preparation).

8   THE SPATIAL DISTRIBUTION OF BCS CLUSTERS

In this section we discuss the redshift and Galactic latitude distribution of the clusters in the flux-limited BCS and present distribution of the BCS clusters on the sky.
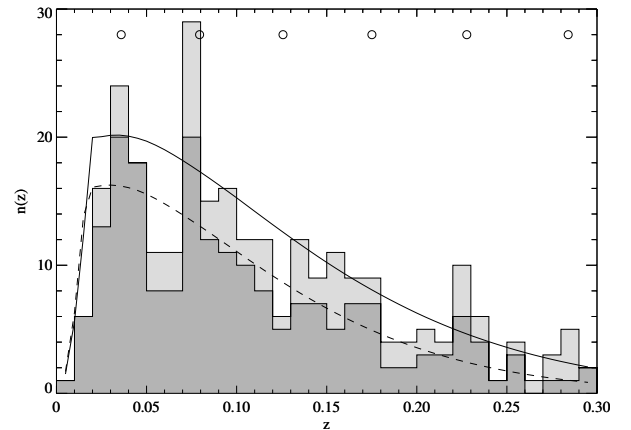
Figure 22. The differential redshift distributions of the clusters in the flux-limited BCS. The distribution shown in light shading represents the 80 per cent complete sample; the 90 per cent complete subsample is shown in dark shading. The open circles in the upper half of the plot mark the loci of spherical shells in comoving space at a constant separation of $120 \, h_0^{-1}$ Mpc. The solid and dashed curves show the redshift distribution expected for a spatially homogeneous cluster distribution.

8.1   The redshift distribution of the BCS

Fig. 21 shows the X-ray luminosity of the BCS clusters as a function of redshift. (The two components of the double cluster A1758 have been merged for this plot.[14]) Of the initial 95 serendipitous VTP-detected clusters (see Section 7.1), 19 are sufficiently X-ray-bright to be included in the 80 per cent complete BCS, and for seven the X-ray flux exceeds also the flux limit of the 90 per cent complete BCS.

We note that although 68 (70) per cent of the clusters in the 80 (90) per cent complete BCS subsamples are Abell clusters, the fraction of non-Abell clusters in the BCS is substantial: 13 (11) per cent of the systems contained in the 80 (90) per cent complete sample are Zwicky clusters without Abell identification, and another 18 (19) per cent are listed in neither of the two largest optical cluster catalogues used in our study.

Redshifts have been measured for 98 per cent of the clusters in the 80 per cent complete sample; for the 90 per cent complete sample the redshift completeness rises to 100 per cent. However, a number of BCS clusters are (by RASS standards) very distant ($z \gtrsim 0.35$), and fall thus into a regime where a reliable optical confirmation is no longer feasible from the POSS images alone. Since the POSS plates were our main source of optical information in the cluster verification and confirmation stage of the compilation of the BCS (cf. Section 5), this introduces a redshift limit to the statistically useful BCS at $z \sim 0.3$ (see the dashed line in Fig. 21). Within $z = 0.3$, 98 (100) per cent of the 80 (90) per cent complete BCS have measured redshifts. The sizes of these, our final statistical BCS subsamples within $z = 0.3$, are 276 and 201 clusters for 80 and 90 per cent flux completeness, respectively.[15]

Fig. 22 shows the redshift distributions of the 80 and 90 per cent complete BCS. Note the two pronounced peaks at redshifts around

---

[14] The only other double cluster remaining in the flux-limited sample is A2572a(=HCG 94)/A2572b. This system is at a redshift of 0.04 and, contrary to A1758 ($z = 0.28$), well resolved into two sources at the angular resolution of the RASS.

[15] Subclusters are counted separately: A2572a/b account for two clusters in either sample.

Figure 23. The sky distribution of the BCS clusters of the 80 per cent complete sample that fall into the $0.03 \leq z < 0.05$ (left) and $0.07 \leq z < 0.09$ (right) redshift intervals. Clusters belonging to known Abell superclusters are plotted encircled. In the case of the Hercules supercluster (PHG 9), we assume membership also for AWM 4 and MKW 3s. An equal-area Aitoff projection is used. The 40°-wide exclusion zone around the Galactic equator is marked by the dashed lines.

0.035 and 0.08. These are in part due to a series of superclusters, as can be seen from Fig. 23 which shows the sky positions of the clusters at the redshifts of these two peaks in equatorial coordinates. No fewer than four superclusters from the catalogue of Postman, Huchra & Geller (1992) contribute to the first of the peaks in Fig. 22. The Hercules supercluster, PHG9, contributes six Abell clusters to the BCS in the redshift range $0.03 \leq z < 0.05$ (A2052, A2063, A2107, A2147, A2148 and A2151); the non-Abell clusters AWM 4 and MKW 3s are probably also associated with this supercluster. Another five BCS clusters in the same redshift range (A2572a/b, A2589, A2593 and A2657) are part of the central region (PHG 22) of the Perseus–Pegasus filament. Finally, PHG 4 and PHG 16 are represented by the systems A1177 and A1185, and A147, A160, A168 and A193, respectively. Around the redshift of the second peak in Fig. 22, i.e. at $0.07 \leq z < 0.09$, it is mainly the Corona Borealis supercluster (PHG 7 and PHG 10) that contributes (A1775 and A1800, and A2061, A2065 and A2067, respectively). Additional signal comes from less prominent superclusters like SC 30/2 (Zucca et al. 1993), two members of which members (namely A2029 and A2033) are in this redshift slice of the BCS, as well as cluster pairs such as A399/A401 and A272/A278.

It is clear from Fig. 23 that neither of the pronounced two first peaks in Fig. 22 can be attributed to any single supercluster, although the Hercules supercluster accounts for about half of the excess signal around $z = 0.04$. Rather, it is clusters and superclusters from all over the sky that create the observed signature.

Motivated by this result, we investigate whether there is evidence for further peaks in the BCS redshift distribution. The spacing of the peaks at $z \sim 0.04$ and 0.08 corresponds to a separation in comoving distances of about 120 h_0^{-1} Mpc, a value very close to the apparent periodicity of 128 h_0^{-1} Mpc found in the galaxy 'pencil beam' surveys of Broadhurst et al. (1990).

If we assume that this is a typical separation intrinsic to large-scale clustering, we expect further peaks in the BCS redshift distribution at the locations indicated by the open circles at the top of Fig. 22. Although neither of these more distant peaks is

observed with a significance comparable to that of the first two,[16] the overall appearance of the BCS redshift distribution still lends mild support to the hypothesis of some regularity out to higher redshifts. We stress that this is the first time that evidence for a semi-regular redshift pattern has been found in a large-scale X-ray-selected cluster sample. As the BCS covers the whole extragalactic region of the northern hemisphere (i.e. a solid angle of more than 13 000 deg^2) and extends out to redshifts of $z = 0.3$, any such regularity can certainly not be attributed to unfortunate sampling as was argued in the case of the galaxy pencil beam surveys (van de Weygaert 1991). Our findings are in qualitative agreement with the explanation of Bahcall (1991) that a whole series of superclusters contributes to the periodicity found in galaxy pencil beam surveys, but are in conflict with her prediction that the apparent periodicity should be washed out when averaged over a large solid angle. Apparently the tails of superclusters are interconnected over even larger scales than was previously thought. Our finding thus lends support to the concept of a characteristic scale of ~ 115 Mpc in the large-scale distribution of matter advocated by, e.g., Einasto et al. (1997) based on optically selected cluster samples.

A more detailed discussion of the large-scale structure traced by the BCS will be presented in a forthcoming paper.

8.2 The Galactic latitude distribution of the BCS

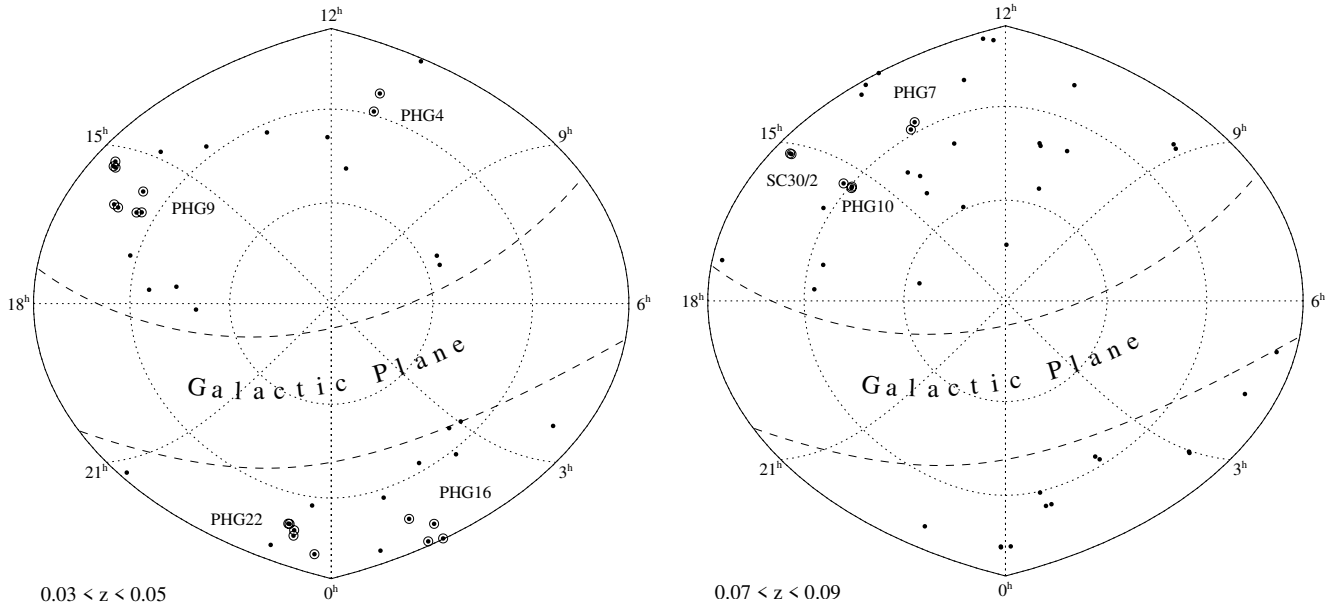Fig. 24 shows the distribution of the BCS clusters with Galactic latitude b for the 80 and 90 per cent complete samples and $z \leq 0.3$. Note that, for both samples, the number of BCS clusters as a function of b is in agreement with that expected for a uniform distribution of clusters on the sky (shown as the solid lines in Fig. 24). There is a slight deficiency in BCS clusters just north of the Galactic plane; for the 90 per cent complete BCS the dearth of

---

[16] Note that the apparent peak at $z \sim 0.225$ in Fig. 22 (lightly shaded histogram) contains one cluster with an estimated (rather than measured) redshift of $z \approx 0.23$. Estimated redshifts do not, however, contribute to any of the other peaks.

clusters in this region is significant at the 2.1σ level. The excess of clusters at Galactic latitudes of about 60° is, again, only marginally significant ($< 2.1\sigma$) for either sample. It is not caused by any known supercluster as, of the PHG superclusters (Postman et al. 1992), only PHG 4 contributes two clusters to the BCS at $60° \leq b < 70°$.

8.3   The distribution of the BCS clusters in the sky

Fig. 25 shows the equatorial sky distribution of the clusters in the two flux-limited BCS subsamples. Again, a redshift cut-off at $z = 0.3$ has been applied.

9   DIFFERENCES BETWEEN THE ABELL CONTENT OF THE BCS AND THE XBACs

Although the XBACs sample and the BCS have been compiled from the same RASS data, the Abell subsample of the flux-limited BCS
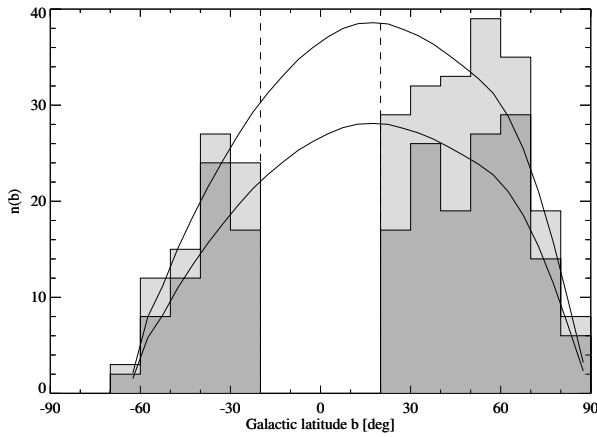
Figure 24. The differential Galactic latitude distribution of the 276 (201) BCS clusters within $z = 0.3$ in the 80 (90) per cent complete samples (light- and dark-shaded histograms, respectively). The solid lines indicate the run expected for either sample for a uniform distribution of clusters on the sky.
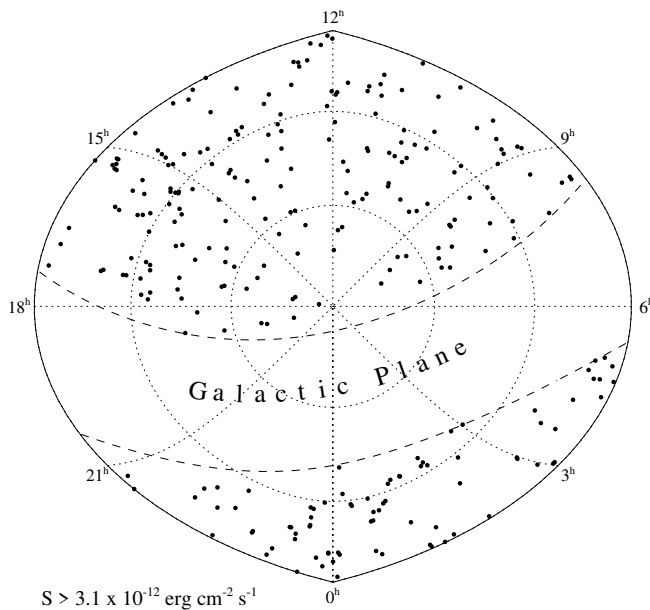
does not exactly match the XBACs list where both samples overlap in sky area and X-ray flux. The small, existing differences are due to different classifications for a few clusters and small variations in the final fluxes caused by, first, the use of more accurate flux correction factors in the BCS (Section 4), as well as, secondly, somewhat different criteria concerning the application of these correction factors for point-like and extended sources (see Section 4 of this paper and section 6.1 in EVB).

In detail the differences are as follows. The XBACs sample contains three clusters missing from the subsample of the BCS obtained by applying the XBACs flux limit of 5.0×10^{-12} erg cm^{-2} s^{-1}, namely A1035, A2228 and A2637. A1035 is listed as a cluster in both samples but its BCS flux is considerably lower than the XBACs value owing to the fact that a nearby soft X-ray source that was considered part of the cluster emission during the compilation of the XBACs sample was, upon careful re-assessment of the optical and X-ray evidence, discarded as unrelated in the course of the BCS compilation. A2228 is treated as a cluster with severe AGN contamination in the XBACs list, whereas it was discarded from the BCS as being dominated by AGN contribution. A2637 (Ledlow & Owen 1996) is a similar case: the system was included in the XBACs sample and marked as contaminated by emission from a background AGN, whereas the same cluster is missing from the BCS as the X-ray emission is now classified as being dominated by the same AGN.

For 10 Abell clusters the opposite scenario is realized: they are contained in the BCS and listed as featuring fluxes of, or greater than, 5.0×10^{-12} erg cm^{-2} s^{-1}, but are none the less missing from the XBACs sample. For two of these there has been a change of emphasis in the opposite sense to that mentioned above: the BCS lists them as *contaminated* by AGN emission, while they were discarded from the XBACs sample as likely to be *dominated* by AGN emission.

The fact that only three Abell clusters are contained in the XBACs sample but not in the corresponding subset of the BCS, while the opposite is true for 10 clusters, is due to the above-mentioned small changes in the final fluxes: the median ratio of the BCS and XBACs fluxes for clusters contained in both samples is
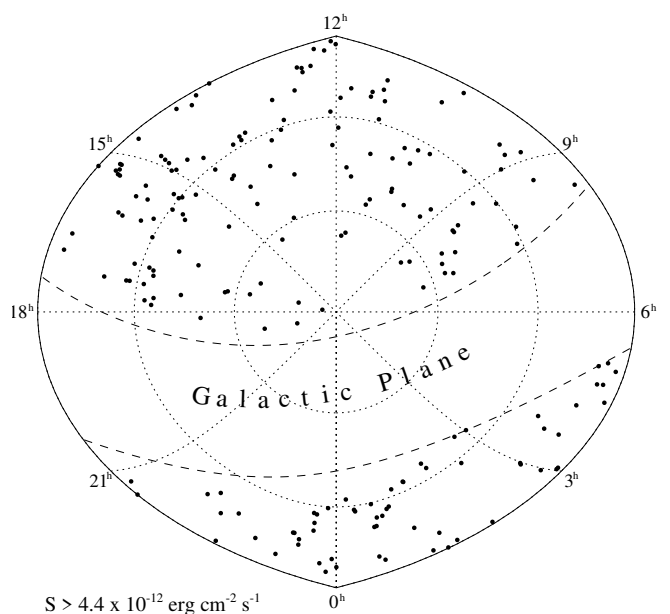
Figure 25. The distribution of the BCS clusters in the 80 and 90 per cent samples (left and right panels, respectively) in an equal-area Aitoff projection of the northern hemisphere. The 40°-wide exclusion zone around the Galactic equator is marked by the dashed lines.

1.015, i.e. there is a tendency for the more accurate BCS fluxes to be slightly higher than the XBACs fluxes computed earlier. This causes eight Abell clusters just to make the XBACs flux limit of 5.0×10^{-12} erg cm^{-2} s^{-1} when the BCS fluxes are used, while they remain just below the flux limit in the original XBACs list.

For all practical purposes, the sample of Abell clusters with fluxes higher than 5×10^{-12} erg cm^{-2} s^{-2} in the BCS can thus be considered to be the same as the subset of the XBACs sample defined by $|b| \geq 20°$ and $\delta \geq 0°$.

10 THE RELEVANCE OF THE 1RXS CATALOGUE FOR THE BCS

While this paper was being prepared for submission, MPE released the *ROSAT* All-Sky Survey Bright Source Catalogue (1RXS: Voges et al. 1996), a list of more than 18 000 sources down to count rates of 0.05 count s^{-1} detected by the SASS in its second processing of the RASS data. The main difference between the first SASS processing (SASS-I) from which the compilation of the BCS started (see Section 2) and this second processing (SASS-II) is that the analysis is no longer confined to 2°-wide strips but is performed on merged photon maps of the same type as those used by VTP in our reprocessing of the RASS data. Note, however, that while the raw data used by the SASS have thus changed, the SASS detection algorithms have not. Accordingly, the severe underestimation of the flux from extended emission discussed by EVB persists, and a reprocessing of the raw data (by VTP or another suitable algorithm) remains mandatory for the compilation of an X-ray flux-limited cluster sample.

Besides the differences in the underlying raw data, the source lists from the first SASS processing and the 1RXS catalogue differ also in the applied source likelihood threshold. Whereas the SASS-I master source list contains all detections with a likelihood of existence higher than 10, a more conservative threshold value of 15 was used in the compilation of the 1RXS catalogue.[17] Probably as a result of this higher threshold, the 1RXS catalogue lists only 8541 sources with count rates higher than 0.1 count s^{-1}, as compared with 10 241 found in the first SASS processing (see Section 3.1).

Given that the number of 1RXS sources above our initial count rate cut is smaller than in SASS-I, we do not necessarily expect a 1RXS-based cluster sample to be more complete than the BCS as it stands. To test this explicitly, we have repeated the first steps of the BCS compilation procedure using the 1RXS catalogue (limited to our study area and sources brighter than 0.1 count s^{-1}) as the input X-ray source list. We find the number of true coincidences in the cross-correlations with the Abell cluster catalogue to lie 10 per cent below the figure obtained for the source list from the first SASS processing, while the number of true coincidences with Zwicky clusters is essentially the same as for the SASS-I source list (see Section 3.1). The number of significantly extended sources in the 1RXS catalogue (318 at $\delta \geq 0°$, $|b| \geq 20°$ and with count rates greater than 0.1 count s^{-1}) is significantly lower than that obtained in the first SASS processing (406 within the same constraints).

A cluster sample compiled from the 1RXS catalogue following the BCS procedure would thus probably be smaller, i.e. less complete, than the BCS as presented here. If we consider only those clusters in the final 90 per cent flux complete BCS subsample

that have SASS-I count rates higher than 0.1 count s^{-1} (i.e. excluding serendipitous VTP detections), we find that 10 of the 196 SASS-I-detected BCS clusters are not contained in the 1RXS catalogue *at any count rate limit*. Among these 10 is Virgo, the X-ray-brightest cluster in the sky, as well as three other clusters with VTP fluxes in excess of 1×10^{-11} erg cm^{-2} s^{-1} (A2589, A2593 and A76). If we apply the same count rate cut to the 1RXS catalogue as before to the SASS-I source list (0.1 count s^{-1}), the number of BCS clusters missing from the 1RXS list becomes even higher: no fewer than 23 of the 201 X-ray-brightest clusters in the northern hemisphere would be missing had we used the 1RXS catalogue instead of the SASS-I source list.[18] For the seven clusters in the 90 per cent complete BCS that were serendipitously detected by VTP, the situation is even worse: two have been missed altogether by SASS-II, another one is listed with a count rate below our threshold of 0.1 count s^{-1}, and a fourth one, RX J1206.6+2811 (MKW 4s), lies above the count rate limit but is classified as a point source and thus would also not have made it into the BCS.

As detailed above, more than 10 per cent of the clusters in the 90 per cent complete BCS would be missing had we based our compilation on the SASS-II detections listed in the 1RXS catalogue rather than on the SASS-I master source list. Although we cannot rigorously prove that the fact that SASS-II fails to reproduce the 90 per cent complete BCS is a reliable measure of the overall performance of the second processing, we are confident that the number of clusters that have been detected by SASS-II outside the area reprocessed by VTP, and which may turn out to be bright enough to be included in the BCS when reprocessed by VTP, cannot outweigh this incompleteness.

11 BCS – THE SAMPLE

Table 3 lists the 201 X-ray-brightest clusters with Galactic latitudes $|b| \geq 20°$, within a redshift of 0.3, and with 0.1–2.4 keV fluxes greater than 4.4×10^{-12} erg cm^{-2} s^{-1}. This sample is 90 per cent flux complete. We also include two clusters at redshifts greater than 0.3 (marked with a filled star symbol in the first column) that otherwise meet the selection criteria. For the sake of completeness we also list A2151b, an apparent low-luminosity satellite of A2151a, although its flux falls almost a factor of 3 short of the quoted limit, as well as A1758a/b which are detected as separate subclusters below the flux limit but are bright enough to make the flux cut when combined. Of these 201 clusters, 71 per cent are Abell clusters, 10 per cent are Zwicky clusters, and 19 per cent are systems not contained in either of these two largest optical cluster catalogues. The diversity of our final sample underlines yet again the importance of X-ray-selected samples for unbiased statistical studies of cluster properties.

The sample listed explicitly in Table 3 is limited to a size of ~200 clusters in order to keep it smaller than a cluster sample under compilation in a second follow-up project of northern RASS clusters (Böhringer et al., in preparation; Burg et al., in preparation). An extended BCS listing including clusters down to a flux limit of ~3×10^{-12} erg cm^{-2} s^{-1} will be published later.

In detail the contents of Table 3 are as follows.

column 1: redshift, contamination, extent and serendipity flag. Clusters at $z > 0.3$ are marked with a filled star; 'c' means that a significant fraction of the quoted flux may come from embedded

---

[17] The version released by MPE on 1996 June 19 also contains 58 sources with count rates and existence likelihoods of zero. In the latest release (1.2), this number has dropped to 9.

[18] We consider a BCS cluster as missing from the 1RXS catalogue if the latter contains no entry within 10 arcmin (radius) of the VTP cluster position.

Table 3. The *ROSAT* Brightest Cluster Sample.

z, contam. extent, serend. flag	cluster name	α (J2000) [deg]	δ (J2000) [deg]	n_H [10^{20} cm^{-2}]	RASS exp. time [s]	VTP count rate [s^{-1}]	r_{VTP} [arcmin]	final count rate [s^{-1}]	count rate error [s^{-1}]	kT [keV]	z	f_X (0.1–2.4 keV) [10^{-12} erg cm^{-2} s^{-1}]	L_X (0.1–2.4 keV) [10^{44} erg s^{-1}]	z reference
VS	RXJ0000.1+0816	0.044	8.277	5.3	436	0.24	6.1	0.29	0.07	2.3^e	0.0396	5.6	0.38	(17)
VS	A7	2.946	32.420	5.3	378	0.47	6.4	0.53	0.10	6.2^e	0.1073	10.3	5.01	(42)
VS	A21	5.133	28.663	4.4	400	0.43	7.6	0.51	0.10	5.5^e	0.0955	9.4	3.66	(42)
VS	IV Zw 015	5.407	28.064	4.4	407	0.22	5.9	0.26	0.07	4.2^e	0.0943	4.8	1.82	(17)
V	A68	9.272	9.153	4.6	322	0.25	6.7	0.29	0.08	10.0^e	0.2546	5.5	14.89	(17)
cVS	A75	9.862	21.255	3.4	432	0.29	7.7	0.34	0.08	3.2^e	0.0619	5.8	0.95	(42)
V	A76	10.002	6.818	3.9	294	0.48	9.6	0.65	0.14	1.5	0.0395	11.0	0.74	(20)
VS	A77	10.123	29.549	5.1	422	0.35	6.9	0.41	0.09	4.0^e	0.0712	7.9	1.71	(38)
VS	A84	10.444	21.374	3.4	417	0.32	7.1	0.38	0.08	5.0^e	0.1014	6.5	2.84	(20)
V	Z235	10.967	24.402	4.1	435	0.56	6.3	0.61	0.10	5.2^e	0.0830	10.9	3.22	(2)
V	A104	12.452	24.441	4.3	455	0.34	6.6	0.39	0.08	4.3^e	0.0815	7.1	2.01	(18)
V	A115	13.999	26.378	5.2	313	0.40	7.9	0.46	0.11	9.8^e	0.1971	9.0	14.59	(42)
V •	RXJ0058.9+2657	14.731	26.959	5.5	424	0.19	7.0	0.24	0.07	2.4^e	0.0470	4.6	0.44	(12)
V	IV Zw 038	16.868	32.462	5.3	471	0.42	9.3	0.53	0.10	1.5^e	0.0170	9.9	0.12	(3)
VS	A147	17.040	2.182	2.9	435	0.31	7.6	0.39	0.09	2.6^e	0.0447	6.2	0.54	(20)
VS	A160	18.255	15.489	4.1	309	0.21	7.2	0.25	0.08	2.3^e	0.0442	4.5	0.38	(42)
VS	A168	18.787	0.354	3.3	436	0.55	10.5	0.66	0.11	2.6	0.0448	11.0	0.95	(47)
S	RXJ0123.2+3327	20.801	33.461	5.0	379	0.32	5.4	0.34	0.08	1.2^e	0.0146	6.0	0.05	(45)
V	RXJ0123.6+3315	20.921	33.261	5.0	379	0.81	9.7	0.92	0.14	1.8^e	0.0164	17.1	0.20	(45)
V	A193	21.266	8.688	4.7	264	0.71	8.6	0.83	0.16	4.2	0.0491	15.4	1.59	(32)
VS	A189	21.353	1.741	3.1	436	0.31	6.7	0.39	0.09	1.3^e	0.0181	6.1	0.09	(42)
VS	A262	28.191	36.157	5.3	346	2.07	11.2	2.53	0.25	2.4	0.0163	48.6	0.55	(20)
VS	A267	28.203	1.019	2.8	437	0.33	6.5	0.38	0.08	9.7^e	0.2300	6.2	13.71	(10)
VS	A272	28.766	33.898	5.2	332	0.44	5.3	0.52	0.11	5.2^e	0.0872	10.1	3.27	(47)
VS	RXJ0228.2+2811	37.069	28.184	7.4	295	0.19	5.2	0.23	0.08	2.0^e	0.0350	4.9	0.26	(46)
VS	A376	41.534	36.887	5.9	570	0.56	8.2	0.68	0.10	5.1	0.0488	13.6	1.38	(7)
V	A400	44.412	6.006	8.9	266	0.58	9.3	0.73	0.15	2.1	0.0238	16.2	0.40	(47)
VS	A399	44.457	13.053	10.6	413	1.08	11.0	1.23	0.15	5.8	0.0722	28.8	6.40	(20)
VS	A401	44.737	13.573	10.6	474	1.70	10.6	1.84	0.17	7.8	0.0739	42.8	9.94	(20)
VS	Z808	45.409	1.927	7.5	239	0.21	4.8	0.24	0.08	6.8^e	0.1690	5.1	6.12	(10)
V	A407	45.456	35.835	9.8	485	0.19	5.5	0.23	0.06	2.5^e	0.0464	5.4	0.50	(42)
V	A409	45.849	1.926	7.1	259	0.20	4.6	0.22	0.08	6.1^e	0.1530	4.7	4.63	(10)
VS	2A0335+096	54.675	9.977	16.4	403	2.79	12.0	2.95	0.24	3.0	0.0349	80.5	4.21	(27)
VS	RXJ0341.3+1524	55.342	15.405	14.2	376	0.48	7.2	0.60	0.12	2.6^e	0.0290	15.5	0.56	(10)
VS	RXJ0352.9+1941	58.249	19.690	13.4	348	0.28	5.6	0.31	0.08	5.7^e	0.1090	7.9	3.98	(10)
VS	A478	63.359	10.466	13.9	285	1.48	9.7	1.57	0.20	6.8	0.0882	39.9	13.19	(47)
VS	RXJ0419.6+0225	64.911	2.420	10.8	289	1.70	14.5	1.95	0.23	2.1^e	0.0123	45.7	0.30	(45)
VS	RXJ0439.0+0715	69.755	7.260	10.2	377	0.19	4.9	0.23	0.07	9.5^e	0.2443	5.3	13.25	(17)
V	RXJ0439.0+0520	69.766	5.339	9.7	394	0.19	4.5	0.21	0.06	7.9^e	0.2080	4.8	8.62	(10)
VS	A520	73.531	2.920	7.4	412	0.34	5.4	0.40	0.09	9.8^e	0.2030	8.4	14.44	(37)
VS	A523	74.797	8.774	12.0	418	0.14	4.9	0.19	0.06	4.3^e	0.1000	4.5	1.94	(19)

Table 3 – *continued*

z, contam. extent, serend. flag	cluster name	α (J2000) [deg]	δ (J2000) [deg]	n_H [10^{20} cm^{-2}]	RASS exp. time [s]	VTP count rate [s^{-1}]	r_{VTP} [arcmin]	final count rate [s^{-1}]	count rate error [s^{-1}]	kT [keV]	z	f_X (0.1–2.4 kev) [10^{-12} erg cm^{-2} s^{-1}]	L_X (0.1–2.4 kev) [10^{44} erg s^{-1}]	z reference
VS	RXJ0503.1+0608	75.777	6.135	9.3	422	0.23	5.5	0.30	0.08	4.5[e]	0.0880	6.8	2.26	(10)
VS	A566	106.093	63.275	5.6	356	0.49	9.5	0.59	0.11	6.1[e]	0.0980	11.6	4.73	(42)
VS	Z1261	109.154	53.388	6.4	353	0.17	5.5	0.22	0.07	2.8	0.0644	4.5	0.81	(16)
VS	A576	110.382	55.764	5.4	278	0.98	10.3	1.15	0.18	3.7	0.0381	22.4	1.39	(47)
VS	A586	113.093	31.634	5.4	455	0.42	6.2	0.46	0.09	8.7[e]	0.1710	9.1	11.12	(37)
VS	UGC03957	115.239	55.437	4.7	402	0.90	8.7	1.00	0.14	3.2[e]	0.0341	18.6	0.93	(28)
VS	RXJ0751.3+5012	117.842	50.211	5.0	456	0.45	10.4	0.55	0.10	1.8[e]	0.0220	10.1	0.21	(12)
V	A602	118.351	29.366	4.3	436	0.32	6.4	0.38	0.08	3.4[e]	0.0621	6.9	1.14	(19)
VS	Z1478	119.919	53.999	4.0	445	0.24	6.3	0.29	0.07	4.6[e]	0.1038	5.2	2.38	(17)
VS	RXJ0819.6+6336	124.913	63.610	4.1	442	0.22	5.5	0.26	0.07	5.0[e]	0.1190	4.7	2.83	(11)
S	A646	125.547	47.100	4.0	406	0.34	4.7	0.35	0.08	6.0[e]	0.1303	6.3	4.54	(37)
V●	Z1665	125.798	4.356	3.1	242	0.45	7.4	0.59	0.15	2.2[e]	0.0293	9.6	0.36	(17)
VS	A655	126.361	47.132	4.0	332	0.44	8.1	0.55	0.12	7.1[e]	0.1267	9.9	6.73	(42)
V	A667	127.019	44.764	4.0	431	0.26	4.9	0.29	0.07	6.1[e]	0.1450	5.1	4.59	(10)
VS	A671	127.170	30.432	3.8	409	0.39	7.5	0.47	0.10	3.1[e]	0.0503	8.2	0.90	(20)
VS	A665	127.739	65.854	4.2	456	0.57	6.3	0.64	0.10	8.3	0.1818	11.8	16.33	(29)
c	A689	129.356	14.983	3.7	317	0.51	5.3	0.53	0.11	13.5[e]	0.2793	9.5	30.41	(17)
S	A697	130.741	36.365	3.4	261	0.26	4.3	0.29	0.09	10.5[e]	0.2820	5.0	16.30	(10)
⋆cVS	Z1953	132.542	36.086	3.1	362	0.29	8.0	0.35	0.09	14.5[e]	0.3737	6.1	34.12	(17)
V	Z2089	135.158	20.916	3.3	363	0.24	4.5	0.27	0.07	8.8[e]	0.2347	4.7	10.82	(17)
cVS	A750	137.299	10.989	3.6	379	0.40	6.6	0.47	0.10	8.1[e]	0.1630	8.3	9.30	(15)
V	A763	138.124	15.943	3.5	400	0.39	5.5	0.44	0.09	4.6[e]	0.0851	7.6	2.34	(19)
cV	A757	138.357	47.687	1.6	437	0.47	6.9	0.58	0.10	3.1[e]	0.0514	7.9	0.90	(22)
VS	A773	139.475	51.716	1.5	502	0.45	6.3	0.48	0.08	9.4[e]	0.2170	6.7	13.08	(19)
VS	A781	140.120	30.519	1.9	373	0.25	6.6	0.32	0.08	10.8[e]	0.2984	4.7	17.22	(17)
S	A795	141.024	14.168	3.5	411	0.39	5.6	0.42	0.09	6.6[e]	0.1357	7.3	5.66	(37)
c	Z2701	148.198	51.891	0.9	551	0.41	4.6	0.46	0.08	8.7[e]	0.2140	5.6	10.68	(10)
VS	Z2844	150.657	32.688	1.6	466	0.32	5.9	0.40	0.08	2.6[e]	0.0500	5.3	0.57	(21)
V	A961	154.085	33.641	1.5	472	0.29	5.5	0.35	0.08	5.2[e]	0.1241	4.8	3.14	(43)
V	A963	154.255	39.029	1.4	490	0.37	4.7	0.43	0.08	8.6[e]	0.2060	5.9	10.41	(42)
V	A980	155.617	50.121	1.0	551	0.50	5.5	0.55	0.09	7.4[e]	0.1582	7.0	7.35	(25)
V●	A990	155.912	49.145	1.0	542	0.63	6.0	0.70	0.10	7.5[e]	0.1440	8.8	7.73	(10)
S	Z3146	155.915	4.190	2.7	445	0.46	4.4	0.47	0.08	12.8[e]	0.2906	7.7	26.47	(2)
VS	Z3179	156.484	12.691	3.6	468	0.28	4.6	0.31	0.07	6.2[e]	0.1434	5.5	4.78	(2)
VS	A1033	157.932	35.058	1.6	473	0.50	5.2	0.55	0.09	6.3[e]	0.1259	7.6	5.13	(2)
S	A1068	160.187	39.951	1.5	406	0.63	5.0	0.69	0.11	7.5[e]	0.1386	9.4	7.65	(2)
V●	RXJ1053.7+5450	163.449	54.850	0.8	603	0.35	5.8	0.43	0.08	3.3[e]	0.0704	4.9	1.04	(17)
V	A1132	164.616	56.782	0.6	602	0.69	6.9	0.77	0.10	7.1[e]	0.1363	8.8	6.89	(37)
VS	A1177	167.363	21.728	1.2	327	0.33	7.0	0.42	0.10	1.9[e]	0.0319	5.0	0.22	(19)
V	A1185	167.695	28.706	1.7	263	0.35	7.0	0.46	0.12	3.9	0.0314	6.4	0.27	(20)
VS	A1190	167.869	40.830	1.6	361	0.32	6.1	0.40	0.09	3.8[e]	0.0794	5.4	1.47	(38)

Table 3 – *continued*

cluster name	z, contam. extent, serend. flag	α (J2000) [deg]	δ (J2000) [deg]	n_H [10^{20} cm^{-2}]	RASS exp. time [s]	VTP count rate [s^{-1}]	r_{VTP} [arcmin]	final count rate [s^{-1}]	count rate error [s^{-1}]	kT [keV]	z	f_X (0.1–2.4 keV) [10^{-12} erg cm^{-2} s^{-1}]	L_X (0.1–2.4 keV) [10^{44} erg s^{-1}]	z reference
A1201	V	168.225	13.450	1.7	424	0.32	4.9	0.36	0.08	6.9[e]	0.1688	5.2	6.28	(22)
A1204	S	168.337	17.596	1.4	351	0.39	4.2	0.43	0.09	7.3[e]	0.1706	5.9	7.26	(2)
A1235	VS	170.804	19.616	1.6	434	0.32	5.8	0.38	0.08	4.7[e]	0.1042	5.2	2.42	(42)
A1246	VS	170.977	21.488	1.4	434	0.33	5.1	0.37	0.08	7.5[e]	0.1904	5.0	7.62	(2)
A1302	V	173.307	66.399	1.1	679	0.38	5.1	0.42	0.07	5.1[e]	0.1160	5.3	3.05	(19)
A1314	V	173.748	49.090	1.6	428	0.29	6.1	0.40	0.09	5.0	0.0338	5.6	0.27	(47)
A1361	VS	175.917	46.374	2.0	353	0.37	4.5	0.41	0.09	5.5[e]	0.1167	6.2	3.59	(2)
A1367	V	176.152	19.759	2.3	454	4.63	11.4	5.36	0.32	3.5	0.0214	81.4	1.60	(47)
A1366	V	176.202	67.413	1.4	714	0.44	5.5	0.50	0.07	5.6[e]	0.1159	6.8	3.87	(19)
A1413	VS	178.826	23.408	2.0	468	0.92	7.8	1.03	0.13	8.9	0.1427	15.5	13.28	(42)
A1423	VS	179.342	33.632	1.6	488	0.31	5.2	0.37	0.08	8.5[e]	0.2130	5.3	10.03	(10)
A1437	VS	180.104	3.349	1.8	406	0.58	6.8	0.68	0.12	7.4[e]	0.1339	10.0	7.55	(22)
Z4803	VS	181.114	1.903	1.9	397	1.10	9.1	1.29	0.16	1.7	0.0200	17.7	0.30	(4)
RXJ1205.1+3920	S	181.299	39.342	2.0	432	0.42	4.9	0.46	0.09	2.3[e]	0.0370	6.5	0.38	(10)
MKW 4s	V•	181.647	28.180	1.7	488	0.35	6.2	0.46	0.09	1.8[e]	0.0283	6.0	0.21	(4)
Z4905	VS	182.571	5.392	1.5	437	0.29	4.8	0.35	0.08	3.5[e]	0.0770	4.7	1.20	(11)
Z5029	V•	184.422	3.659	1.7	404	1.39	8.1	1.54	0.17	6.3[e]	0.0750	22.0	5.28	(14)
RXJ1223.0+1037	S	185.774	10.620	2.0	444	0.48	4.6	0.49	0.09	1.8[e]	0.0257	6.8	0.19	(5)
Virgo	V	187.697	12.337	2.4	443	40.76	7.5	121.00	2.58	2.4	0.0036	821.1	1.00	(36)
A1553	V	187.700	10.556	2.1	445	0.37	4.7	0.42	0.08	7.4[e]	0.1652	6.3	7.30	(37)
Z5247	V•	188.572	9.770	1.7	440	0.26	4.8	0.32	0.08	8.5[e]	0.2290	4.6	10.12	(1)
A1589	V	190.325	18.551	1.9	462	0.62	7.4	0.74	0.11	4.6[e]	0.0718	10.8	2.39	(15)
A1656	VS	194.883	27.903	0.9	506	23.50	16.4	25.87	0.67	8.0	0.0231	319.2	7.26	(20)
A1668	VS	195.937	19.277	2.2	601	0.53	6.4	0.62	0.09	3.9[e]	0.0634	9.3	1.61	(31)
A1677	VS	196.471	30.886	1.1	525	0.31	5.0	0.35	0.07	6.9[e]	0.1832	4.4	6.24	(37)
A1682	VS	196.739	46.545	1.1	545	0.34	5.3	0.41	0.08	8.9[e]	0.2260	5.3	11.26	(2)
RXJ1320.1+3308	V•	200.035	33.143	1.0	548	0.34	5.8	0.40	0.08	2.0[e]	0.0362	4.6	0.26	(34)
RXJ1326.3+0013	VS	201.575	0.226	1.8	305	0.35	4.8	0.41	0.10	4.0[e]	0.0820	5.9	1.69	(11)
A1758b		203.126	50.409	1.1	590	0.15	3.8	0.17	0.05	7.5[e]	0.2800	2.2	7.25	(37)
A1758a	VS	203.189	50.548	1.1	591	0.25	4.5	0.28	0.06	9.1[e]	0.2800	3.6	11.68	(37)
A1763	VS	203.818	40.996	0.9	628	0.49	5.1	0.56	0.08	10.0[e]	0.2279	6.9	14.93	(22)
A1767	VS	204.032	59.211	1.6	748	0.74	7.1	0.86	0.10	4.1	0.0701	11.7	2.47	(47)
A1775	VS	205.460	26.382	1.0	383	0.92	7.0	1.05	0.15	4.9	0.0724	13.0	2.91	(20)
A1773	V	205.528	2.233	1.8	267	0.32	4.7	0.42	0.11	3.9[e]	0.0776	5.9	1.53	(20)
A1795	VS	207.218	26.598	1.2	429	5.05	10.5	5.34	0.31	5.1	0.0622	68.1	11.27	(20)
A1800	VS	207.365	28.106	1.2	441	0.84	8.2	1.00	0.14	5.1[e]	0.0748	12.8	3.05	(20)
A1809	V	208.275	5.158	2.0	407	0.35	5.8	0.41	0.09	3.9[e]	0.0790	6.0	1.61	(20)
A1831	V	209.802	27.978	1.3	473	0.78	7.1	0.91	0.12	4.2[e]	0.0612	11.9	1.90	(20)
A1835	VS	210.260	2.882	2.2	407	0.87	6.7	0.95	0.13	14.8[e]	0.2528	14.7	38.53	(2)
A1885	VS	213.432	43.661	1.2	752	0.51	5.4	0.56	0.07	4.6[e]	0.0890	7.1	2.40	(10)
Z6718	S	215.401	49.544	1.8	784	0.37	4.5	0.41	0.06	3.6[e]	0.0710	5.7	1.24	(2)

Table 3 – *continued*

z, contam. extent. serend. flag	cluster name	α (J2000) [deg]	δ (J2000) [deg]	n_H [10^{20} cm^{-2}]	RASS exp. time [s]	VTP count rate [s^{-1}]	r_{VTP} [arcmin]	final count rate [s^{-1}]	count rate error [s^{-1}]	kT [keV]	z	f_X (0.1–2.4 keV) [10^{-12} erg cm^{-2} s^{-1}]	L_X (0.1–2.4 keV) [10^{44} erg s^{-1}]	z reference
S	A1902	215.428	37.299	1.0	622	0.38	4.4	0.41	0.07	6.6e	0.1600	5.1	5.56	(10)
S	A1918	216.342	63.183	1.7	887	0.32	4.4	0.35	0.05	5.8e	0.1394	5.0	4.13	(38)
S	A1914	216.509	37.835	1.0	656	1.11	6.1	1.19	0.12	10.8e	0.1712	15.0	18.39	(22)
VS	A1927	217.765	25.628	2.0	556	0.36	5.6	0.41	0.08	4.4e	0.0908	6.1	2.14	(19)
cVS	A1930	218.120	31.633	1.1	484	0.38	6.1	0.44	0.08	5.8e	0.1313	5.6	4.09	(37)
V	MKW 8	220.156	3.467	2.7	335	0.92	10.4	1.16	0.17	2.7e	0.0276	18.4	0.60	(4)
VS	RXJ1442.2+2218	220.573	22.301	2.6	536	0.36	4.2	0.42	0.08	4.8e	0.0970	6.6	2.66	(11)
V	A1978	222.775	14.611	1.8	386	0.29	3.8	0.34	0.08	6.0e	0.1460	5.0	4.50	(11)
VS	A1983	223.248	16.709	2.0	396	0.32	4.7	0.38	0.09	2.5e	0.0444	5.5	0.47	(20)
S	A1991	223.629	18.650	2.4	405	0.56	5.5	0.60	0.10	5.4	0.0586	9.4	1.38	(19)
S	Z7160	224.310	22.344	3.1	426	0.27	4.0	0.28	0.07	9.6e	0.2578	4.8	13.19	(2)
V	A2009	225.085	21.362	3.2	378	0.49	5.0	0.54	0.10	7.8	0.1530	9.2	9.12	(9)
VS	A2034	227.545	33.506	1.5	610	0.83	7.1	0.92	0.11	7.1e	0.1130	12.7	6.85	(10)
V	A2029	227.729	5.720	3.0	443	3.37	9.2	3.67	0.26	7.8	0.0766	61.3	15.29	(47)
V	A2033	227.848	6.319	2.8	437	0.47	5.3	0.56	0.10	4.7e	0.0817	9.0	2.57	(19)
V	A2050	229.068	0.089	4.3	265	0.32	5.3	0.38	0.10	5.8e	0.1183	7.0	4.15	(37)
VS	A2052	229.176	7.002	2.8	449	2.60	8.3	2.92	0.23	3.4	0.0353	47.1	2.52	(33)
VS	A2055	229.672	6.211	3.1	433	0.57	4.7	0.65	0.11	6.1e	0.1021	10.9	4.82	(31)
S	A2064	230.221	48.672	1.8	797	0.44	4.9	0.47	0.07	5.3e	0.1076	6.8	3.33	(42)
V	A2061	230.321	30.640	1.9	395	0.88	9.7	1.04	0.15	5.6e	0.0777	15.3	3.95	(20)
VS	MKW 3s	230.507	7.699	3.1	352	1.65	6.3	1.84	0.20	3.0	0.0453	30.3	2.68	(4)
VS	A2065	230.612	27.711	2.8	382	1.17	8.7	1.35	0.17	8.4	0.0723	22.2	4.94	(20)
VS	A2063	230.757	8.580	2.9	412	1.99	8.6	2.30	0.21	4.1	0.0355	37.5	2.03	(20)
V ●	A2069	231.041	29.921	2.1	391	0.90	9.8	1.06	0.15	7.9e	0.1145	16.1	8.92	(19)
V	A2072	231.477	18.236	3.7	349	0.23	3.8	0.26	0.07	5.2e	0.1270	4.6	3.13	(11)
⋆S	RXJ1532.9+3021	233.226	30.353	2.1	324	0.29	3.9	0.33	0.09	12.5e	0.3450	5.0	24.40	(11)
V	A2107	234.910	21.789	4.4	405	0.69	7.2	0.83	0.13	4.2	0.0411	15.2	1.10	(30)
VS	A2111	234.924	34.417	2.0	384	0.27	4.9	0.33	0.08	8.8e	0.2290	5.0	10.94	(42)
VS	A2110	234.952	30.716	2.3	240	0.53	5.7	0.62	0.14	5.6e	0.0980	9.6	3.93	(35)
V	A2108	235.038	17.878	3.3	253	0.25	4.6	0.32	0.10	4.3e	0.0916	5.5	1.97	(37)
VS	A2124	236.250	36.066	1.7	277	0.43	6.1	0.53	0.12	3.7e	0.0654	7.3	1.35	(20)
V	A2142	239.592	27.233	3.8	555	3.23	11.9	3.44	0.22	11.0	0.0894	61.5	20.74	(42)
V	A2147	240.578	16.020	3.2	568	2.58	14.3	3.15	0.22	4.4	0.0353	53.2	2.84	(42)
VS	A2151a	241.179	17.726	3.3	580	0.76	7.7	0.88	0.11	3.5	0.0370	15.0	0.88	(20)
VS	AWM 4	241.238	23.946	4.8	620	0.47	6.3	0.55	0.08	3.7	0.0318	10.2	0.44	(4)
cV	A2151b	241.718	17.781	3.5	581	0.08	3.4	0.10	0.04	1.3e	0.0321	1.6	0.07	(20)
VS	A2175	245.128	29.892	2.6	692	0.40	6.1	0.46	0.07	5.0e	0.0972	7.3	2.93	(20)
VS	A2199	247.165	39.550	0.9	823	7.48	14.3	8.07	0.29	4.7	0.0299	96.8	3.70	(20)
S	A2204	248.195	5.574	5.3	541	1.06	5.4	1.12	0.12	11.4e	0.1524	21.9	21.25	(37)
VS	A2218	248.970	66.214	3.4	1937	0.39	5.0	0.44	0.04	6.7	0.1710	7.5	9.30	(37)
S	A2219	250.094	46.706	1.7	930	0.60	5.1	0.65	0.07	11.4e	0.2281	9.5	20.40	(2)

Table 3 – *continued*

z, contam. extent, serend. flag	cluster name	α (J2000) [deg]	δ (J2000) [deg]	n_H [10^{20} cm^{-2}]	RASS exp. time [s]	VTP count rate [s^{-1}]	r_{VTP} [arcmin]	final count rate [s^{-1}]	count rate error [s^{-1}]	kT [keV]	z	f_X (0.1–2.4 kev) [10^{-12} erg cm^{-2} s^{-1}]	L_X (0.1–2.4 kev) [10^{44} erg s^{-1}]	z reference
S	RXJ1651.1+0459	252.798	4.996	6.0	516	0.25	3.7	0.28	0.06	6.6^e	0.1540	5.6	5.62	(40)
VS	AWM5	254.464	27.860	4.6	807	0.20	5.7	0.24	0.05	2.6	0.0347	4.5	0.23	(4)
S	A2241	254.934	32.617	2.2	749	0.27	4.9	0.29	0.05	4.3^e	0.1013	4.4	1.94	(15)
VS	A2244	255.667	34.063	2.1	768	1.41	8.9	1.54	0.13	7.1	0.0970	23.4	9.34	(38)
VS	A2256	256.010	78.632	4.1	1455	2.50	13.0	2.72	0.12	7.5	0.0581	49.5	7.11	(47)
V	A2249	257.452	34.474	2.4	772	0.77	8.8	0.92	0.10	5.6^e	0.0802	14.4	3.95	(42)
VS	A2255	258.182	64.062	2.6	3527	0.98	9.3	1.10	0.05	7.3	0.0809	17.8	4.94	(47)
VS	RXJ1715.3+5725	258.826	57.427	2.6	1647	0.72	8.1	0.82	0.06	2.4^e	0.0280	12.7	0.43	(14)
VS	A2254	259.441	19.673	5.3	622	0.25	5.2	0.30	0.06	7.5^e	0.1780	5.8	7.73	(10)
S	Z8197	259.548	56.671	2.6	1467	0.31	4.8	0.33	0.04	5.0^e	0.1135	5.3	2.89	(11)
S	RXJ1720.1+2638	260.037	26.635	3.9	707	0.75	5.8	0.80	0.09	10.2^e	0.1640	14.3	16.12	(14)
S	A2259	260.040	27.669	3.8	716	0.30	4.7	0.33	0.06	7.1^e	0.1640	5.9	6.66	(10)
VS	A2261	260.615	32.127	3.2	768	0.46	5.7	0.51	0.07	10.8^e	0.2240	8.7	18.18	(10)
VS	A2294	260.980	85.890	6.1	1078	0.21	4.6	0.25	0.04	7.1^e	0.1780	5.0	6.62	(10)
VS	RXJ1733.0+4345	263.255	43.758	2.4	1110	0.67	6.2	0.76	0.07	2.6^e	0.0330	11.6	0.54	(11)
VS	RXJ1740.5+3539	265.133	35.652	2.8	897	0.34	5.0	0.40	0.06	2.5^e	0.0430	6.3	0.50	(11)
VS	Z8276	266.056	32.982	3.4	827	0.86	7.1	0.96	0.10	5.7^e	0.0757	16.4	4.02	(44)
S	RXJ1750.2+3505	267.567	35.083	3.0	869	0.24	4.1	0.26	0.05	6.6^e	0.1710	4.4	5.49	(11)
VS	Z8338	272.710	49.920	4.1	1566	0.40	6.4	0.46	0.05	3.0^e	0.0473	8.2	0.79	(23)
VS	A2312	283.451	68.385	5.7	2973	0.23	5.0	0.26	0.03	4.2^e	0.0928	5.1	1.89	(19)
c	A2318	286.433	78.083	4.8	1372	0.27	4.3	0.28	0.04	6.0^e	0.1405	5.3	4.40	(2)
VS	II Zw 108	318.526	2.569	6.2	462	0.92	12.0	1.09	0.14	4.4^e	0.0483	21.9	2.19	(19)
VS	RXJ2129.6+0005	322.408	0.094	4.3	287	0.39	5.4	0.44	0.11	11.0^e	0.2350	8.1	18.59	(11)
VS	A2390	328.403	17.692	6.6	267	0.41	5.4	0.47	0.11	11.6^e	0.2329	9.6	21.44	(26)
VS	A2409	330.227	20.959	6.4	312	0.38	6.5	0.43	0.10	7.6^e	0.1470	8.8	8.06	(2)
VS	RXJ2214.7+1350	333.699	13.834	4.9	280	0.22	7.3	0.28	0.09	1.6^e	0.0263	5.1	0.15	(24)
V	A2443	336.511	17.378	4.9	476	0.32	7.1	0.35	0.07	5.2^e	0.1072	6.6	3.23	(37)
V	A2457	338.918	1.526	5.4	165	0.39	6.3	0.50	0.16	3.8^e	0.0591	9.6	1.44	(18)
VS	A2495	342.571	10.917	4.9	407	0.56	8.4	0.62	0.11	5.0^e	0.0768	11.8	2.98	(19)
VS	Z8852	347.629	7.583	5.1	446	0.60	12.1	0.72	0.11	3.2^e	0.0400	13.8	0.94	(8)
VS	A2572a	349.294	18.691	4.7	465	0.61	9.4	0.72	0.11	2.5	0.0422	13.4	1.03	(13)
VS	A2572b	349.612	18.724	4.7	466	0.45	8.2	0.54	0.10	2.8^e	0.0389	10.0	0.65	(13)
V	A2589	350.973	16.809	3.9	459	1.23	9.8	1.43	0.16	3.7	0.0416	25.3	1.88	(47)
VS	A2593	351.084	14.651	4.1	448	0.70	10.0	0.83	0.12	3.1	0.0428	14.8	1.17	(6)
V	A2622	353.771	27.370	5.3	503	0.30	8.3	0.35	0.07	3.4^e	0.0613	6.7	1.09	(38)
VS	A2626	354.142	21.128	4.1	489	0.69	9.6	0.80	0.11	2.9	0.0565	14.3	1.96	(15)
	A2627	354.174	23.930	4.1	471	0.25	4.1	0.28	0.07	5.3^e	0.1245	5.0	3.33	(10)
V	A2634	354.615	27.022	4.9	613	1.03	15.3	1.22	0.13	3.4	0.0309	23.1	0.95	(47)
V	A2657	356.237	9.201	5.6	441	1.06	10.5	1.20	0.15	3.4	0.0400	23.4	1.61	(47)
VS	Z9077	357.644	29.531	5.3	251	0.23	5.2	0.28	0.09	4.4^e	0.0950	5.5	2.11	(41)
VS	A2665	357.713	6.138	5.5	437	0.63	8.7	0.72	0.11	4.2^e	0.0562	14.1	1.90	(39)
VS	A2675	358.962	11.355	4.8	439	0.36	9.0	0.46	0.09	4.2^e	0.0720	8.6	1.90	(18)

point sources; 'V' ('S') signals significant X-ray extent according to VTP (SASS), i.e. an extent value in excess of 35 arcsec; systems flagged by a filled circle are serendipitous VTP detections in the sense of Section 7.1.

column 2: cluster name. Where clusters appear to consist of two components, two entries ('a' and 'b') are listed.

column 3: right ascension (J2000) of the X-ray position as determined by VTP.

column 4: declination (J2000) of the X-ray position as determined by VTP.

column 5: column density of Galactic hydrogen from Stark et al. (1992).

column 6: RASS exposure time (accumulated).

column 7: PSPC count rate in PHA channels 11 to 235 originally detected by VTP.

column 8: the equivalent radius $\sqrt{A_{\mathrm{VTP}}/\pi}$ of the source detected by VTP.

column 9: final PSPC count rate in Pulse Height Analyser (PHA) channels 11 to 235 based on the original VTP count rate. Statistical corrections for low-surface-brightness emission that has not been detected directly and for contamination from point sources have been applied.

column 10: error in the final PSPC count rate according to equation (4). The fractional uncertainty in the energy flux (column 13) and the X-ray luminosity (column 14) can be assumed to be the same as the fractional count rate error.

column 11: ICM gas temperature used in the conversion from count rates to energy fluxes. 'e' indicates that the temperature has been estimated from the $L_{\mathrm{X}}-kT$ relation.

column 12: redshift.

column 13: unabsorbed X-ray energy flux in the 0.1–2.4 keV band.

column 14: intrinsic X-ray luminosity in the 0.1–2.4 keV band (cluster rest frame).

column 15: reference for the redshift in column 12.

The source positions listed in columns 3 and 4 of Table 3 are typically good to about 1 arcmin. Depending on the angular extent of the emission (as indicated by the equivalent detection radius quoted in column 8) and the presence of substructure and/or contaminating point sources (usually unknown), somewhat larger positional errors for individual sources cannot be ruled out.

12 SUMMARY

We present the *ROSAT* Brightest Cluster Sample (BCS), an X-ray flux-limited sample of clusters of galaxies in the northern extragalactic sky ($\delta \geq 0°$, $|b| \geq 20°$). Although the bulk of the BCS clusters are Abell clusters (~70 per cent), the sample also contains a considerable number of Zwicky clusters (~10 per cent) as well as purely X-ray-selected systems (~20 per cent). In terms of being a representative cluster sample, the BCS constitutes a significant improvement over the all-sky XBACs sample of EVB which is of similar size but limited to ACO clusters. The procedures followed during the compilation of the BCS are in many ways very similar to those devised by EVB for the compilation of the XBACs sample. An overview of the compilation procedure is given in Fig. 26.

We confirm the finding of EVB that the compilation of a properly flux-limited cluster sample from the RASS data is impossible from SASS output alone. The reprocessing of the RASS photon event files with VTP, a source detection algorithm developed specifically for the detection of low-surface-brightness emission of essentially arbitrary geometry, is thus of vital importance for the compilation of the BCS. A comparison with the VTP count rates for clusters with $S > 2 \times 10^{-12}$ erg cm^{-2} s^{-1} shows the SASS count rates to be too low by typically a factor of 0.64 (median), with the 10th and 90th percentiles being 0.35 and 0.84. Any SASS count rate limited cluster sample will thus necessarily be incomplete. Since the compilation of the BCS started from just that, i.e. a count rate limited SASS source list, and VTP was run only on part of our study area, our final cluster sample is incomplete even at fluxes as high as 4×10^{-12} erg cm^{-2} s^{-1} (0.1–2.4 keV). However, a set of 95 clusters detected serendipitously by VTP allows this incompleteness to be accurately quantified and corrected for.

After correction for incompleteness, we find the $\log N - \log S$ distribution of our clusters to follow a power law of slope -1.31 down to X-ray fluxes of about 2×10^{-12} erg cm^{-2} s^{-1}. Although the canonical Euclidean value of -1.5 is formally ruled out by our measurement, the observed flattening of the $\log N - \log S$ distribution with decreasing flux is not indicative of cluster evolution. Rather, it can be attributed to cosmological effects in an expanding universe. If these are taken into account we find the BCS $\log N - \log S$ distribution to be consistent with a non-evolving cluster population down to the quoted flux level. Using the best-fitting power law to quantify the level of completeness of the BCS cluster list, we compile two flux-limited subsamples with limiting fluxes of 3.1×10^{-12} and 4.4×10^{-12} erg cm^{-2} s^{-1}. The flux completeness of these samples is 80 and 90 per cent, respectively. Since clusters at a redshift higher than about 0.3 cannot be reliably confirmed with the presently available optical plate material, thus requiring additional optical follow-up, we limit our statistical sample to systems at $z \leq 0.3$. Within this redshift, the 80 and 90 per cent complete BCS contains 276 and 201 clusters, respectively, if subclusters are counted separately. All clusters in the 90 per cent complete sample have measured redshifts as listed in Table 3.

The redshift distribution of the BCS shows intriguing evidence for large-scale inhomogeneities in the form of cluster overdensities

References to Table 3

(1) Allen, private communication, (2) Allen et al. (1992), (3) Andersen & Owen (1994), (4) Beers et al. (1995), (5) Binggeli, Sandage & Tammann (1985), (6) Bothun & Schombert (1990), (7) Capelato et al. (1991), (8) Chincarini & Rood (1976), (9) Ciardullo et al. (1983), (10) Crawford et al. (1995), (11) Crawford et al., in preparation, (12) Davoust & Considere (1995), (13) Ebeling et al. (1995), (14) Elvis et al. (1992), (15) Fetisova (1982), (16) Gregory & Burns (1982), (17) Ebeling, Henry & Mullis, in preparation, (18) Hoessel, Gunn & Thuan (1980), (19) Huchra, private communication, (20) Huchra et al. (1992), (21) Huchra, Geller & Corwin (1995), (22) Karachentsev & Kopylov (1981), (23) Karachentsev, Lebedev & Shcherbanovskij (1985), (24) Lacy et al. (1993), (25) Lebedev & Lebedeva (1991), (26) Le Borgne et al. (1991), (27) McNamara, Bregman & O'Connell (1990), (28) Michel & Huchra (1988), (29) Oegerle, Fitchett & Hill (1991), (30) Oegerle & Hill (1992), (31) Owen, Ledlow & Keel (1995), (32) Postman & Lauer (1995), (33) Quintana et al. (1985), (34) Ramella, Geller & Huchra (1995), (35) Rhee & Katgert (1988), (36) Sandage & Tammann (1995), (37) Sarazin, Rood & Struble (1982), (38) Schneider, Gunn & Hoessel (1983), (39) Shectman (1985), (40) Spinrad et al. (1985), (41) Stocke et al. (1991), (42) Struble & Rood (1987), (43) Tago, private communication, (44) Ulrich (1976), (45) de Vaucouleurs et al. (1991), (46) Wegner, Haynes & Giovanelli (1993), (47) Zabludoff, Huchra & Geller (1990).
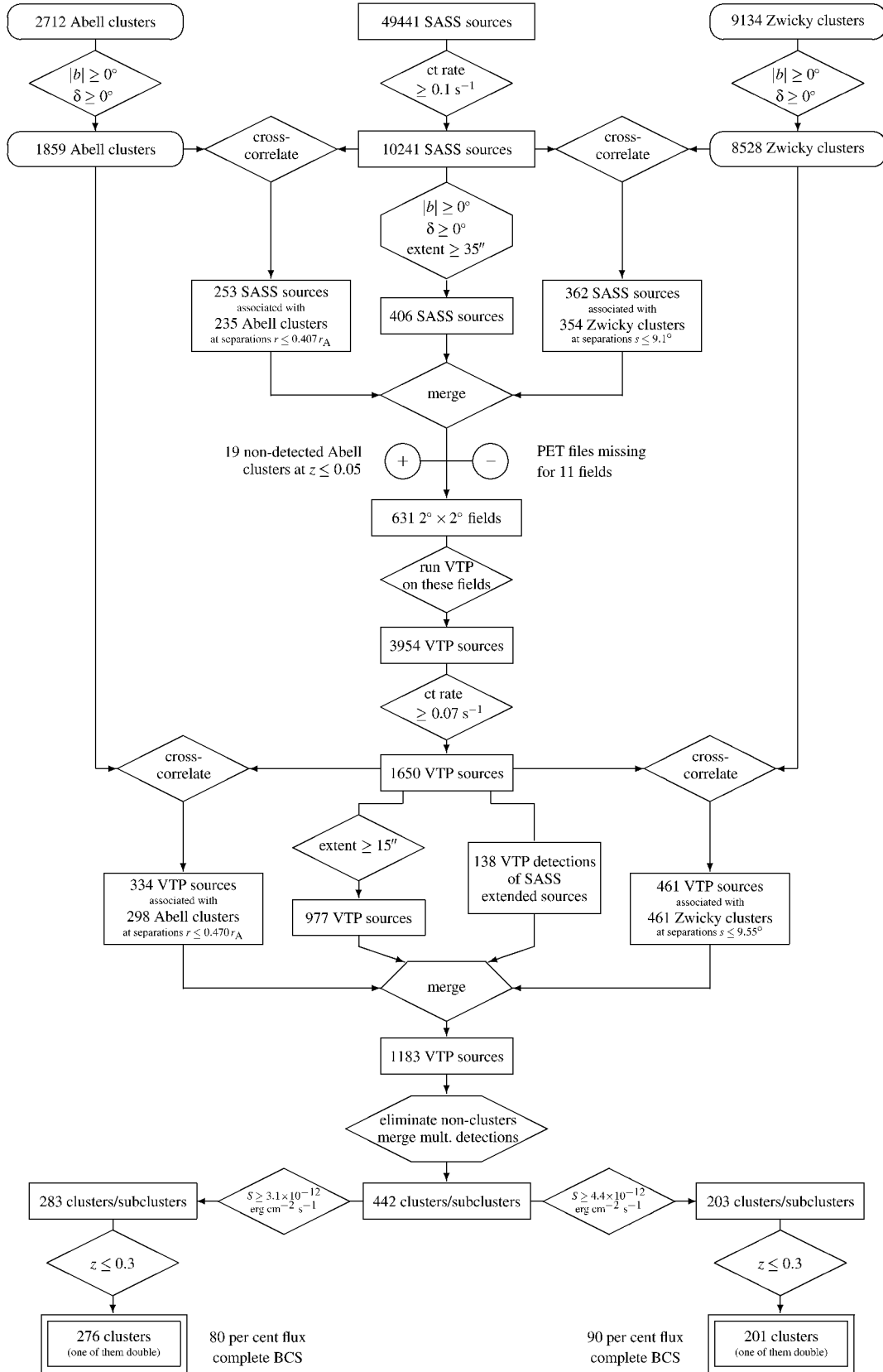
Figure 26. Flow diagram summarizing the compilation of the BCS.

at certain redshifts. We stress that the observed peaks in the redshift distribution can only partly be explained by contributions from any single supercluster.

We assess the statistical quality of strictly X-ray-selected cluster samples by comparing the X-ray extent and hardness ratio distributions for clusters and point sources. Cluster samples with a high degree of completeness (85 to 90 per cent) can be compiled from VTP detections if thresholds are applied to both the X-ray extent and the spectral hardness of the selected sources. The point source contamination of the resulting cluster samples will be about 55 per cent; if an improved VTP algorithm were used the contamination could be reduced to some 35 per cent. This is also the level of contamination expected for a purely X-ray-selected cluster sample based on SASS detections. However, owing to the inefficiency of the SASS extent criterion, the completeness of an SASS-selected cluster sample will always remain below 70 per cent.

The BCS is the largest X-ray-selected, flux-limited sample of clusters of galaxies compiled to date. Besides its obvious importance as a target list for on-going and future X-ray missions, the BCS will allow detailed studies of a whole series of cluster statistics, such as the spatial two-point correlation function or the cluster X-ray luminosity function (Ebeling et al. 1997), to name but two.

ACKNOWLEDGMENTS

REFERENCES

Abell G. O., 1958, ApJS, 3, 211

Abell G. O., Corwin H. G., Olowin R. P., 1989, ApJS, 70, 1 (ACO)

Allen S. W. et al., 1992, MNRAS, 259, 67

Anders E., Grevesse N., 1989, Geochim. Cosmochim. Acta, 53, 197

Andersen V., Owen F. N., 1994, AJ, 108, 361

Bahcall N. A., 1991, ApJ, 376, 43

Beers T. C., Kriessler J. R., Bird C. M., Huchra J. P., 1995, AJ, 109, 874

Binggeli B., Sandage A., Tammann G. A., 1985, AJ, 90, 1681

Böhringer H., Briel U. G., Schwarz R. A., Voges W., Hartner G., Trümper J., 1994, Nat, 368, 828

Bothun G. D., Schombert J. M., 1990, ApJ, 360, 436

Briel U. G., Henry J. P., Böhringer H., 1992, A&A, 259, L31

Broadhurst T. J., Ellis R. S., Koo D. C., Szalay A. S., 1990, Nat, 343, 726

Capelato H. V., Mazure A., Proust D., Vanderriest C., Lemonnier J. P., Sodré L., Jr, 1991, A&AS, 90, 355

Cavaliere A., Fusco-Femiano R., 1976, A&A, 49, 137

Chincarini G., Rood H. J., 1976, PASP, 88, 388

Ciardullo R., Ford H., Bartko F., Harms R., 1983, ApJ, 273, 24

Collins C. A., Guzzo L., Nichol R. C., Lumsden S. L., 1995, MNRAS, 274, 1071

Crawford C. S., Edge A. C., Fabian A. C., Allen S. W., Böhringer H., Ebeling H., McMahon R.G., Voges W., 1995, MNRAS, 274, 75

Cruddace R. G., Hasinger G., Trümper J., Schmidt J. H. M. M., Hartner G. D., Rosso C., Snowden S. L., 1991, Exp. Astron., 1, 365

Dalton G. B., Efstathiou G., Maddox S. J., Sutherland W. J., 1992, ApJ, 390, L1

David L. P., Slyz A., Jones C., Forman W., Vrtilek S. D., Arnaud K. A., 1993, ApJ, 412, 479

Davoust E., Considere S., 1995, A&AS, 110, 19

De Grandi S., 1996, in Zimmermann H. U., Trümper J., eds, MPE Report 263, Röntgenstrahlung from the Universe. MPE, p. 577

de Vaucouleurs G., de Vaucouleurs A., Corwin H. G., Buta R. J., Paturel G., Fouqué P., 1991, Third Reference Catalogue of Bright Galaxies. Springer, New York

Ebeling H., 1993, PhD thesis, Ludwig-Maximilian Universität München, MPE report 250

Ebeling H., Wiedenmann G., 1993, Phys. Rev. E, 47, 704

Ebeling H., Voges W., Böhringer H., Edge A. C., 1993, A&A, 275, 360

Ebeling H., Voges W., Böhringer H., 1994, ApJ, 436, 44

Ebeling H., Mendes de Oliveira C., White D. A., 1995, MNRAS, 277, 1006

Ebeling H., Voges W., Böhringer H., Edge A. C., Huchra J. P., Briel U. G., 1996, MNRAS, 281, 799 (EVB)

Ebeling H., Edge A. C., Fabian A. C., Allen S. W., Crawford C. S., Böhringer H., 1997, ApJ, 479, L101

Edge A. C., Stewart G. C., Fabian A. C., Arnaud K. A., 1990, MNRAS, 245, 559

Einasto J. et al., 1997, MNRAS, 289, 801

Elvis M., Plummer D., Schachter J., Fabbiano G., 1992, ApJS, 80, 257

Fetisova T., 1982, SvA, 25, 647

Frenk C. S., White S. D. M., Efstathiou G., Davis M., 1990, ApJ, 351, 10

Gioia I. M., Luppino G. A., 1994, ApJS, 94, 583

Gioia I. M., Maccaro T., Schild R. E., Stocke J. T., Liebert J. W., Danziger I. J., Kunth D., Lub J., 1984, ApJ, 283, 495

Gioia I. M., Henry J. P., Maccaro T., Morris S. L., Stocke J. T., Wolter A., 1990, ApJ, 356, L35

Gregory S. A., Burns J. O., 1982, ApJ, 255, 373

Guzzo L. et al., 1995, in Maddox S. J., Aragón-Salamanca A., eds, Wide Field Spectroscopy and the Distant Universe. World Scientific, Singapore, p. 205

Hasinger G., Boese G., Predehl P., Turner T. J., Yusaf R., George I. M., Rohrbach G., 1994, HEASARC LEGACY No. 4 , NASA Publication, p. 40

Henry J. P., Gioia I. M., Maccaro T., Morris S. L., Stocke J. T., Wolter A., 1992, ApJ, 386, 408

Hoessel J. G., Gunn J. E., Thuan T. X., 1980, ApJ, 241, 466

Huchra J. P., Henry J. P., Postman M., Geller M. J., 1990, ApJ, 365, 66

Huchra J. P., Geller M. J., Clemens C. M., Tokarz S. P., Michel A., 1992, Bull. Inform. CDS, 41, 31

Huchra J. P., Geller M. J., Corwin H. G., 1995, ApJS, 99, 391

Irwin M., Maddox S., McMahon R., 1994, Spectrum, 2, 14

Jones C., Forman W., 1984, ApJ, 276, 38

Jones L. R., Scharf C., Ebeling H., Perlman E., Wegner G., Malkan M., Horner D., 1998, ApJ, 495, 100

Karachentsev I. D., Kopylov A. I., 1981, Sov. Astron. Lett., 7, 285

Karachentsev I., Lebedev V., Shcherbanovskij A., 1985, Bull. Inform. CDS, 29, 87

Lacy M., Hill G. J., Kaiser M.-E., Rawlings S., 1993, MNRAS, 263, 707

Lebedev V. S., Lebedeva I. A., 1991, Bull. Spec. Astrophys. Obs. North Caucasus, 31, 88

Le Borgne J.-F., Mathez G., Mellier Y., Pello R., Sanahuja B., Soucail G., 1991, A&AS, 88, 133

Ledlow M. J., Owen F. N., 1996, AJ, 112, 9

Lucey J. R., 1983, MNRAS, 204, 33

Lumsden S. L., Nichol R. C., Collins C. A., Guzzo L., 1992, MNRAS, 258, 1

Luppino G. A., Gioia I. M., 1995, ApJ, 445, L77

Maccacaro T., Wolter A., McLean B., Gioia I. M., Stocke J. T., Della Ceca R., Burg R., Faccini R., 1994, Astrophys. Lett. Comm., 29, Nos 5–6

McHardy I., 1978, MNRAS, 184, 783

McNamara B. R., Bregman J. N., O'Connell R. W., 1990, ApJ, 360, 20

Michel A., Huchra J., 1988, PASP, 100, 1423

Nichol R. C., Briel U. G., Henry J. P., 1994, MNRAS, 267, 771

Nichol R. C., Holden B. P., Romer A. K., Ulmer M. P., Burke D. J., Collins C. A., 1997, ApJ, 481, 644

Oegerle W. R., Hill J. M., 1992, AJ, 104, 2078

Oegerle W. R., Fitchett M. J., Hill J. M., 1991, ApJ, 376, 46

Owen F. N., Ledlow M. J., Keel W. C., 1995, AJ, 109, 14

Piccinotti G., Mushotzky R. F., Boldt E. A., Holt S. S., Marshall F. E., Serlemitsos P. J., Shafer R. A., 1982, ApJ, 253, 485

Postman M., Lauer T. R., 1995, ApJ, 440, 28

Postman M., Huchra J. P., Geller M. J., 1992, ApJ, 384, 404

Postman M., Lubin L. M., Gunn J. E., Oke J. B., Hoessel J. G., Schneider D. P., Christensen J. A., 1996, AJ, 111, 615

Quintana H., Melnick J., Infante L., Thomas B., 1985, AJ, 90, 410

Ramella M., Geller M. J., Huchra J. P., 1995, AJ, 109, 145

Rhee G., Katgert P., 1988, A&AS, 72, 243

Romer A. K., Collins C. A., Böhringer H., Cruddace R. G., Ebeling H., MacGillivray H. T., Voges W., 1994, Nat, 372, 75

Rosati P., Della Ceca R., Burg R., Norman C., Giacconi R., 1995, ApJ, 445, L11

Sandage A., Tammann G. A., 1995, ApJ, 446, 1

Sarazin C. L., Rood H. J., Struble M. F., 1982, A&A, 108, L7

Scaramella R., Zamorani G., Vettolani G., Chincarini G., 1991, AJ, 101, 342

Scharf C. A., Jones L. R., Ebeling H., Perlman E., Malkan M., Wegner G., 1997, ApJ, 477, 79

Schneider D. P., Gunn J. E., Hoessel J. G., 1983, ApJ, 264, 337

Schwartz D. A., 1978, ApJ, 220, 8

Shectman S. A., 1985, ApJS, 57, 77

Spinrad H., Djorgovski S., Marr J., Aguilar L., 1985, PASP, 97, 932

Stark A. A., Gammie C. F., Wilson R. W., Bally J., Linke R. A., Heiles C., Hurwitz M., 1992, ApJS, 79, 77

Stocke J. T., Morris S. L., Gioia I. M., Maccacaro T., Schild R., Wolter A., Fleming T. A., Henry J. P., 1991, ApJS, 76, 813

Struble M. F., Rood H. J., 1987, ApJS, 63, 543

Struble M. F., Rood H. J., 1991, ApJ, 374, 395

Sutherland W. J., 1988, MNRAS, 234, 159

Trümper J., 1990, Phys. Bl., 46 (5), 137

Ulrich M.-H., 1976, ApJ, 206, 364

van de Weygaert R., 1991, MNRAS, 249, 159

van Haarlem M. P., Frenk C. S., White S. D. M., 1997, MNRAS, 287, 817

Voges W., 1992, Proc. Satellite Symp. 3, ESA ISY-3, p. 9

Voges W. et al., 1992, Proc. Satellite Symp. 3, ESA ISY-3, p. 223

Voges W. et al., 1996, IAU Circ. 6420, 2

Wallin J. F., Yentis D., MacGillivray H. T., Bauer S. B., Wong C. S., 1994, BAAS, 184, 2704

Wegner G., Haynes M., Giovanelli R., 1993, AJ, 105, 1251

White D. A., Jones C., Forman W., 1997, MNRAS, 292, 419

Zabludoff A. I., Huchra J. P., Geller M. J., 1990, ApJS, 74, 1

Zucca E., Zamorani G., Scaramella R., Vettolani G., 1993, ApJ, 407, 470

Zwicky F., Herzog E., Wild P., Karpowicz M., Kowal C. T., 1961–68, Catalogue of galaxies and cluster galaxies, Vols 1–6

APPENDIX A: THE STATISTICAL QUALITY OF STRICTLY X-RAY-SELECTED RASS CLUSTER SAMPLES

Having selected our final flux-limited sample, we can now assess the efficiency of cluster selection by X-ray properties alone. To this end, we compare the distributions of the two relevant source characteristics, X-ray extent and spectral hardness, for point sources and clusters.

Since, in the conversion from count rates to energy fluxes, different spectral models have to be assumed for clusters and point-like sources such as stars or AGN, this comparison cannot be performed as a function of source flux. We use the detected VTP count rate instead, and compute the count rate limits which, for clusters of galaxies, correspond to limiting fluxes of 2×10^{-12}, 3.1×10^{-12} and 4.4×10^{-12} erg cm^{-2} s^{-1} i. e. the lowest possible flux limit for an X-ray-selected cluster sample based on the RASS data in the northern hemisphere, and the BCS flux limits of 80 and 90 per cent flux completeness.

A1 Source extent

Fig. A1 shows the cumulative, fractional distributions of the VTP extent parameter for BCS clusters and other, non-cluster sources at the intermediate of the three quoted count rate limits. For an extent threshold of 35 arcsec, some 80 per cent of the clusters are
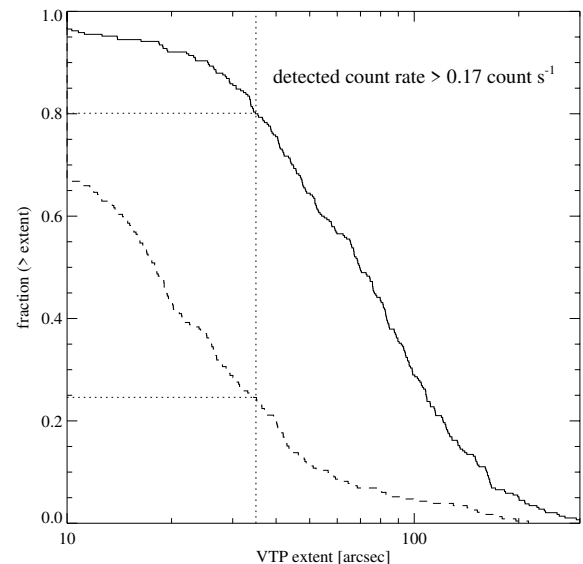

Figure A1. The cumulative extent distribution of galaxy clusters (solid line) in our sample of VTP detections, and the corresponding extent distribution of non-cluster sources of comparable brightness (dashed line). The count rate cut at 0.17 count s^{-1} corresponds roughly to the BCS flux limit of 80 per cent completeness at 3.1×10^{-12} erg cm^{-2} s^{-1}. The dotted lines mark the fraction of clusters and non-cluster sources classified as extended by VTP when the extent threshold is set to 35 arcsec; the intercepts with the ordinate change only slightly when count rate cuts corresponding to 2×10^{-12} and 4.4×10^{-12} erg cm^{-2} s^{-1} are chosen.

recognized as extended. We find this fraction to change only by a few per cent when all VTP detections brighter than 2×10^{-12} erg cm^{-2} s^{-1} are considered or only the ones featuring fluxes in excess of 4.4×10^{-12} erg cm^{-2} s^{-1}, the flux limit of the 90 per cent complete flux-limited BCS. Although a cluster sample selected by VTP extent alone would thus be highly complete (note that a completeness of about 90 per cent is achievable at all flux levels if the extent threshold is lowered to 25 arcsec), there is a massive penalty for this high degree of completeness. Some 25 per cent of all non-cluster sources, too, are classified as extended by VTP, again almost independently of the chosen flux limit. By comparison, the fraction of point sources misclassified as extended by the SASS is less than 10 per cent at the same numerical extent value of 35 arcsec (Ebeling et al. 1993).

The reason for the high fraction of point sources erroneously classified as extended by VTP is twofold. First, there is the effect of the spectral hardness of the sources. The flux correction procedure that determines the X-ray extents of VTP-detected sources (see Section 4) uses the PSPC point spread function for a nominal photon energy of 1 keV. Since the width of the PSF increases with decreasing photon energy, very soft sources will appear extended if a too narrow, high-energy PSF is used in the extent determination. This effect accounts for about 25 per cent of the erroneous extents. It could, in principle, be heavily suppressed by matching the PSF to the spectral hardness of each individual source (see Section 13.2 for a discussion of the significance of X-ray hardness ratios).

The second cause for erroneous VTP extents is of a more complex nature. Recent simulations by Scharf et al. (1997, see also Jones et al. 1998) indicate that a large fraction of the erroneous extent classifications of VTP may be caused by the inclusion of 'positive noise' in the percolation stage of the detection process. This problem can, however, be almost completely overcome by raising the detection threshold by some 30 per cent with respect to the surface brightness of the background. Although this leads necessarily to lower detected fluxes, it turns out that the loss in detected flux is entirely compensated for in the flux correction step described in detail in Section 4. According to Scharf and co-workers, this procedure reduces the fraction of point sources erroneously classified as extended to less than 10 per cent i.e. a value comparable to that obtained with the SASS.

A2 Spectral hardness

The second source characteristic that is a promising discriminator between clusters of galaxies and other X-ray sources is the spectral hardness of the detected emission. Following EVB, we define the hardness ratio HR as

$$HR = \frac{h - s}{h + s},$$

where h are the photon counts in the hard energy range from 0.5 to 2 keV, and s those in the softer 0.1–0.4 keV band. Using the same definition of HR, Ebeling et al. (1993) found more than 90 per cent of all Abell clusters detected by the SASS in the RASS data to feature HR values greater than zero. A more stringent criterion can be obtained by taking into account the X-ray-absorbing column density of Galactic hydrogen, n_H, in the direction of the cluster (EVB, fig. 10). Fig. A2 shows the observed hardness ratios as determined by VTP as a function of n_H for all BCS clusters with detected count rates greater than ~ 0.11 count s^{-1}, the count rate equivalent of the lowest possible RASS flux limit of completeness
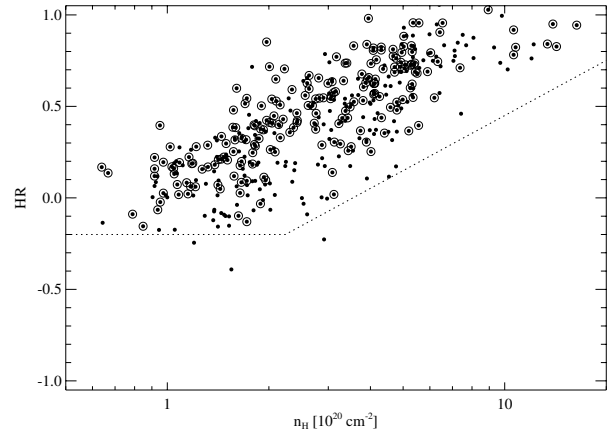

Figure A2. The X-ray spectral hardness ratio as a function of the Galactic column density of neutral hydrogen for all BCS clusters with detected count rates in excess of 0.11 count s^{-1}. The dotted line marks the 99 per cent lower limit of the distribution. Note that none of the clusters of the 90 per cent complete sample (shown encircled) falls below the dotted line.
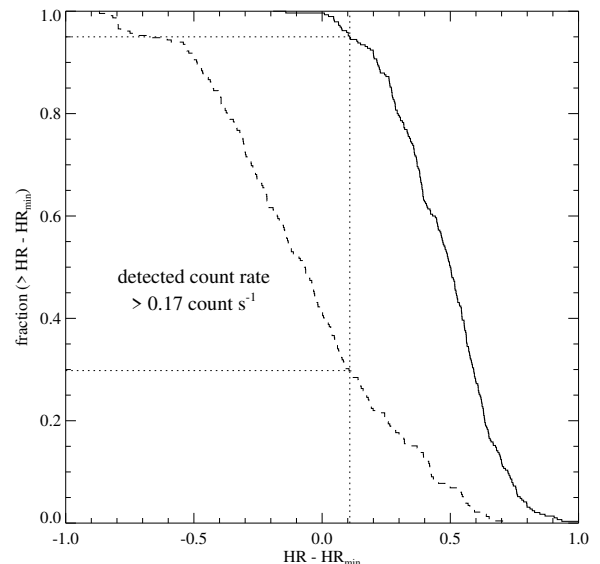

Figure A3. The cumulative hardness ratio distribution for the galaxy clusters (solid line) in our sample of VTP detections and the corresponding HR distribution for non-cluster sources of comparable brightness (dashed line). The count rate cut of 0.17 count s^{-1} corresponds roughly to the BCS flux limit of 80 per cent completeness at 3.1×10^{-12} erg cm^{-2} s^{-1}. The dotted lines mark the loci of 95 per cent completeness for clusters of galaxies; the intercept with the abscissa moves to slightly lower (higher) values when count rate cuts corresponding to $2(4.4) \times 10^{-12}$ erg cm^{-2} s^{-1} are chosen.

at 2×10^{-12} erg s^{-2} cm^{-2}. The dotted line, given by

$$HR_{min} = \max\left(-0.55 + \log\frac{n_H}{10^{20}\ \text{cm}^{-2}}; -0.2\right), \tag{A1}$$

marks a lower limit to the hardness ratio of X-ray emission from groups and clusters of galaxies (99 per cent confidence). It is also a 98 per cent lower limit to the HR values of the VTP detections of ACO clusters of the extended (unpublished) sample of EVB.

As can be seen from Fig. A3, discarding all VTP sources with spectral hardness ratios below HR_{min} as given by equation (A1)

excludes about 70 per cent of all point sources while leaving the cluster detections essentially unaffected. Owing to a weak correlation between spectral hardness and source brightness for clusters, and a weak anticorrelation between the same quantities for point sources, the HR threshold resulting in a 95 per cent complete cluster sample can be increased slightly when only sources above the count rate limits of our 80 and 90 per cent complete BCS subsamples are considered.

Although a cluster sample selected by X-ray hardness ratio alone will thus be highly complete, the remaining contamination from point sources will still be significant and, in fact, even stronger than for a purely X-ray-extent-selected sample.

A3   Combining source extent and hardness ratio

A high fraction of point sources erroneously classified as extended or a significant fraction of point sources with cluster-like hardness ratios lead to a severe contamination by point sources for an X-ray-selected cluster sample. Since, in the RASS data, stars, X-ray binaries and AGN together outnumber groups and clusters of galaxies by about 10 to 1, a total fraction p of hard or extended point sources will result in a point source contamination of $10p/(10p + c)$, where c is the chosen completeness of the sample. If, for instance, the contamination by point sources is to be limited to 50 per cent and, at the same time, 90 per cent completeness is aimed for, then p is required to be less than 0.09.

It is obvious from Figs A1 and A3 that this goal cannot be achieved by setting thresholds to either source extent or hardness ratio alone. However, as these two source properties are essentially uncorrelated, a combination of both should greatly improve our odds.
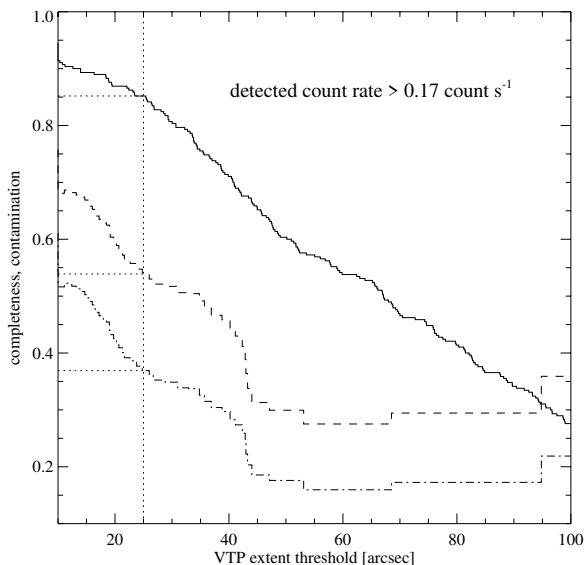

Figure A4. Completeness (solid line) and contamination by point sources (dashed line) of a strictly X-ray-selected cluster sample as a function of the chosen VTP extent threshold after the HR cut indicated by the dotted line in Fig. A3 has been applied. The ratio of point sources to extended sources in the overall sample of VTP detections is assumed to be 10 to 1. The count rate cut at 0.17 count s^{-1} corresponds roughly to the flux limit of 80 per cent completeness at 3.1×10^{-12} erg cm^{-2} s^{-1}. The dot-dashed line represents the contamination level achievable with an improved VTP algorithm that suppresses the inclusion of 'positive noise'. The dotted lines mark the completeness and contamination levels of an HR-filtered sample when the extent threshold is set to 25 arcsec.

Fig. A4 shows completeness and contamination of an X-ray-selected cluster sample as a function of the chosen extent threshold if an HR cut as shown in Fig. A3 is applied. We assume again that the ratio of point sources to intrinsically extended sources (galaxies as well as groups and clusters of galaxies) in the RASS is 10 to 1. According to Fig. A4, more than 85 per cent completeness is achievable if a VTP extent threshold of about 25 arcsec is chosen to discriminate between extended and point-like emission. The contamination of such a cluster sample selected exclusively by X-ray source characteristics (extent and hardness ratio) is typically 55 per cent. For an improved VTP algorithm with a fraction of erroneous extent determinations for point sources half as high as at present (see Section A1), the contamination is expected to fall to about 35 per cent (dot-dashed line in Fig. A4). Again, the completeness will be slightly lower (higher) and the contamination higher (lower) when a lower (higher) count rate or flux limit is aimed for.

X-ray-selected RASS cluster samples of impressive size could be obtained if such a selection were performed over the whole extragalactic sky: for flux limits of 2×10^{-12}, 3.1×10^{-12} and 4.4×10^{-12} erg cm^{-2} s^{-1} we predict sample sizes of 1300, 740 and 470 clusters, respectively (100 per cent completeness).

A4   SASS versus VTP: a performance comparison

As stated in Section A1, the SASS is a priori less prone to misclassifications of point sources as extended than VTP, while the SASS hardness ratio is as reliable a discriminator as the one derived by VTP. As a consequence, one might expect that cluster selection by X-ray properties should be even more efficient when the source parameters returned by the SASS are used. This, however, is true only as far as the contamination is concerned. With the fraction of point sources misclassified as extended by the SASS being about half as big as that found for VTP (see Fig. A1), the contamination of an SASS X-ray-selected cluster sample can be expected to lie somewhere in the range of values delineated by the dot-dashed line in Fig. A4.

Unfortunately, the SASS not only detects fewer point sources as extended, but is also much less efficient in detecting the extent of truly extended sources, in particular when the emission is of low surface brightness, thus providing little contrast with the background. This flaw goes hand in hand with the fact that the SASS heavily underestimates the flux from extended emission (cf. fig. 22 of EVB). Fig. A5 compares the extent values returned by the SASS and VTP for those BCS clusters that have been detected by both algorithms. (For obvious reasons we limit this comparison to detections of Abell and Zwicky clusters, and do not include sources initially selected because of their SASS extent.) Note that this comparison is favourable to the SASS, as it does not reflect a significant number of sources in the respective flux ranges that the SASS has missed altogether (see Section 7.1). We find that, at the lowest possible RASS flux limit of completeness, both algorithms are about 75 per cent efficient in recognizing clusters as extended X-ray sources when a threshold of 35 arcsec is chosen for the extent parameter. As mentioned earlier in Section 3.1, this is the best possible extent threshold for the SASS, as the fraction of SASS-extended BCS clusters does not increase significantly when a lower value is chosen (see also Fig. 6). As, for this largest of the three flux-limited samples of common detections depicted in Fig. A5, VTP is equally efficient at the same numerical extent value, we will use 35 arcsec as the common threshold for the extent parameters returned by either algorithm in the comparison at the end of this section.
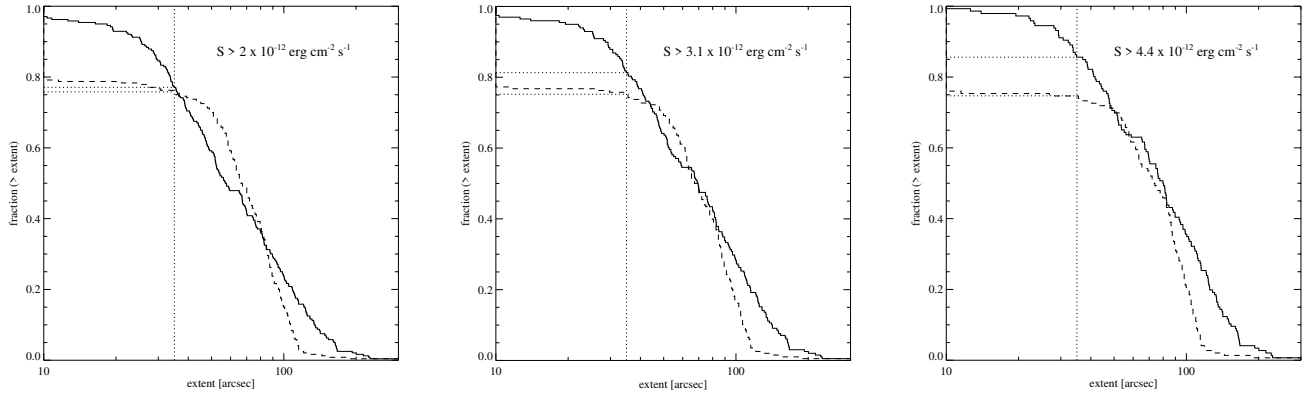
Figure A5. The cumulative extent distributions of the BCS clusters detected by both the SASS and VTP for various flux limits. The dotted lines mark the fraction of clusters and non-cluster sources classified as extended by each algorithm when the extent threshold is set to 35 arcsec. In each panel, the solid line shows the extent distribution returned by VTP, while the dashed curve represents the distribution of SASS extents. The chosen flux cuts correspond to the lowest possible RASS flux limit of completeness and the BCS flux limits of 80 and 90 per cent completeness.
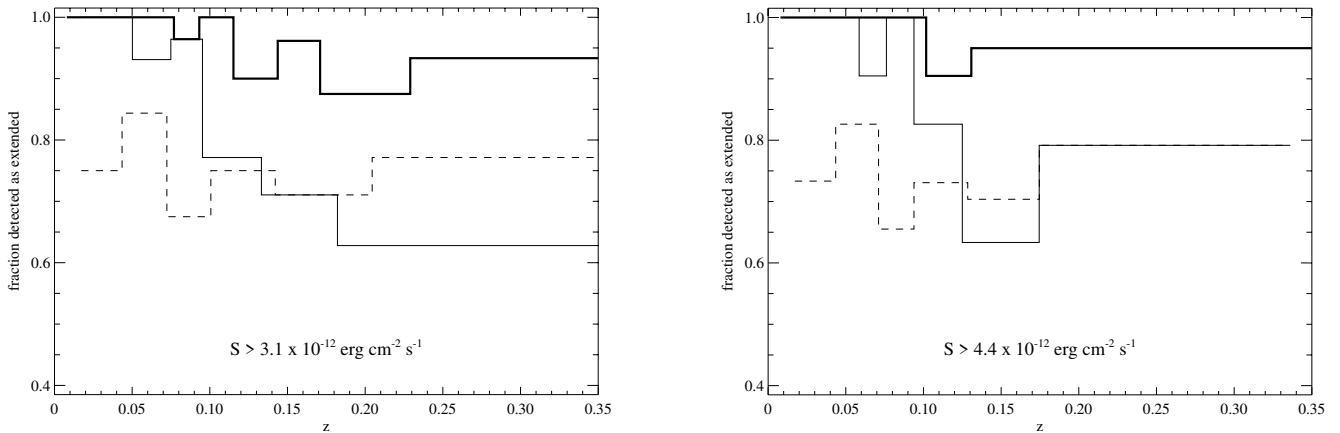

Figure A6. The fraction of common (SASS- and VTP-detected) Abell and Zwicky clusters in the BCS that feature an X-ray source extent of more than 35 arcsec, at the flux limits of the 80 and 90 per cent complete BCS subsamples (left- and right-hand panels, respectively). In each panel, the thin solid line refers to VTP while the dashed one shows the SASS performance. The thick solid lines represent the fraction of *all* BCS clusters at the respective flux limit that have been classified as extended by either or both of the two algorithms i. e. – in addition to Abell and Zwicky clusters – it also takes into account the systems originally selected on the grounds of their SASS extent. In the left-hand plot, each redshift interval but the first in the various histograms contains 29 clusters, while in the right-hand plot the respective number is 18.

Note, however, that a lower threshold leads to a significantly increased fraction of VTP-extended clusters, while the SASS efficiency remains essentially constant. Also, the maximal completeness achievable with an SASS-extent-selected sample does not increase any further i. e. beyond 75 per cent, when the flux limit of the sample is raised, which is mainly due to the poor correlation between the SASS-detected fluxes and the true cluster fluxes (EVB). As far as VTP goes, the flux limit does, however, have an effect on the fraction of clusters recognized as extended: of the 198 (145) BCS clusters at fluxes greater than 3.1×10^{-12} erg s^{-2} cm^{-2} (4.4×10^{-12} erg s^{-2} cm^{-2}) detected by both the SASS and VTP (again excluding the ones selected only because of their SASS extent), VTP finds 81 (86) per cent to be significantly extended in the X-ray.

As mentioned before, the resulting 25 per cent incompleteness of a cluster sample selected exclusively by SASS extent at essentially all flux levels is only the component arising from unrecognized extended sources. An *additional* incompleteness of more than 20 per cent (at fluxes of 3.1×10^{-12} erg s^{-2} cm^{-2}) is caused by the fact that one out of five clusters is missed altogether at the SASS count

rate cut of 0.1 count s^{-1} from which our study started. This number can certainly be reduced by including fainter SASS detections to begin with – however, all these additional sources need to be reprocessed by an algorithm that allows the true fluxes to be determined. With the ratio between true and SASS-detected count rates exceeding 2.3 (3.0) for more than 25 (11) per cent of the SASS detections of clusters with true fluxes higher than 3.1×10^{-12} erg s^{-2} cm^{-2}, this implies that all SASS detections at least down to count rates of 0.046 count s^{-1} would need to be re-evaluated. This, however, is the SASS detection limit in the RASS i. e. even if *all* extended SASS sources were reprocessed by VTP or some other algorithm, this would not even ensure *detection* completeness at 3.1×10^{-12} erg s^{-2} cm^{-2}. Also, the 25 per cent incompleteness owing to unrecognized extent would of course remain.

Given these difficulties, it is not obvious how a statistically complete and entirely X-ray-selected cluster sample can ever be compiled from SASS data at fluxes below the BCS flux limit of 90 per cent completeness, without essentially reprocessing the entire RASS raw data with an additional algorithm that allows the erroneous flux and extent determinations of the SASS to be corrected.

If, however, priority is given to low contamination rather than completeness, an SASS-selected cluster sample might be slightly preferred over one based on VTP detections. The resulting sample will be at best 70 per cent complete, but the contamination by point sources will be no higher than about 40 per cent, compared with some 55 per cent for a VTP-based sample. The latter will, however, be 85 to 90 per cent complete.

Turning again to the flux-limited BCS subsamples, we confirm the results of EVB on the redshift dependence of the cluster fraction detected as extended by the SASS or VTP. Fig. A6 shows the fraction of extended sources in the sample of BCS clusters detected by both algorithms as a function of redshift (again, clusters originally included solely on the grounds of their SASS extent have been excluded). As EVB did for their ACO cluster sample, we find the SASS to perform at the about 75 per cent level, independently of redshift and flux limit. The fraction of VTP-extended BCS clusters is similar (about 70 per cent for either flux limit) at redshifts greater than 0.1, but rises steeply to more than 95 per cent for more nearby clusters.

When all 283 (203) clusters of the 80 (90) per cent complete, flux-limited BCS are considered, the total fraction of clusters classified as extended by either or both of the two algorithms reaches an impressive 96 (97) per cent, which varies only little with redshift (bold solid lines in Fig. A6).

A5   Summary

To summarize, we confirm that cluster selection by X-ray source extent and hardness ratio works. However, owing to the (different) imperfections of each of the two detection algorithms used in the present study (SASS and VTP), the compilation of *statistically useful* cluster samples requires a massive amount of work. With VTP, the price to be paid for a highly flux-complete sample (85 to 90 per cent) is a considerable point source contamination of some 55 per cent (35 per cent if an improved version of VTP is used). These point sources need to be removed from the sample by visual inspection of the X-ray detections and potential optical counterparts. With the SASS, the contamination by point sources is slightly lower (typically 40 per cent), but the highest achievable completeness is no more than about 70 per cent. Owing to the biases introduced by such a low completeness, the statistical usefulness of such a purely SASS-based cluster sample must remain doubtful.

This paper has been typeset from a T$_E$X/L^{A}T$_E$X file prepared by the author.